Linear Dichroism in the NEXAFS spectroscopy of *n*-alkane thin films

A Thesis Submitted to the College of
Graduate Studies and Research
In Partial Fulfillment of the Requirements
For the Degree of Doctor of Philosophy
In the Department of Chemistry
University of Saskatchewan
Saskatoon

By

Juxia Fu

Permission to Use

In presenting this thesis in partial fulfillment of the requirements for a postgraduate degree from the University of Saskatchewan, I agree that the Libraries of this University may make it freely available for inspection. I further agree that permission for copying of this thesis in any manner, in whole or in part, for scholarly purposes may be granted by Professor S. G. Urquhart who supervised my thesis work or, in his absence, by the Head of the Department of Chemistry or the Dean of the College of Graduate Studies and Research. It is understood that any copying or publication or use of this thesis or parts thereof for financial gain shall not be allowed without my written permission. It is also understood that due recognition shall be given to me and to the University of Saskatchewan in any scholarly use that may be made of any material in my thesis.

Request for permission to copy or to make other use of material in this thesis in whole or in part should be addressed to:

The Head
Department of Chemistry
University Of Saskatchewan
Saskatoon, Saskatchewan
Canada S7N 5C9

Abstract

Linear dichroism in Near Edge X-ray Absorption Fine Structure (NEXAFS) spectroscopy has been used to determine molecular orientation at surfaces and in microscopic domains. However, the molecular orientation of *n*-alkanes cannot be derived unambiguously from their NEXAFS spectra due to the inadequate understanding of the character of the relevant spectroscopic features in the NEXAFS spectra of *n*-alkanes (i.e. C 1s $\rightarrow \sigma^*_{C\text{-}H}$, C 1s $\rightarrow \sigma^*_{C\text{-}C}$ transitions).

We have studied linear dichroism in the NEXAFS spectra of hexacontane (HC, *n*-$C_{60}H_{122}$) thin films by using angular dependent NEXAFS spectroscopy. The HC thin films were epitaxially grown onto the cleaved NaCl (001) surfaces by physical vapor deposition. NEXAFS spectra of these HC thin films were acquired at different angles using STXM microscopy. A detailed analysis of the angular dependence of the NEXAFS spectra of the HC thin film helps us to understand the relationship between the form of linear dichroism and the molecular orientation in *n*-alkane molecules. This linear dichroism in the NEXAFS spectroscopy of *n*-alkanes is relevant for quantitative measurements of molecular orientation, such as for the microanalysis of crystalline organic materials.

Linear dichroism for the NEXAFS resonances of *n*-alkanes has also been studied by *ab initio* calculations. These calculations were carried out on an isolated *n*-alkane molecule and a cluster of *n*-alkane molecules. The calculations on an isolated *n*-alkane molecule are used to study linear dichroism for the NEXAFS resonances above the C 1s ionization potential. The cluster calculations account for the matrix effects, particularly for the NEXAFS resonances below the C 1s ionization potential. These

calculations help us to understand the character and linear dichroism in the NEXAFS spectra of *n*-alkanes.

The film morphology and molecular orientation of *n*-alkane thin films have also been investigated by the NEXAFS spectroscopy and microscopy. Thin films of hexacontane (*n*-$C_{60}H_{122}$) and hexatriacontane (*n*-$C_{36}H_{74}$) were epitaxially grown onto cleaved NaCl (001) surfaces by physical vapor deposition. It is found that the film morphology and molecular orientation of *n*-alkane thin films depend on the alkane chain length and deposition parameters, such as substrate temperature. These observations have been rationalized by consideration of the kinetics and thermodynamics of nucleation and film growth.

Acknowledgements

First of all, I would like to sincerely thank my supervisor, Professor Stephen G. Urquhart, for his consistent support, excellent guidance and faith in me in the course of this work. He gave me the opportunity to get involved in this wonderful synchrotron work. The experience I gained through the course of this work will benefit my later research career.

I would like to thank the members of my advisory committee: Professor A. Baranski, Professor R. E. Verrall, and Professor K. Mitchell for their advice during the program.

I am grateful to the members of Professor Urquhart's lab: Edwige Otero, Danielle Covelli, Stephen Christensen, Rémy Coulombe, Brian Haines, Ryan Cooney, and Tania Lim.

I wish to thank the Department of Chemistry, the University of Saskatchewan, and Saskatchewan Synchrotron Institute for financial support.

Finally I express my deepest gratitude to my husband Yingshen for his encouragement and faith in me, to my mom for her taking care of my daughter so that I can focus on writing, to my father, to my parents-in-law for their love and support, and to my sweetheart, Mellissa. She brings so much joy to me.

Table of Contents

List of Tables

List of Figures

Chapter 1

Chapter 2

Chapter 3

Appendices

List of Abbreviations

AFM	Atomic force microscopy
ALS	Advanced Light Source
BA	Benzoic Acid
BB	Building Block
EMR	Electromagnetic Radiation
EPU	Elliptically Polarized Undulator
EXAFS	Extended X-ray Absorption Fine Structure
FM	Frank – van der Merwe
GSCF3	Gaussian Self Consistent Field version 3
HC	Hexacontane
HTC	Hexatriacontane
IP	Ionization Potential
IVO	Improved Virtual Orbital
KHP	Potassium Hydrogen Phthalate
LB	Langmuir-Blodgett
LD	Linear Dichroism
MES	Molecular Environment Science
MO	Molecular Orbital
NCSU	North Carolina State University
NEXAFS	Near Edge X-ray Absorption Fine Structure
OD	Optical Density

OSA	Order Sorting Aperture
p-BBA	*Para*-bromo Benzoic Acid
PBrS	Poly (bromo-styrene)
PC	Polycarbonate
PE	Polyethylene
PLM	Polarized Light Microscopy
PMMA	Poly (methyl methacrylate)
p-PBA	*p*-Phenyl Benzoic Acid
PS	Polystyrene
PTFE	Poly (tetrafluoroethylene)
PVD	Physical Vapor Deposition
RT	Room Temperature
SAMs	Self Assembly Monolayers
SCF	Self Consistent Field
SK	Stranski – Krastanov
STXM	Scanning Transmission X-ray Microscope
SVD	Singular Value Decomposition
TA	Terephthalic Acid
TDM	Transition Dipole Moment
TTC	Tetratetracontane
TV	Term Value
VM	Volmer – Weber
X-PEEM	X-ray Photoelectron Emission Microscopy

Chapter 1 Introduction

Linear dichroism (LD) observed in Near Edge X-ray Absorption Fine Structure (NEXAFS) spectroscopy is used frequently to measure the orientation of organic materials such as surface adsorbed molecules (Stöhr 1992), ultrathin films (Zharnikov et al. 2001), crystalline polymers (Smith et al. 1996; Croll et al. 2003), and rubbed polymer surfaces (Stöhr et al. 1998). The relationship between the molecular orientation and the LD in the NEXAFS spectroscopy of unsaturated species is well established. However, the relationship between the molecular orientation and LD in the NEXAFS spectroscopy of saturated species, such as *n*-alkanes, is poorly defined. Therefore, the primary goal of this project is to provide an experimental measurement of the LD in the NEXAFS spectroscopy of *n*-alkane thin films. The detailed research objectives are described in §1.8.

The theory of NEXAFS spectroscopy and its applications to qualitative, quantitative, and orientation analysis of organic materials are presented in §1.1. The concept of LD is introduced in §1.2, including the definition of LD, symmetry considerations, and the application of LD for orientation analysis. The specific application of LD in NEXAFS spectroscopy and microscopy is given in §1.3 and §1.4, respectively. The NEXAFS spectroscopy of *n*-alkanes is introduced in §1.5. The *n*-alkane thin film preparation method employed in this project, epitaxial growth, is

introduced in §1.6. The morphology of these thin films is interpreted by various thin film growth mechanisms that are introduced in §1.7. The research objectives of this project are presented in §1.8.

1.1 Near-Edge X-ray Absorption Fine Structure (NEXAFS)

The intensity of X-rays transmitted through a sample decreases due to X-rays absorption. Depending on the energy of X-rays, the absorbed X-rays can excite core electrons from different levels in an atom or a molecule. Based on the origin of the excited electron, the absorption edge can be classified as K-edge (corresponding to the excitation of a 1s electron.), L-edge (L_I-, L_{II}-, and L_{III}-edge corresponds to the excitation of a 2s, $2p_{1/2}$, and $2p_{3/2}$ electron, respectively), and so on. Figure 1.1 presents a typical X-ray absorption cross section as a function of the X-ray energy (Teo 1986).

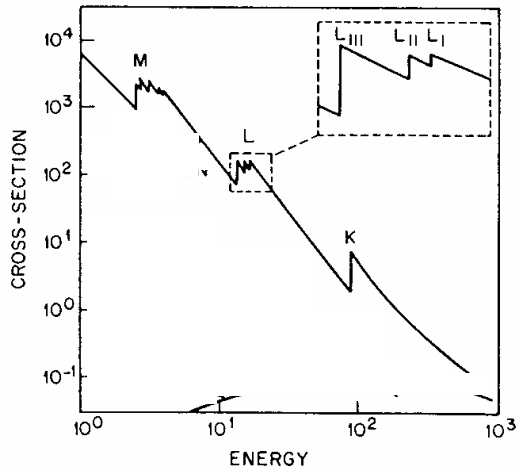

Figure 1.1 Definition of X-ray absorption edge (Teo 1986).

With the increase of photon energy, the X-ray absorption cross section that describes the probability of absorption decreases. However, when the photon energy corresponds to the binding energy of a core electron, the X-ray absorption cross section

increases abruptly, and then decreases monotonically above the core edge. Thus an edge-like structure is observed in the absorption spectrum.

X-ray absorption cross section

The X-ray absorption cross section and optical oscillator strength are the two main factors to describe the absorption probabilities. The absorption cross section is defined as the number of electrons excited per unit time divided by the number of incident photons per unit time per unit area (Stöhr 1992). Within the dipole approximation the X-ray absorption cross section is given by (Stöhr 1992)

$$\sigma_x = \frac{4\pi^2\hbar^2}{m^2}\frac{e^2}{\hbar c}\frac{1}{\hbar\omega}\left\langle \psi_f \left| \mathrm{E} \bullet \mu \right| \psi_i \right\rangle^2 \rho_f(E) \tag{1.1}$$

where σ_x is the X-ray absorption cross section in cm^2, which is usually expressed in barn ($1\ cm^2 = 10^{24}$ barn), $\hbar = h/2\pi$, h is the Planck constant, c is the speed of light, e is the electron charge, m is the mass of the electron, $\hbar\omega$ is the photon energy, $\boldsymbol{E}$ is the electric field vector of X-ray photons, μ is the dipole operator, ψ_f is the wavefunction of the final state, ψ_i is the wavefunction of the initial state, and $\rho_f\ (E)$ is the energy density of the final state.

Eq. (1.1) is the basis of theoretical calculations of X-ray absorption spectra. The outcome of these theoretical calculations is often expressed as the *optical oscillator strength f*, which is related to the X-ray absorption cross section by (Stöhr 1992)

$$\sigma_x(E) = C\frac{df}{dE} \tag{1.2}$$

where $C = 2\pi^2 e^2\hbar/mc = 1.1 \times 10^2$ Mb eV (1 Mb = 1 megabarn). f is the energy integral of the X-ray absorption cross section, and therefore, a measure of the intensity of a

resonance. The *optical oscillator strength* is often quoted as an "*f number*" (Stöhr 1992)

$$f = \frac{2}{m\hbar\omega}\left\langle \psi_f \left| \mathrm{E} \bullet \mu \right| \psi_i \right\rangle^2 \tag{1.3}$$

The calculated oscillator strengths *f* for transitions can be converted to X-ray absorption cross section by use of Eq. (1.4) (Stöhr 1992)

$$\sigma_x(E) = \frac{2\pi^2 e^2 \hbar}{mc} f\rho_f(E) \tag{1.4}$$

X-ray absorption spectrum

Generally, the X-ray absorption spectrum can be divided into two parts, the Near Edge X-ray Absorption Fine Structure (NEXAFS) that corresponds to the absorption up to ~50 eV above the absorption edge and Extended X-ray Absorption Fine Structure (EXAFS), which corresponds to the absorption up to 1000 eV above the absorption edge. EXAFS spectroscopy is used mostly in the study of inorganic species for determining the numbers, types, and distances of the backscattering atoms surrounding the absorbing atoms (Lee et al. 1981). For example, the Mn K-edge EXAFS spectra are used to investigate the oxygen evolving complex (Mukhopadhyay et al. 2004). However, core edges in low Z atoms are too close together to permit EXAFS analysis. For organic molecular species, the NEXAFS part of the spectrum is the most useful.

Principles of NEXAFS spectroscopy

Figure 1.2 outlines the principles of NEXAFS spectroscopy. Near the K-shell absorption threshold, a series of fine structures are superimposed on the absorption edge. In organic molecules, these fine structures are dominated by resonances arising from transitions of 1s core electrons to unoccupied π^* or σ^* orbitals, depending on the

covalent bonding in the molecule, as well as to Rydberg orbitals (left side of this Figure). The characteristic features of the K-shell spectrum are shown in the right part of this figure. The NEXAFS spectrum is usually dominated by two types of resonances, with the ionization potential (IP) as a boundary. Resonances below the IP correspond to the excitation of a core electron to a bound orbital. These orbitals are usually of π^* or Rydberg character and sometimes of σ^* character for saturated species, such as *n*-alkanes. These resonances are usually sharp and well-defined. Resonances above the IP usually correspond to the excitation of a core electron to an unbound orbital of σ^* character, as well as double excitation. These resonances are usually broad. At the IP, a step-like increase is observed, from the onset of the core edge (cf. Figure 1.1).

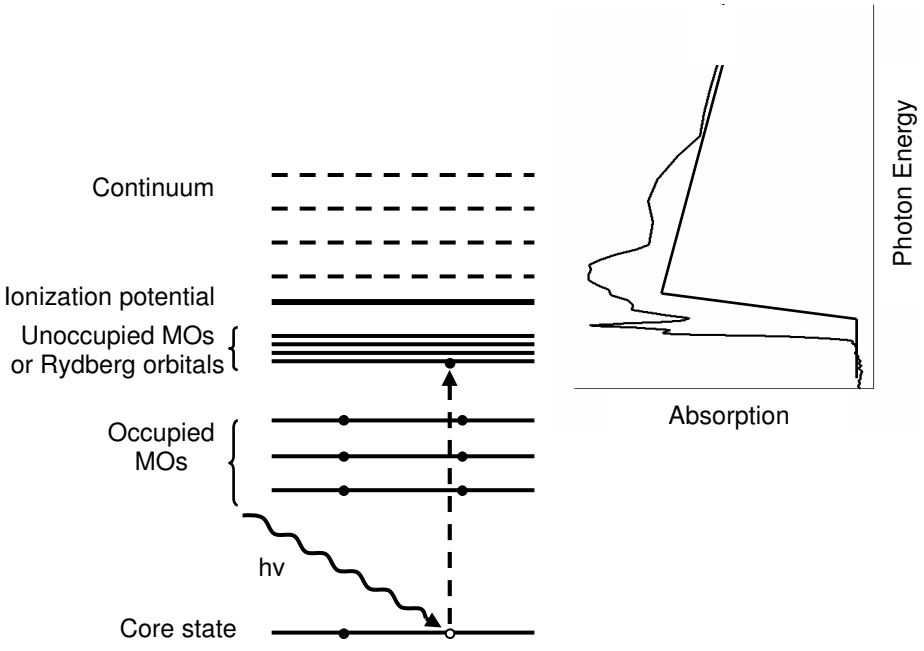

Figure 1.2 Schematic illustration of a NEXAFS spectrum

NEXAFS spectroscopy can be used for qualitative analysis of organic materials to obtain information like which element and what functional groups are present in the sample. This spectroscopy can also be used to quantitatively determine the chemical composition of a complex polymer. Furthermore, polarization dependent NEXAFS spectroscopy allows orientation analysis. These capabilities of NEXAFS spectroscopy will be described below.

1.1.1 Qualitative analysis of NEXAFS spectroscopy

The chemical sensitivity of NEXAFS spectroscopy arises from several factors. Each element has a characteristic electron binding energy. For example, the binding energy of Carbon 1s is ~285 eV, Nitrogen 1s ~410 eV, Oxygen 1s ~543 eV, and Fluorine 1s ~ 696 eV (Stöhr 1992; Thompson et al. 2001), therefore, NEXAFS has elemental sensitivity. Secondly, NEXAFS spectroscopy is sensitive to the bonding within different functional groups (Ade et al. 1992; Ade 1997; Smith et al. 2001; Dhez et al. 2002). For example, the C 1s $\rightarrow \pi^*_{C\equiv N}$ transition of the acrylonitrile group occurs at 287 eV in poly(styrene-*r*-acrylonitrile) and the C 1s $\rightarrow \pi^*_{C=C}$ transition of the phenyl ring occurs at 285 eV. For the phenyl ring, the symbol "$\pi^*_{C=C}$" is used to denote the delocalized π^* structure in the phenyl ring for typographical convenience. The origin of the energy shift of core $\rightarrow \pi^*$ transitions in different functional groups is due to differences in the unoccupied orbital energy as well as that of the C 1s core level. This effect is illustrated in Figure 1.3 (Ade et al. 2002). The y-axis of this figure shows the energy relative to the vacuum level for the carbon 1s orbitals (e.g the ionization potential), as well as the energy of the unoccupied molecular orbitals of the C≡N group

and the C=C group in the phenyl ring (usually identified as the term value). The carbon 1s ionization potential for C≡N is greater than that for a C=C bond in the phenyl ring, due to the electronegativity of the nitrogen atom in the acrylonitrile group. The term value of the $\pi^*_{C\equiv N}$ molecular orbital is larger than that of $\pi^*_{C=C}$ in the phenyl ring. Considering both the 1s ionization potential and the unoccupied orbital term value, the transition energy of C $1s_{(Ph)} \rightarrow \pi^*_{C=C(Ph)}$ transition is less than that of the C $1s_{(C\equiv N)} \rightarrow \pi^*_{C\equiv N}$ transition. Therefore, the first transition at 285 eV is the electronic transition of C $1s_{(Ph)} \rightarrow \pi^*_{C=C(Ph)}$ in the phenyl functional group and the second transition at 287 eV corresponds to the C $1s_{(C\equiv N)} \rightarrow \pi^*_{C\equiv N}$ transition of the acrylonitrile functional group.

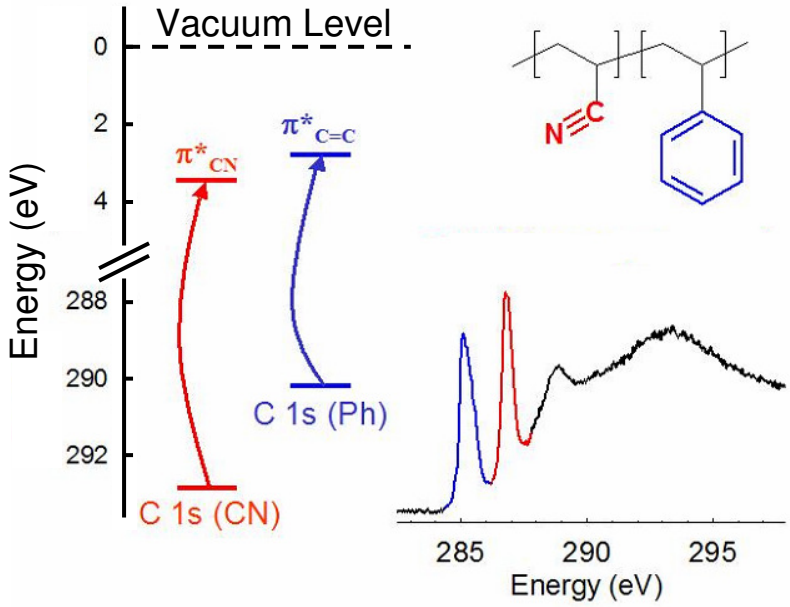

Figure 1.3 Electronic schematic for the NEXAFS photoabsorption spectrum of poly(styrene-r-acrylonitrile) (Ade et al. 2002)

This functional group sensitivity of NEXAFS spectroscopy has been studied widely. Figure 1.4, for example, shows NEXAFS spectra of a series of carbon

containing organic compounds: polyethylene (PE), poly(methyl methacrylate) (PMMA), polystyrene (PS), poly(bromo-styrene) (PBrS), and polycarbonate (PC) (Smith et al. 2001).

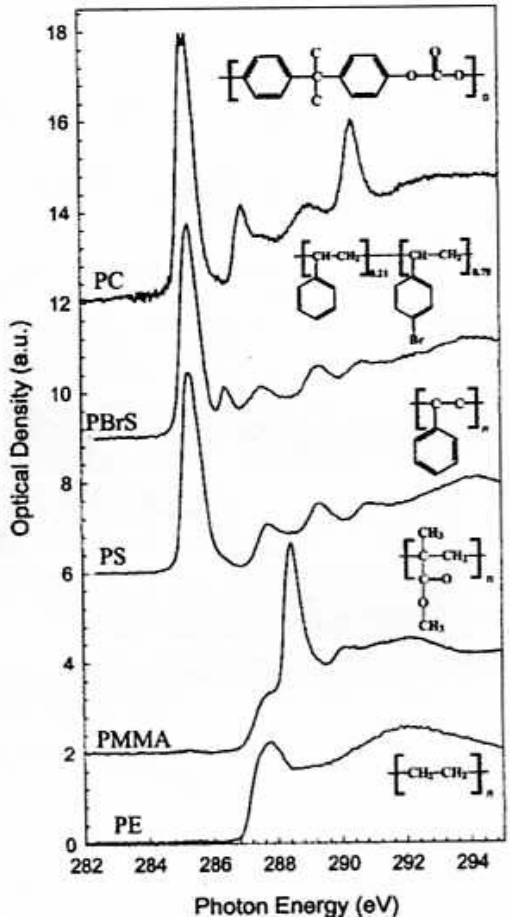

Figure 1.4 C 1s NEXAFS spectra of organic compounds (Smith et al. 2001)

Saturated PE has a relatively simple X-ray absorption spectrum, with two broad resonances at 287.8 eV and 292 eV, corresponding to C 1s $\rightarrow \sigma^*$ transitions. The NEXAFS spectra of unsaturated compounds exhibit a complex structure. In PMMA, the sharp and intense peak at 288.4 eV corresponds to C $1s_{(C=O)} \rightarrow \pi^*_{(C=O)}$ transition, while in PC, this transition shifts to higher energy (290.4 eV) due to the inductive

effect of the two oxygen atoms adjacent to the carbonyl group. In PC, PBrS, and PS, the C=C group in the phenyl ring has a similar chemical environment, and therefore, the intense peak at 285.0 eV, corresponding to C 1s $\rightarrow \pi^*_{C=C}$ in the phenyl ring, is observed in these three compounds. However, comparison of the spectra of PBrS and PS reveals that the substitution of Br in the *para* position on the phenyl ring shifts the C 1s binding energy of this substituted carbon atom to higher energy. Therefore a small sharp peak at 286.4 eV is observed, just above the most intense C 1s $\rightarrow \pi^*_{C=C}$ in the NEXAFS spectrum of PBrS.

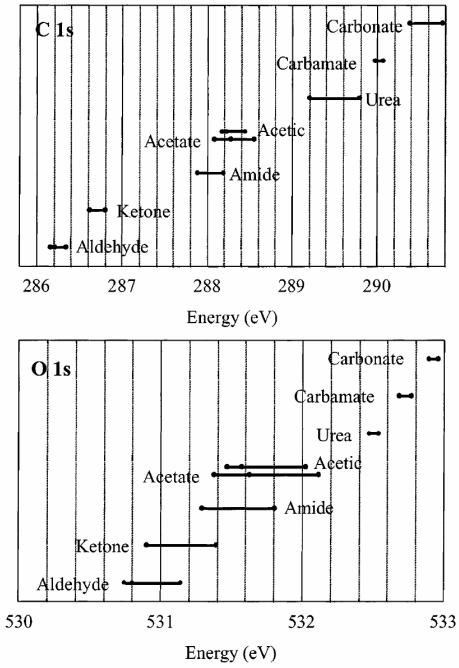

Figure 1.5 Spectroscopic correlation diagram for the expected energies of the C 1s $\rightarrow \pi^*_{C=O}$ transitions (top) and the O 1s $\rightarrow \pi^*_{C=O}$ transitions (bottom) in molecules containing the carbonyl group (Urquhart et al. 2002)

The chemical sensitivity of NEXAFS spectroscopy is useful not only in identifying functional groups, but also in establishing spectroscopic correlation diagrams for the same group in different chemical environments. Urquhart and Ade

(Urquhart et al. 2002) explored the chemical sensitivity of carbonyl core (C 1s, O 1s) $\rightarrow \pi^*_{C=O}$ transitions in C 1s and O 1s NEXAFS spectra for a series of carbonyl containing compounds in different bonding environments. A spectroscopic correlation diagram for the expected energies of the C 1s $\rightarrow \pi^*_{C=O}$ transitions and O 1s $\rightarrow \pi^*_{C=O}$ transitions in molecules containing the carbonyl group is shown in Figure 1.5

NEXAFS spectroscopy is also sensitive to electronic delocalization. For example, in the ring substitution isomers of 1,2- dimethyl phthalate, 1,3- dimethyl phthalate, and 1,4- dimethyl phthalate (Urquhart et al. 1997), the energy of C 1s $\rightarrow \pi^*_{C=C}$ and C 1s $\rightarrow \pi^*_{C=O}$ transitions shifts due to the changing nature of $\pi^*_{C=C}$ and $\pi^*_{C=O}$ mixing in the isomers.

The above examples qualitatively illustrate that NEXAFS spectroscopy can be employed to obtain information about organic materials, such as element species, functional group, substitution effect, electronic dislocalization, etc. In addition, NEXAFS spectroscopy can also be used for quantitative analysis of organic materials.

1.1.2 Quantitative analysis of NEXAFS spectroscopy

The basis for quantitative analysis of NEXAFS spectroscopy in transmission measurements is the optical Beer-Lambert law; the photon transmission is converted to optical density (OD) according to

$$OD = -\ln(\frac{I}{I_0}) \tag{1.5}$$

where for a given X-ray energy, I_0 is the incident flux of the X-ray beam, I is the transmitted flux through the sample, and ln is the natural logarithm. The OD is related to the sample's properties by:

$$OD = \mu \cdot \rho \cdot t = \mu_l \cdot t \tag{1.6}$$

where μ (cm^2/g) is the mass absorption coefficient, ρ (g/cm^3) is the density of the material, t (cm) is the sample thickness, and μ_l (cm^{-1}) = $\mu\rho$ is the linear absorption coefficient. The mass absorption coefficient μ is a function of the atomic absorption cross section σ_a (cm^2) and atomic mass A (g/mol) according to (Thompson et al. 2001)

$$\mu = \frac{N_A}{A}\sigma_a \tag{1.7}$$

where N_A is the Avogadro number.

Thus the experimentally measured *OD* and the theoretically calculated *oscillator strength*, *f*, have the following relationship by combination of Eq.(1.4), (1.6), and (1.7)

$$OD = \frac{N_A}{A}\frac{2\pi^2 e^2 \hbar}{mc}\rho t \rho_f(E) f \tag{1.8}$$

i.e., the experimental OD is proportional to the calculated *f*. They both represent the strength of a transition.

The chemical composition of polyurethane samples have been investigated by NEXAFS spectroscopy (Urquhart et al. 1999). The results indicate that with the appropriate model compounds, C 1s NEXAFS spectroscopy can determine the chemical composition of a complex polymer such as polyurethane at the 10% molar level. This is relevant for chemical microanalysis by X-ray microscopy. In addition, quantitative maps of polystyrene (PS) and poly(methyl methacrylate) (PMMA) blend polymers have also been obtained by NEXAFS microscopy (Urquhart et al. 1999).

1.1.3 Orientation analysis of NEXAFS spectroscopy

While the transition energy and intensity for a NEXAFS feature depends on the presence of elements and their bonding in specific functional groups, the intensity of a specific transition also depends on the orientation of the transition dipole moment associated with that transition relative to the polarization vector of the linearly polarized X-ray beam. Therefore, NEXAFS spectroscopy is sensitive to molecular orientation. This linear dichroism will be introduced in §1.2. The orientation analysis of NEXAFS spectroscopy will be presented in §1.3.

1.2 Linear Dichroism (LD)

Linearly polarized electromagnetic radiation (EMR)

Linear dichroism (LD) (Norden 1978; Rodger et al. 1997; Schellman et al. 1997) is the anisotropic absorption of plane or linearly polarized electromagnetic radiation (EMR). EMR has electric and magnetic fields. These two fields are orthogonal to each other and perpendicular to the direction of propagation, as illustrated in the left side of Figure 1.6. When considering the polarization of EMR, the electric field vector (***E*** vector) is described and the magnetic field ***B*** is usually ignored as the ***B*** vector is fully defined relative to the ***E*** vector and the propagation direction. The oscillating electric field ***E*** *(x, t)* of EMR along the *x*-direction is written as

$$E(x,t) = E_0 \cos\{2\pi\nu t - (\frac{2\pi}{\lambda})x + \phi\} \tag{1.9}$$

where E_0 is the amplitude of the electric field, λ is the wavelength, ν is the frequency, and ϕ is the phase of the light wave. In linearly polarized EMR, the electric field oscillates in a single plane as illustrated in Figure 1.6 (right).

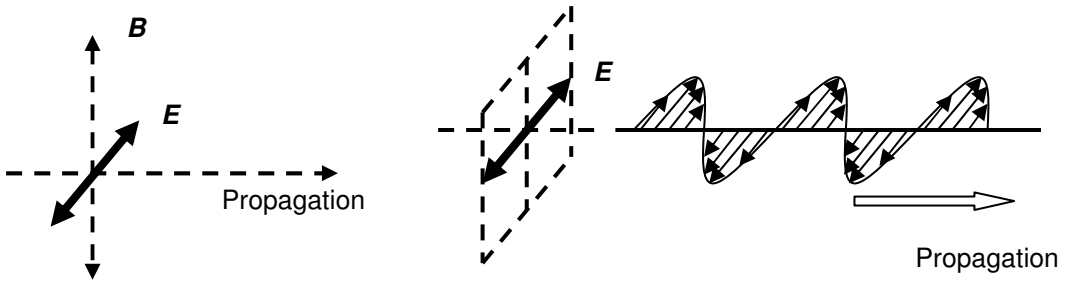

Figure 1.6 (left) ***E*** vector, ***B*** vector, and propagation direction of electromagnetic radiation (EMR) wave are orthogonal to each other. (right) Linearly polarized EMR.

Transition dipole moment (TDM)

When a molecule absorbs a photon of EMR with the appropriate energy, $h\nu$, to excite it from its ground or initial state, ψ_i, to its excited or final state, ψ_f, the electric field of the EMR relocates the electrons to a new stationary state, where the electron distribution in the molecule is reorganized for minimal total energy. The effect of the electric field is to cause a linear rearrangement of charge. The net linear displacement of charge during any transition is called the electric transition dipole moment (TDM)

$$\mu_{if} = \langle \psi_i | \mu | \psi_f \rangle \tag{1.10}$$

where μ is the electric dipole moment operator, which defines the polarization of the transition according to

$$\mu = \mu_x + \mu_y + \mu_z = \sum_i e_i x_i + \sum_i e_i y_i + \sum_i e_i z_i \tag{1.11}$$

where μ_x, μ_y and μ_z are electric dipole moment operators along the x, y, and z directions, respectively, e_i represents the charge on the i^{th} particle, and x_i, y_i, z_i are its Cartesian coordinates.

Dipole selection rule

The excitation of K-shell electrons is often discussed within the dipole approximation (e.g. Eq. 1.1) (Stöhr 1992). Therefore, the transition between the initial state ψ_i and final state ψ_f is governed by the dipole selection rule. A transition dipole moment μ_{if} must be zero if the integrand along all of the three components is not totally symmetric under the symmetry operations of this system. An electric dipole transition is allowed along x, y, or z polarization planes if the direct product of the representations of the two states concerned $\Gamma_f \otimes \Gamma_i$ is or contains the irreducible representation to which x, y, or z, respectively, belongs (Somers et al. 1989; Cotton 1990).

Intensity of a transition

The intensity of an electric dipole allowed transition is the dot product of the ***E*** vector of light and the TDM of that transition, as given by (Charney 1988; Stöhr 1992; Rodger 1993)

$$I \propto \left| E \bullet \mu_{if} \right|^2 = \left| E \right|^2 \left| \mu_{if} \right|^2 \cos^2 \theta \qquad (1.12)$$

where ***E*** is the polarization of the electric field vector of the light and θ is the angle subtended between ***E*** and μ_{if}. Clearly, the strength of a transition depends on the orientation of the TDM (μ_{if}) associated with that transition relative to the direction of ***E***, which is illustrated in Figure 1.7. The ***E*** vector of the light, in this diagram, is in the plane of the paper. In this example, the molecule has two electric dipole allowed transitions with TDM μ_{if1} (in the plane of the paper) parallel to the ***E*** and TDM μ_{if2} (out of the plane of the paper) perpendicular to the ***E***, respectively. In the hypothetical

absorption spectrum, light polarized parallel to the TDM (μ_{if1}) has maximum probability of absorption (A_1, dashed line) and, on the contrary, if the polarization of the light is perpendicular to the TDM (μ_{if2}) no absorption (A_2, solid line) takes place for that transition (Rodger 1993).

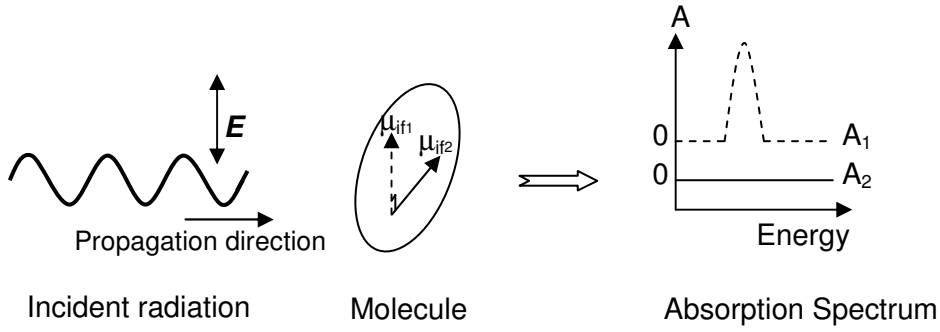

Figure 1.7 Linear dichroism of absorption (Rodger 1993).

Thus, the linear dichroism can be analyzed to derive the orientation of the TDM for a transition with respect to the polarization of incident light provided that the ***E*** vector of the incident light is known. If the TDM for a transition is known, then the orientation of an oriented molecule can be determined from this linear dichroism.

Linear dichroism studies are widely used to measure the orientation of biomaterials, such as DNA, proteins, polypeptides (Charney 1988), and self-assembled monolayer (SAMs), Langmuir-Blodgett (LB) films, rubbed polymers (Samant et al. 1996), etc. Linear dichroism studies can be carried out by a variety of spectroscopic techniques such as attenuated total reflectance (Pelletier et al. 2003), infrared reflection absorption spectroscopy (Pelletier et al. 2002; Pelletier et al. 2003), and polarization modulation infrared reflection absorption spectroscopy (Pelletier et al. 2002). Raman

spectroscopy can also be used to derive molecular orientation (Ianoul et al. 1999; Rousseau et al. 2004).

NEXAFS spectroscopy has been used to study the linear dichroism of organic materials, such as *n*-alkanes. Figure 1.8 is an example showing the linear dichroism in the NEXAFS spectroscopy of a well ordered *n*-alkane thin film from our work. The solid line represents the spectrum when the ***E*** vector is perpendicular to the macromolecular axis, which exhibits maximum intensity in the resonances at ~288 eV. The dashed line represents the spectrum when the ***E*** vector is parallel to the macromolecular axis, which shows the maximum intensity at ~293 eV. The difference observed in these two spectra is ascribed to the different geometrical arrangements of the macromolecular axis relative to the ***E*** vector. A detailed analysis of these spectra is given in §3.2.2 and §3.3.

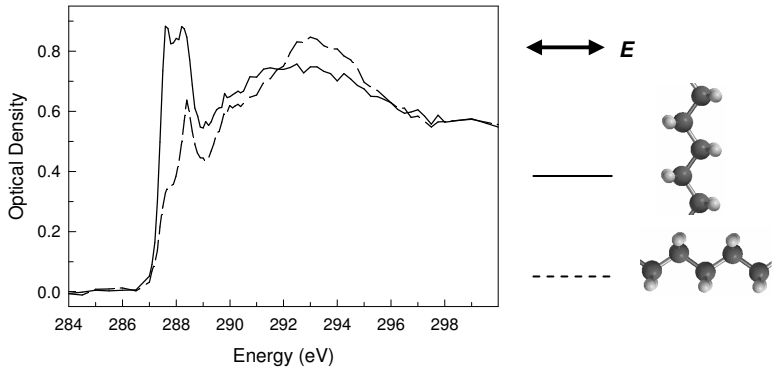

Figure 1.8 LD in the C 1s NEXAFS spectroscopy of ordered hexacontane thin film

1.3 LD in NEXAFS spectroscopy

In NEXAFS spectroscopy of organic materials, features can be described as one electron transitions between the core level and an unoccupied orbital. The intensity of

these transitions depends on the subtended angle between the $\boldsymbol{E}$ vector of the X-rays, and the direction of the TDM according to Eq. (1.12) (Stöhr 1992).

In a molecule, core excitation transitions are generally considered to follow an "atomic propensity rule" in which excitations are considered to obey atomic selection rules ($\Delta l = \pm 1$) on the core excited atom. Based on the "atomic propensity rule", the electric-dipole matrix element for 1s core excitation is dominated by terms involving 1s atomic orbitals of the initial level and the 2p atomic orbitals localized at the site of the localized core excitation (Urquhart 1997). Therefore, for excitation from a 1s orbital, the TDM points in the same direction as the *p*-component in the optical orbital on the excited atoms. Thus, Eq. (1.12) can be simplified as

$$I = A\cos^2\theta \tag{1.13}$$

where A describes the angle-integrated cross section and θ is the angle between the $\boldsymbol{E}$ vector of X-rays and the direction of the *p*-component in the final state orbital.

LD in unsaturated systems

LD of NEXAFS spectroscopy for unsaturated materials is simple and straightforward because the core $\rightarrow \pi^*$ transitions are sharp and lie at energies well below the ionization potential. Thus their position and intensity can be determined quite accurately.

A number of LD studies using core $\rightarrow \pi^*$ transitions in NEXAFS spectroscopy have been carried out on simple systems, such as CO vertically adsorbed on a Mo (110) surface (Stöhr 1992), and on complicated systems such as aromatic polymer thin films (Samant et al. 1996; Cossy-Favre et al. 1998; Stöhr et al. 1998; Weiss et al. 1998; Giebler et al. 1999; Stöhr et al. 1999; Weiss et al. 2000; Crain et al. 2001; Ernst et al.

2001; Stöhr et al. 2001; Croll et al. 2003). For example, the surface orientation of buffed polyimides was investigated through the angular dependence of C 1s $\rightarrow \pi^*_{C=C}$ transitions for the phenyl ring (Samant et al. 1996). The polyimide chains at the film surface were found to be highly aligned in the buffing direction. In addition, the NEXAFS study of liquid crystal alignment on these rubbed polyimide films reveals a preferred in-plane and out-of-plane orientation of phenyl and C=O groups at the surface (Stöhr et al. 1998). Furthermore, the surface orientation of stylized and rubbed polyimides was investigated by X-ray photoelectron emission microscopy (X-PEEM) through monitoring the intensity of C 1s $\rightarrow \pi^*$ transition with respect to the $\boldsymbol{E}$ vector. The X-PEEM results on rubbed polyimides showed lateral inhomogeneities in the rubbing process, suggesting that the oriented regions act as nucleation sites or pinning sites for liquid crystals (Cossy-Favre et al. 1998).

Figure 1.9 illustrates a simple example of the orientation of the CO molecule on a Mo (110) surface (Stöhr 1992). CO is normally oriented on the Mo (110) surface. The C 1s $\rightarrow \pi^*_{CO}$ and C 1s $\rightarrow \sigma^*_{CO}$ transitions are both electric dipole allowed. The TDM of C 1s $\rightarrow \pi^*_{CO}$ transition is parallel to the substrate surface, while the TDM of C 1s $\rightarrow \sigma^*_{CO}$ transition is perpendicular to the substrate surface. When X-rays are incident normal to the substrate surface, the $\boldsymbol{E}$ vector is parallel to the TDM of the C 1s $\rightarrow \pi^*_{CO}$ transition and maximum intensity is observed at this transition. In the case, when the X-rays are incident grazing (20°) to the substrate surface, the $\boldsymbol{E}$ vector makes a 20° angle with the TDM of the C 1s $\rightarrow \pi^*_{CO}$ transition and 70° with the TDM of the C 1s $\rightarrow \sigma^*_{CO}$ transition, and therefore, the intensity of C 1s $\rightarrow \pi^*_{CO}$ transition decreases and that of C 1s $\rightarrow \sigma^*_{CO}$ transition increases.

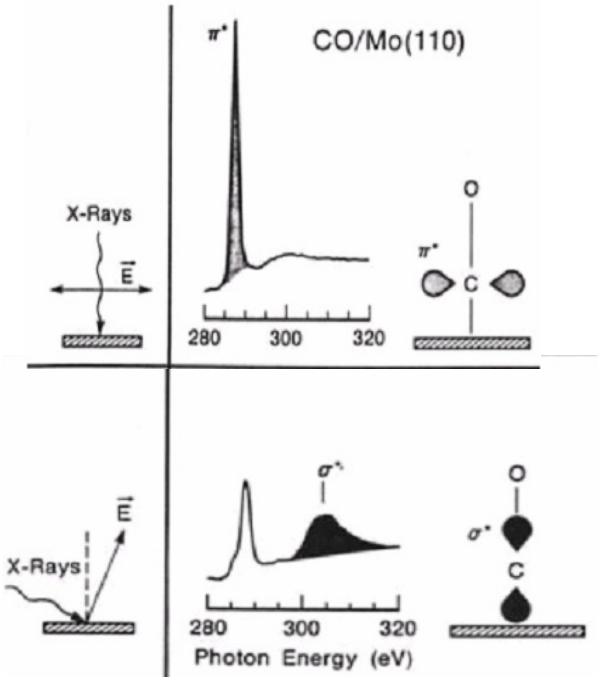

Figure 1.9 Polarization dependence of resonances for normally oriented CO on Mo (110) (Stöhr 1992)

This example demonstrates that if the TDM of a transition is known, the expected angular dependence of NEXAFS spectrum can be predicted. On the other hand, if the angle-resolved NEXAFS spectra are measured, the TDM of that transition can be deduced.

As illustrated in Figure 1.9, the LD of NEXAFS spectroscopy in unsaturated molecules is relatively simple. However, for saturated species such as *n*-alkanes, there are no core $\rightarrow \pi^*$ transitions with a well defined symmetry. In such systems, core $\rightarrow$ σ^* transitions have been used to study the molecular orientation of the saturated species.

LD in saturated systems

The analysis of LD for core $\rightarrow \sigma^*$ transitions is not straight forward. It is complicated by the fact that these transitions are broad and often superimposed on a background, limiting the accurate determination of peak position and intensity.

A number of LD studies have been carried out on *n*-alkane and alkane containing species by NEXAFS spectroscopy, such as SAMs (Hähner et al. 1993; Zharnikov et al. 1999; Crain et al. 2001), LB films (Outka et al. 1987; Outka et al. 1988; Hähner et al. 1991; Kinzler et al. 1994; Kinzler et al. 1995; Schertel et al. 1996), *n*-alkanes (Bagus et al. 1996; Väterlein et al. 1998; Weiss, Bagus et al. 1999; Weiss, Weckesser et al. 1999; Kondoh et al. 2001; Ade et al. 2004), and polyethylene (Stöhr and Outka 1987; Stöhr, Outka et al. 1987). The surface structure and orientation of fluorocarbons have also been investigated by NEXAFS spectroscopy, such as poly(tetrafluoroethylene) (PTFE) (Castner et al. 1993; Ågren et al. 1995; Gamble et al. 2002) and semifluorinated alkane self-assembled monolayers (Genzer, Sivaniah, Kramer, Wang, Korner, Char et al. 2000; Genzer, Sivaniah, Kramer, Wang, Korner, Xiang et al. 2000; Genzer, Sivaniah, Kramer, Wang, Xiang et al. 2000; Xiang et al. 2000; Genzer et al. 2002; Genzer et al. 2003)

An example of using core $\rightarrow \sigma^*$ transitions to investigate LD in NEXAFS spectroscopy is shown in Figure 1.10, in which the NEXAFS spectra of PTFE change as a function of angle α, which is defined as the angle between the projection of the $\boldsymbol{E}$ vector onto the surface and the macromolecular axis, *t* (Ziegler et al. 1994). It is noted that there is a strong polarization dependence of the NEXAFS features. For example, the first feature at 292.8 eV has maximum intensity at $\alpha = 90°$ and greatly reduced

intensity at $\alpha = 0°$. The second feature at 296.2 eV exhibits the opposite behavior. When $\alpha = 90°$, the ***E*** vector is perpendicular to the PTFE macromolecular backbone and parallel to the C-F bonds. Based on this angular dependence the first transition has been assigned to C 1s $\rightarrow \sigma^*_{C\text{-}F}$ transitions and the second one to C 1s $\rightarrow \sigma^*_{C\text{-}C}$ transitions (Ziegler et al. 1994).

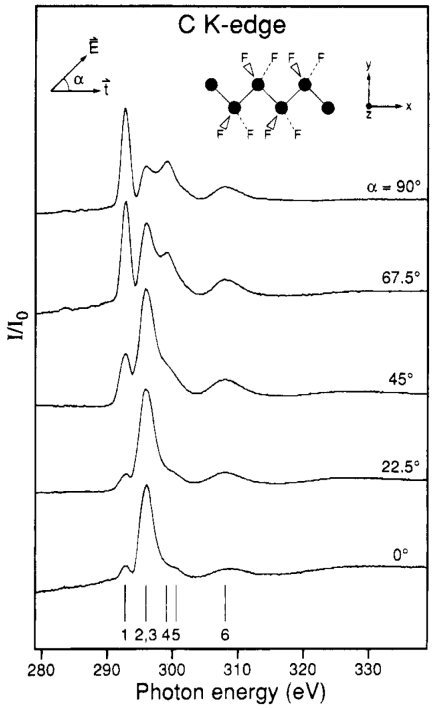

Figure 1.10 Polarization-dependent C 1s near-edge absorption spectra of PTFE at different angle α (Ziegler et al. 1994)

As we have seen from the above examples, the intensity of a NEXAFS resonance is greatly affected by the angle between the ***E*** vector and its TDM. The intensity of a specific transition is also affected by the ellipticity of X-rays.

Ellipticity of X-rays

The ellipticity of X-rays, also called the degree of linear polarization, is defined as (Stöhr 1992)

$$P = \frac{\left|E^{//}\right|^2}{\left|E^{//}\right|^2 + \left|E^{\perp}\right|^2} \tag{1.14}$$

where $E^{//}$ and $E^{\perp}$ are the horizontal and vertical components of the X-ray electric field vector defined as parallel or perpendicular to the electron orbit plane of the storage ring. The degree of linear polarization in the soft X-ray region between 250 and 1000 eV, is 0.8~0.9 for a bending magnet source and $\cong 1.0$ for an undulator source (Stöhr 1992). When the degree of linear polarization of X-rays is not 100%, Eq. (1.12) has to be modified as

$$I \propto P\left|E^{//}\right|^2 \left|\mu_{if}\right|^2 \cos^2\theta + (1-P)\left|E^{\perp}\right|^2 \left|\mu_{if}\right|^2 \sin^2\theta \tag{1.15}$$

where θ is the angle between μ_{if} and $E^{//}$. Therefore, even though the subtended angle between the $\boldsymbol{E}^{//}$ vector and TDM (μ_{if}) of a transition is 90°, due to the non-perfect polarization of the X-rays produced in the bending magnet, the transition intensity will not be zero.

1.4 LD in NEXAFS microscopy

In §1.3 we have demonstrated through examples that LD in NEXAFS spectroscopy can be used to determine the molecular orientation of organic materials. LD can also be applied to NEXAFS microscopy provided that the sample is oriented. If in the NEXAFS spectrum, one or more resonances exhibit LD, then NEXAFS images are obtained at this selected energy. Image contrast is then observed to change with different orientation of $\boldsymbol{E}$ vector.

LD in X-ray microscopy was demonstrated for Kevlar® fiber, a polymer widely used in body armor, sporting equipment, and tire reinforcement (Ade et al. 1993).

Figure 1.11 shows the images of Kevlar® 149 fiber (its chemical structure is based on poly(*p*-phenylene terephthalamide)) at two different orientations of the electric field vector: left-right for the left image and up-down for the right image. These images were acquired at 285.5 eV, the most prominent peak corresponding to C $1s_{(\text{phenyl ring})} \rightarrow \pi^*_{(\text{phenyl ring})}$ transition. This photon energy is selected because the strong peak at 285.5 eV exhibits the greatest LD.

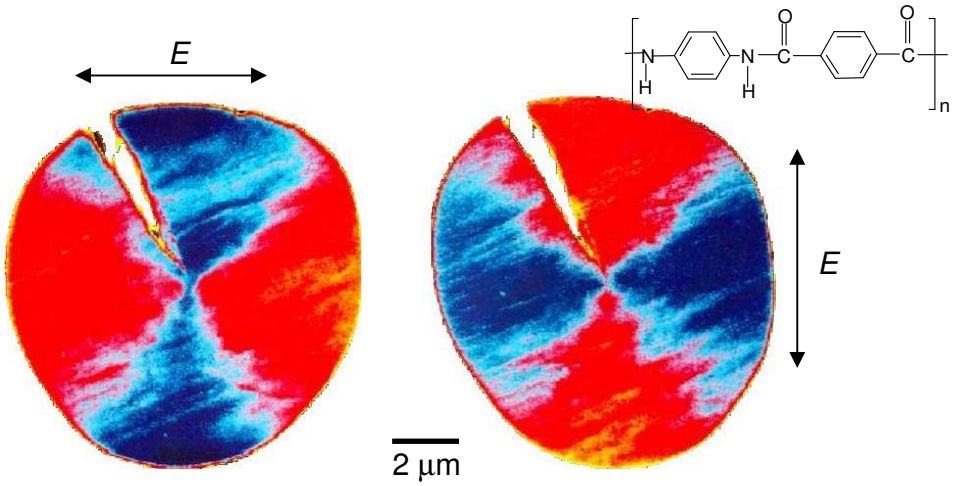

Figure 1.11 Images of Kevlar® 149 fiber acquired at photon energy of 285.5 eV (Ade et al. 1993).

Butterfly-like patterns are observed in both images, which is consistent with the expected radially symmetric structure of the fiber. This pattern rotates with the rotation of the ***E*** vector, arising from the polarization dependent X-ray absorption cross section. Therefore, it is seen that LD in X-ray microscopy can be used to image the molecular orientation of domains. This molecular orientation is also quantified by using LD in X-ray spectroscopy (Smith et al. 1996).

1.5 NEXAFS spectroscopy of n-alkanes

Figure 1.12 presents a typical C 1s NEXAFS spectrum of *n*-alkanes. Below the C 1s IP of *n*-alkanes, two sharp peaks are observed at ~ 288 eV. Above the IP, a broad peak around 292 eV and an even broader peak around 302 eV are observed. The character of these resonances is discussed below.

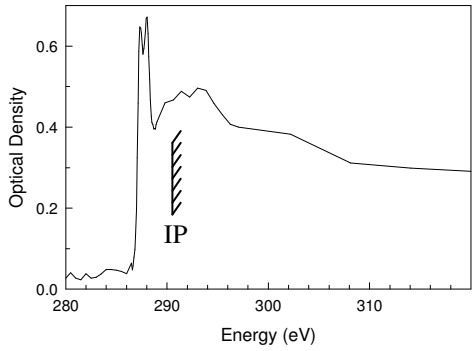

Figure 1.12 C 1s NEXAFS spectrum of *n*-alkanes

NEXAFS resonances below the C 1s ionization potential (IP)

The assignments of the NEXAFS resonances below the C 1s IP of *n*-alkanes are quite controversial. These resonances have been first identified as C 1s $\rightarrow \sigma^*_{C\text{-}H}$ transitions. These assignments are based on the observation that these resonances exhibit strongest intensity when the electric field vector is perpendicular to the chain direction, confirmed by Xα multiple-scattering calculations for the central C atom in propane (Stöhr, Outka et al. 1987). In electron energy loss spectra of linear and branched alkanes, these peaks have been assigned to excitation to a $3p/\pi^*(CH_2)$ energy levels, a mixed Rydberg/valence orbital (of antibonding $\sigma^*_{C\text{-}H}$) (Hitchcock et al. 1986; Hitchcock and Ishii 1987). However, Bagus *et al.*(Bagus et al. 1996) assign the peaks

around 288 eV to C 1s $\rightarrow$ Rydberg transitions based on their *ab initio* self-consistent field Hartree-Fock calculations on an isolated propane molecule.

NEXAFS resonances above the C 1s IP

The resonances observed above the C 1s IP in the NEXAFS spectra for *n*-alkanes are often referred to as shape resonances. There are at least two main different models to describe such phenomena. In a molecular orbital model, the character of these resonances is related to the character of the unoccupied molecular orbital (Hitchcock et al. 1978), in which these resonances are described as C 1s $\rightarrow$ $\sigma^*_{C\text{-}C}$ transitions embedded in the continuum. This approach has the advantage of providing a direct relationship between the molecular structure and its spectrum through the familiar and predictive language of molecular orbital theory.

In a scattering model, the outgoing photoelectron is trapped by a potential well, in which the photoelectron wave is resonantly scattered back-and-forth along the inter-nuclear axis between the absorbing atom and its neighbors (Sette et al. 1984). For this reason, the σ-shape resonances excitation energy is expected to be sensitive to the bond length. The main outcome of this scattering model is the bond-length-with-a-ruler method to correlate the intramolecular bond lengths with the σ-shape resonances (Sette et al. 1984; Hitchcock and Stöhr 1987). However, Piancastelli *et al*. do not like this scattering model on "bond-length-with-a-ruler" (Piancastelli et al. 1987) because multiple excitation, shake-up continuum, and shake-off continuum features can also be considered as the origin of continuum features (Piancastelli 1997).

1.6 Epitaxial growth of organic materials

Well-ordered *n*-alkane samples with lateral molecular orientation are required for angular dependent NEXAFS measurements. The details of this geometry requirement are discussed in §3.1. In this project we employed epitaxial growth to prepare such samples.

Definition of epitaxy

The term epitaxy, deriving from the Greek roots "επι-" meaning "upon" and "ταξι-" meaning "order", refers to the oriented growth of a deposited crystal on the surface of a substrate crystal (Pashley 1965). Epitaxy has been observed in inorganic and organic thin films. When used for inorganic materials, there is a one-to-one relationship between atom positions of the deposited material and the substrate surface (Forrest 1997). Examples of this inorganic epitaxy include growth of Au on thin molybdenite substrate (Stowell et al. 1966), and growth of InSb on GaAs (001) substrate (Zhang et al. 1990). It has long been thought that a lattice mismatching less than 15% between the deposit and substrate is essential to obtain epitaxy (Pashley 1965) in inorganic materials. The lattice mismatching between the deposit and substrate is defined as

$$\Delta = 100(d_c - d_s)/d_s \tag{1.16}$$

where d_c and d_s are the lattice distances of deposit and substrate, respectively (Zhang et al. 1989).

However, when the term epitaxy is used in organic materials, especially long chain molecules, it is different from inorganic epitaxy in two aspects: the requirement of lattice mismatching and the molecular orientation of long chain molecules. The lattice

matching is not a crucial criterion for the epitaxial influence of the substrate on the crystallizing polymer. For example, the epitaxial crystallization of polyethylene was observed on cleaved (001) surfaces of NaCl, NaBr, NaI, KCl, KI, and LiF with the corresponding lattice mismatching ranging from -28 to 27% (Koutsky et al. 1966). On the other hand, in these long chain molecules, orientation is an added variable compared to atomic epitaxy. The molecular orientation of linear molecules can be classified into *lateral* and *normal* orientation, which is illustrated in Figure 1.13. The macromolecular backbone of the long chain molecule is parallel to the substrate surface in *lateral* orientation and perpendicular to the substrate surface in *normal* orientation. The rods in this figure represent the long chain molecules. These are the two extreme cases, beyond these; the molecules can be present on the substrate surface with some tilt angle.

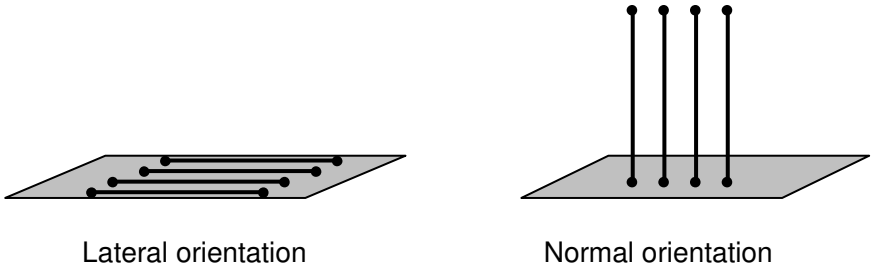

Figure 1.13 The molecular orientations of long chain molecules.

Epitaxy of long chain molecules

Long chain molecules, such as polyethylene and *n*-alkane (the low-molecular-weight homologues of polyethylene) due to their simplicity, have been grown epitaxially. The existence of epitaxy in films of paraffin wax on various substrates was evident 50 years ago (Willems et al. 1956). The first oriented growth of long chain molecules of polyethylene on (001) NaCl was obtained by Willems (Willems et al.

1956), in which the polyethylene was crystallized in its orthorhombic form with the (110) lattice plane of PE parallel to the (001) surface of NaCl. The <001> direction of PE, i.e. the molecular chain axes, is oriented in the two perpendicular <110> directions of the NaCl substrate. Figure 1.14 depicts the oriented growth of a PE single crystal on the (001) surface of a NaCl-type alkali halide single crystal (Mauritz et al. 1978).

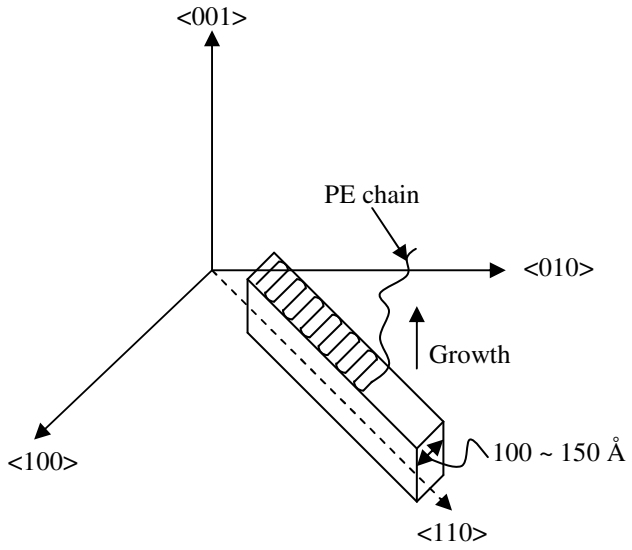

Figure 1.14 Epitaxial growth of a PE single crystal on the (001) face of an NaCl-type alkali halide single crystal (Mauritz et al. 1978).

The PE chain forms a folded structure in such a manner that a chain can be accommodated within a span of 10~15 nm (Mauritz et al. 1978). Since then, a variety of organic epitaxial molecular films have been fabricated and investigated.

Substrates for epitaxy of long chain molecules

A variety of substrates have been used for the growth of long chain molecules. The substrates can be inorganic or organic. Alkali halide substrates (Walton et al. 1968; Wellinghoff et al. 1974) are one of the most commonly used inorganic groups that can

serve as the substrates for epitaxial growth of *n*-alkanes. These substrates are easily prepared and are soluble in water. Organic carboxyl acids (or their potassium salts) with a phenyl ring and different *p*- and *o*- substituents (e.g. benzoic acid and *p*-phenyl benzoic acid) can also be used as the substrates for epitaxial growth of long chain molecules (Wittmann et al. 1983).

Methods to grow long chain molecules epitaxially

Long chain molecules can be epitaxially grown on substrates by different methods, such as solution casting (Koutsky et al. 1966; Wellinghoff et al. 1974; Zhang et al. 1989), vacuum deposition (Ishida et al. 1993), and comelting (Moss et al. 1984; Moss et al. 1985-1986). For example, PE has been epitaxially grown onto a cleaved NaCl surface from solution (Koutsky et al. 1966; Wellinghoff et al. 1974). The results of electron microscopy and electron diffraction of this sample reveal that the PE long chains are laterally oriented on the (001) faces of NaCl with the macromolecular chain direction oriented along the <110> directions of the NaCl substrate surface. Epitaxial growth of PE and *n*-alkanes has also been achieved from solution on aromatic substrates such as anthracene (Wittmann et al. 1981), *p*-terphenyl (Wittmann et al. 1981), and potassium hydrogen phthalate (KHP) (Wittmann et al. 1981; Zhang et al. 1989). Epitaxy of PE has also been obtained on (001) crystal faces of benzoic acid substrates by comelting, in which the substrate and the deposit materials are heated to high temperature and then allowed to cool down together, and the substrate crystallizes first (Wittmann et al. 1983; Moss et al. 1984; Moss et al. 1985-1986; Dorset 1986). Growth of thin films from solution or comelting is simple and easy. However, the

resultant thin films do not have a uniform thickness and it is difficult to control the growth process.

In contrast, physical vapor deposition (PVD) can provide a thin film with uniform thickness and the film morphology can be tailored by deposition parameters, such as substrate temperature, film thickness, deposition rate, *etc*. The process for the formation of a thin film of linear molecules deposited from the vapor phase is illustrated in Figure 1.15 (Kubono et al. 2002).

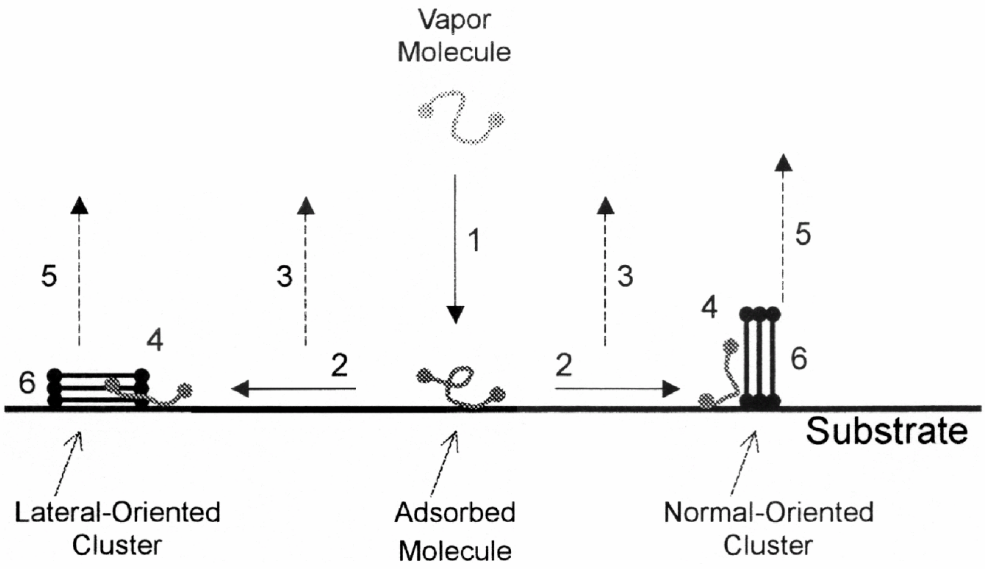

Figure 1.15 PVD process of thin film formation (Kubono et al. 2002)

This process includes (1) adsorption of the vapor molecule on the substrate, (2) surface migration of the adsorbed molecule, (3) re-evaporation of the adsorbed molecule, (4) capture of the adsorbed molecule in an existing cluster, (5) molecule re-evaporation from the cluster, and (6) molecule reorientation. In addition, the adsorbed molecules are present on the substrate surface in several forms, including (1) adsorbed single molecule state in which the molecule can migrate along the surface, (2) lateral-

oriented cluster where all molecules are parallel to the substrate surface, and (3) normal-oriented cluster in which all molecules are perpendicular to the substrate surface (Tanaka et al. 1991; Kubono et al. 2002).

In PVD, the deposition conditions affect the molecular orientation and the domain size of linear molecules. This will be illustrated below.

Molecular orientation of long chain molecules

It is known that the molecular orientation of organic epitaxial thin films is greatly affected by the degree of supercooling (combined effect of the length of the alkyl chain and substrate temperature), the type of substrate, and deposition rate. Therefore, the desired molecular orientation can be tailored by varying these parameters.

The degree of supercooling is found to be the most effective parameter determining the molecular orientation of *n*-alkanes (Matsuzaki et al. 1984; Inoue et al. 1987; Inaoka et al. 1988; Shimizu et al. 1995). It is defined as the difference between the substrate temperature T_s and the *n*-alkane melting point T_m as shown in Eq.(1.17) (Shimizu et al. 1995)

$$\Delta T = T_m - T_s \tag{1.17}$$

Specifically, the molecular orientation is likely to change from a lateral to a normal orientation as the degree of supercooling decreases, i.e. the lateral molecular orientation will form in preference to normal orientation at lower substrate temperature for longer chain molecules. This effect is illustrated in the following examples.

The effect of degree of supercooling on the molecular orientation of tetracontane (*n*-$C_{40}H_{82}$, T_m = 80°C), pentacontane (*n*-$C_{50}H_{102}$, T_m = 94°C), and hexacontane (*n*-$C_{60}H_{122}$, T_m = 98°C) on fused-quartz substrates was explored by wide-angle X-ray

diffraction (WAXD) (Shimizu et al. 1995). It is found at $\Delta T = 233°C$, ($T_s = 134K$), that *n*-$C_{50}H_{102}$ molecules are laterally oriented on the substrate, while at $\Delta T = 32°C$, ($T_s = 335K$), all *n*-$C_{50}H_{102}$ molecules become normally oriented. At ΔT between 32 and 233°C ($T_s = 134$ K ~ 335 K), both lateral orientation and normal orientation are found. The degree of supercooling at which the normal orientation occurred for tetracontane is $\Delta T = 30°C$, ($T_s = 325$ K).

In our experiments, we also observed this degree of supercooling effect on molecular orientation. These details will be given in §3.5. Specifically, at the same substrate temperature (T_s = RT = 21°C), the degree of supercooling for *n*-hexacontane ($T_m = 98°C$) is 24°C higher than that for *n*-hexatriacontane ($T_m = 74°C$), therefore, the *n*-hexacontane molecules are laterally oriented to the NaCl (001) surface, while *n*-hexatriacontane molecules are only partially laterally oriented to the substrate surface.

The type of substrate determines the strength of interaction between the substrate and deposit. The stronger the interaction, the more likely the lateral molecular orientation will occur. Van der Waals interactions are important for epitaxy of organic material (Willems 1958). Coulombic interaction and induced dipolar interaction also play important roles in determining the molecular orientation between the *n*-alkane molecules and ionic substrates, such as alkali halides (Mauritz et al. 1973; Mauritz et al. 1978). For example, when *n*-hexacontane was vacuum deposited on a bare Si_3N_4 membrane surface, a normal molecular orientation was found. However, when *n*-hexacontane was vacuum deposited on a NaCl (001) surface, the *n*-hexacontane molecules were laterally oriented along the substrate surface with the macromolecular axis oriented along the <110> directions of the substrate. This substrate effect on

molecular orientation was also observed when *n*-hexatriacontane molecules were vacuum deposited onto a bare KCl surface (lateral orientation), evaporated Au substrate (normal orientation), and partly Au-covered KCl (lateral + normal orientation) (Ashida et al. 1986). Therefore, the substrate has to be selected carefully in order to obtain desired molecular orientation of *n*-alkanes.

The deposition rate also affects the molecular orientation of *n*-alkane thin films. The higher the deposition rate, the more likely a lateral orientation will occur. The formation of thin films from PVD is a non-equilibrium kinetic process (Venables et al. 1984). The actual vapor pressure of the system is far more than the equilibrium vapor pressure, which "forces" the vapor molecules to kinetically adsorp onto the substrate surface. The higher the deposition rate, the higher the actual vapor pressure of the system. Therefore, a lateral molecular orientation will preferentially form on the substrate surface at higher deposition rate. However, at higher deposition rate, molecules may not have enough time to move along the substrate surface to find their minimum energy positions before they are buried.

In summary, the molecular orientation of long chain molecules is affected by the type of substrates, the chain length of deposit, and the deposition parameters such as substrate temperature (through degree of supercooling) and deposition rate. In order to achieve the desired molecular orientation of *n*-alkane molecules, the above parameters, especially substrate temperature, should be controlled carefully during the deposition.

Domain size of long chain molecules

The substrate temperature and deposition rate not only affect the molecular orientation of linear molecules as described above, but also affect the domain size in the thin films of these molecules.

The substrate temperature can be viewed as supplying activation energy that is required by the deposited molecules to translate to take up the minimum energy substrate surface position. At low substrate temperature, the molecular movement on the substrate is limited due to the lack of thermal energy to promote molecular translation. Molecules can only move a short distance, and many nuclei are formed. At high substrate temperature, the movement of molecules along the substrate surface is enhanced and only a limited number of nuclei are formed, therefore, the average size of the domains becomes larger.

The deposition rate determines the density of the molecules diffusing on the substrate per unit area per unit time. The lower the deposition rate, the less molecular sites for nucleation, therefore, large domains tend to form.

These two factors (the substrate temperature and the deposition rate) are related by the kinetics of the surface diffusion, which is the ratio of the diffusion rate of the deposit molecules D to the deposition rate F (Amar et al. 1995; Ruiz et al. 2004),

$$R = D/F \tag{1.18}$$

The diffusion rate of the deposits along the substrate surface is defined as

$$D = D_0 \exp(-E_a / kT) \tag{1.19}$$

where D_0 is the pre-exponential factor, E_a is the diffusion energy barrier, k is the Planck constant, and T is the substrate temperature. D_0 and E_a are affected by the substrate materials.

The nucleation density, N, the average domain size, A, and the layer coverage Θ are determined by R through

$$N = CR^{-\chi} \approx \frac{\Theta}{A} \tag{1.20}$$

where C is a constant, exponent χ is related to the critical domain size i, which corresponds to *one less* than the number of molecules (or adatoms in the case of inorganic materials) needed to form the smallest stable domains against dissociation (Amar et al. 1995; Ruiz et al. 2004), by

$$\chi = i/(i+2) \tag{1.21}$$

Therefore, the relationship between the substrate temperature and deposition rate can be expressed as:

$$A \propto (\frac{D}{F})^{\chi} = (\frac{D_0 \exp(-E_a / kT_s)}{F})^{\chi} \tag{1.22}$$

From Eq. (1.22), it is clear that increasing the substrate temperature and lowering the deposition rates will increase the average domain size.

1.7 Thin film growth mechanisms

The physical form of the epitaxial deposits, i.e. the morphology of thin films, in terms of continuous thin films or collections of isolated crystals, is a consequence of the thin film growth mechanisms. There are three well-known growth modes (Pashley 1999): (a) monolayer growth (Frank – van der Merwe) – FM mode; (b) three-

dimensional growth (Volmer-Weber) – VW mode; and (c) SK mode (Stranski-Krastanov). The associated names are of those who provided the theoretical backgrounds to the different modes. These modes are illustrated in Figure 1.16.

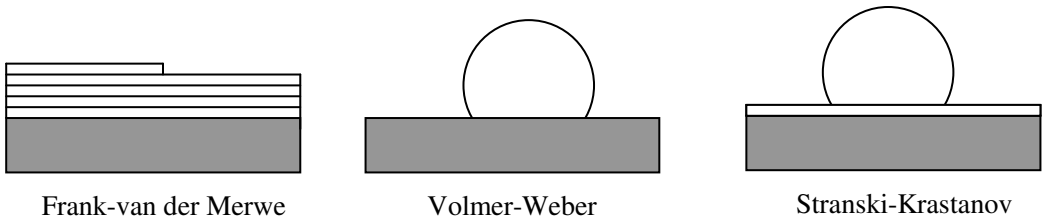

Figure 1.16 Schematic illustration of the Frank-van der Merwe, VW, and SK growth modes for thin films (Pashley 1999)

The primary driving force for generating the different morphologies is the interfacial free energy. If $\gamma_{S\text{-}V}$ is the free energy between substrate and vapor, $\gamma_{F\text{-}S}$ is the free energy between the film and substrate, and $\gamma_{F\text{-}V}$ is the free energy between the film and vapor, then 3D growth mode (Volmer – Weber) is expected when these free energies have the following relationship (Gilmer 1993)

$$\gamma_{F\text{-}S} + \gamma_{F\text{-}V} > \gamma_{S\text{-}V} \tag{1.23}$$

In this case, the bare substrate surface has lower free energy; therefore small clusters are nucleated directly on the substrate to minimize the total free energy. The clusters then grow into three dimensional islands, which in turn coalesce to form a film. The film may have variation in thickness and defects at the interfaces where adjacent clusters coalesce. The Frank-van der Merwe mode describes the condition where the $\gamma_{F\text{-}S}$ is low enough to reverse the sign of Eq. (1.23), i.e. $\gamma_{F\text{-}S} + \gamma_{F\text{-}V} < \gamma_{S\text{-}V}$, so that the deposited materials wet the substrate completely to lower the free energy of this system. Once the first monolayer is formed, the subsequent deposits follow the

monolayer pattern, and therefore the deposited materials form a uniform layer-by-layer structure. The intermediate case, often referred to as SK growth, is a combination of the first two. The SK growth mode cannot be explained by Eq. (1.23) and the effect of strain on the free energy of the film has to be considered. In the initial stages, the deposit is likely to form a very thin uniform film; however, this thin film is under stress due to the misfit between the substrate and deposit. Therefore, additional material aggregates into 3-D clusters on top of this film to relax this stress (Gilmer 1993; Ward 2001).

The above mentioned growth modes are often discussed within the context of inorganic material epitaxy. For example, the growth of SiGe semiconductor thin films on Si (100) surface forms layer-by-layer (Dutartre et al. 1994), while the growth of Ge on Si (001) forms a layer plus island structure (Mo et al. 1990). The organic material epitaxial growth tends to occur as a result of equilibrium conditions (substrate temperature, deposition rate, etc.), and depending on the relative strength of intramolecular interaction ($\gamma_{F\text{-}V}$) and intermolecular interaction ($\gamma_{S\text{-}V}$ and $\gamma_{F\text{-}S}$), the film grows via the above mentioned three mechanisms.

For example, the growth mechanism of organic material PTCDA (3,4,9,10-perylene-tetracarboxylic-dianhydride) on Ag (111) is found to be strongly dependent on the substrate temperature. At T_s = 310 K, this material forms a rather smooth, grain-like thin layer on the Ag (111) surface, through a layer-by-layer (FM) growth. At intermediate temperature (T_s = 340 K), the increased grain size was observed, covering the Ag (111) substrate regularly. At high temperature (T_s = 420 K), large, isolated

crystallites on a complete coverage of two strained layers were observed, i.e. Stranski-Krastanov growth mode occurred at high substrate temperature. (Chkoda et al. 2003)

In contrast, the growth mechanism of thermally evaporated pentacene thin films is generally described by a Volmer-Weber type of process, where the nucleated islands have a three-dimensional growth mode without formation of an initial complete monolayer (Chang et al. 2003).

In summary, the morphology of an organic thin film is determined by the different growth mechanisms, which are subject to the thin film growth conditions. In order to obtain the desired morphology, the growth conditions of thin films, such as deposition rate and substrate temperature, have to be controlled carefully.

1.8 Research objectives

LD for the C 1s $\rightarrow \sigma^*_{C\text{-}C}$ transition in the NEXAFS spectrum of *n*-alkanes

NEXAFS spectroscopy has proved to be a powerful technique for investigating the orientation of molecules and polymers on surfaces. As discussed in §1.3, for polymer containing π^* unoccupied orbitals, such as rubbed polyimide (Samant et al. 1996; Cossy-Favre et al. 1998; Stöhr et al. 1998), a good relationship between polymer orientation and NEXAFS resonances has been established since the absorption bands of core $\rightarrow \pi^*$ transitions are strong and narrow and the direction of the transition dipole moment of such transitions is well defined (Stöhr 1992).

However, for long chain molecules such as polyethylene, *n*-alkanes, and other alkane species that only have σ^* unoccupied orbitals, the relationship between the molecular orientation and the C 1s $\rightarrow \sigma^*$ transition is poorly understood. Two models

are widely employed to derive the molecular orientation of long-chain molecules from the NEXAFS spectra. In the building block (BB) model proposed by Outka, Stöhr, and co-workers (Outka et al. 1987; Stöhr and Outka 1987; Outka et al. 1988), a molecule is viewed as an assembly of diatomic subunits or "building blocks". *n*-Alkanes are treated as the assembly of individual C-C "building blocks", and the angle dependence of the carbon 1s $\rightarrow \sigma^*_{C\text{-}C}$ transition arises from the sum of the transition dipole moments (TDMs) of the individual C-C building blocks, each TDM aligned along each C-C bond. Since this model implicitly considers the electronic structure as the sum of the properties of specific bonds between diatomic pairs, this is in essence a valence bond description. In contrast to this BB model, Hähner *et al*. (Hähner et al. 1991; Kinzler et al. 1994) have used a molecular orbital (MO) approach to consider the angle dependence of the C 1s NEXAFS spectra of *n*-alkanes. A molecular orbital can be delocalized over all or part of a molecule and not (necessarily) localized to a specific bond pair. By using these two models, from almost identical NEXAFS spectra of LB films of Cd-arachidate, Outka *et al*. (Outka et al. 1988) calculate that the molecular chain is normal to the substrate surface, while a tilt angle of 30° of the molecular chain relative to the substrate surface normal is found by Kinzler *et al.* (Kinzler et al. 1994)

The predicted angle dependence for the carbon 1s $\rightarrow \sigma^*_{C\text{-}C}$ transition in the NEXAFS spectrum of a linear alkane molecule based on the BB and MO models is presented in Figure 1.17. This angle dependence is expressed as a function of the angle between the $\boldsymbol{E}$ vector and the macromolecular chain axis of the *n*-alkane. The BB model is constructed by adding up the bond-specific contributions where the TDM is aligned along individual C-C bonds and the sum is derived by use of the appropriate C-

C-C bond angle (Teare 1959; Hu et al. 1989). The MO model assumes that the TDM is directed along the chain axis as a delocalized $\sigma^*_{C\text{-}C}$ molecular orbital (Hähner et al. 1991). The intensity scale is defined according to $I = A\ cos^2\theta$, where A is assumed to equal to 1.

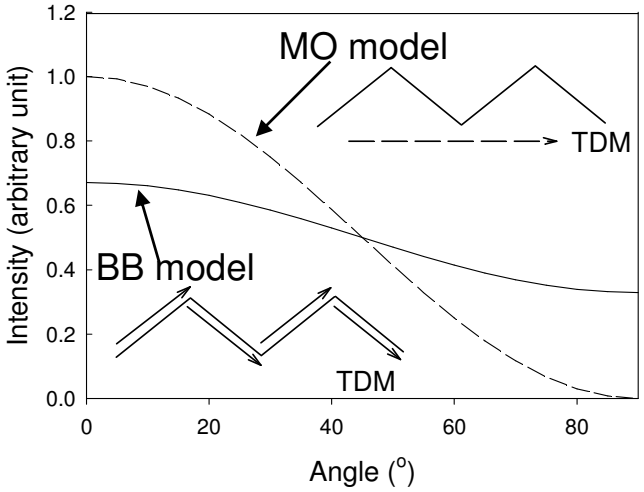

Figure 1.17 The possible relationship of the intensity of C 1s $\rightarrow \sigma^*_{C\text{-}C}$ transition and the included angle between TDM and the ***E*** vector of X-rays by using the BB model (solid line) and the MO model (dashed line)

Both models show that the intensity of the Carbon 1s $\rightarrow \sigma^*_{C\text{-}C}$ transition is at a maximum when the electric field vector is directed along the chain axis ($\theta = 0°$) and reaches a minimum when the electric field vector is perpendicular to the chain axis ($\theta = 90°$). The key difference between these models is the magnitude of the change. In the MO model, the intensity of the Carbon 1s $\rightarrow \sigma^*_{C\text{-}C}$ transition is predicted to go to zero at $\theta = 90°$ while this transition never goes to zero intensity in the BB model. The difference between models can be understood by considering the $\cos^2\theta$ dependence for bond-specific contributions in the BB model.

Calculated LD for NEXAFS resonances of *n*-alkanes

The second research objective of this project is to understand the LD for the NEXAFS resonances of *n*-alkanes by carrying out theoretical calculations. Generally, for the NEXAFS resonances below the C 1s IP, we want to understand:

a. How many features are present below the C 1s IP? The early NEXAFS spectra of n-alkanes only show one broad peak below the C 1s IP (Stöhr, Outka et al. 1987), while our high resolution NEXAFS spectra reveal two sharp peaks. However, the least-square fit of our angular dependent NEXAFS spectra exhibit four features (see §3.2.6).

b. What is their character? As introduced in §1.5, in the condensed phase *n*-alkanes, the NEXAFS resonances of *n*-alkanes below the C 1s IP have been assigned as valence transition, Rydberg transition, or mixing of valence and Rydberg. We want to determine the character of these resonances.

c. The most important part in this research objective is to understand the LD of each resonance below the IP.

For the NEXAFS resonances above the C 1s IP, we wish to gain some insight of the TDM of these transitions from theoretical calculations and correlate the experimental results with theoretical calculations.

Rationalize the *n*-alkane thin film growth

As introduced in §1.6, we are using epitaxial growth to prepare *n*-alkane thin films for our spectroscopy experiments. However, the molecular orientation and growth mechanism of organic molecules are greatly affected by the deposition parameters. Therefore, the last objective of this project is to understand the nature of deposition in *n*-alkane thin films, i.e. how the deposition parameters, such as the substrate

temperature, the type of substrates and the chain length of *n*-alkane, affect the thin film morphology, growth mechanism, and the orientation of these molecules in the thin films.

Approaches to study

As described in §1.8, the BB and MO models are used to determine the relationship between the molecular orientation and C 1s $\rightarrow \sigma^*_{C\text{-}C}$ transition in *n*-alkane molecules. In order to determine which model gives a better description, well-ordered *n*-alkane thin films with lateral orientation and large domain size are needed. The detailed substrate and thin film preparation methods are given in §2.2 and §2.3. The prepared thin films were then characterized by Scanning Transmission X-ray Microscopy. The description of these microscopes is given in §2.4. The detailed results are presented in Chapter 3.

As well, *ab initio* calculations are carried out to (a) elucidate the character of each NEXAFS feature of *n*-alkane molecules; (b) determine the LD of each feature. These calculations were carried out on propane and fairly long nonane molecules in both the gas and condensed phases. By correlating with the experimental results, the character and LD for each feature is then determined. The calculation method is described in detail in §2.5 and the result is presented in §3.4.

In order to understand the nature of deposition in *n*-alkane thin films, the deposition parameters such as substrate temperature and the chain length of *n*-alkane were explored. These effects on the morphology and molecular orientation of *n*-alkane samples are given in detail in §3.5.

Chapter 2 Experimental and Theoretical methods

As discussed in Chapter 1, well-ordered *n*-alkane thin films with a lateral orientation and large domain size are needed in order to measure the LD in the NEXAFS spectra of *n*-alkanes. The selection of the *n*-alkane molecules examined is given in §2.1, and the preparation of the substrates and *n*-alkane thin films on these substrates is presented in §2.2 and §2.3, respectively. The techniques of Scanning Transmission X-ray Spectroscopy and Microscopy are presented in §2.4. These techniques are used to characterize the *n*-alkane thin film morphology and molecular orientation. Theoretical methods for calculating the NEXAFS spectra of *n*-alkanes are introduced in §2.5.

2.1 n-Alkane candidates

Long-chain *n*-alkanes are a basic type of organic compound. Long alkyl chains play important roles in the formation of ordered structures in molecular assemblies such as LB films, SAMs, liquid crystals, and biomembranes. The *n*-alkane molecules used in this project are *n*-hexacontane (*n*-$C_{60}H_{122}$, HC) and *n*-hexatriacontane (*n*-$C_{36}H_{74}$, HTC) with their purity of 98% and 98%, respectively, purchased from Sigma-Aldrich and no further purification was carried out. These molecules are solid at room temperature, have low vapor pressure, and are compatible with high vacuum.

2.2 Preparation of substrates

As introduced in §1.6, inorganic and organic materials can be used as the substrates for epitaxial growth of *n*-alkane thin films. These substrates can be in polycrystalline form or single crystal. The inorganic substrates used in this project are single crystals of NaCl (surplus FTIR windows) and evaporated KCl (Aldrich Company, 99.99%) thin films. Organic substrates are potassium hydrogen phthalate (BDH Chemicals, 99.9%), benzoic acid (BDH Chemicals, 99%), *p*-Br benzoic acid (Aldrich, 98%), *p*-phenyl benzoic acid (Aldrich, 95%) and terephthalic acid (Aldrich, 98%). All chemicals were used without further purification.

In this project, several approaches are used to prepare crystalline substrates. A fresh substrate can be prepared by depositing it as a thin film in a high vacuum chamber, where the substrate morphology can be controlled by adjusting the deposition rate, substrate temperature and thickness. Other methods to prepare substrates involve cleaving the single crystal in air to expose a fresh surface for the thin film deposition, casting of dilute substrate solution, followed by solvent evaporation, or comelting the substrate material with deposit material (Wittmann et al. 1983; Moss et al. 1984). These approaches are outlined below.

(1) Crystalline substrates prepared by PVD: Potassium chloride (KCl), *p*-phenyl benzoic acid (*p*-PBA), and terephthalic acid (TA). These species were evaporated onto a clean Si wafer in vacuum with a thickness of 20 nm. The resultant thin layers of KCl, *p*-PBA, and TA were used as a substrate for epitaxial growth of *n*-alkanes. This method provides a clean and fresh substrate surface for the growth of *n*-alkane thin films.

However, the surface of the deposited thin films might have a different crystal structure from the bulk, and may lack long range crystalline order.

(2) Substrates prepared by cleaving: Single crystals of NaCl were cleaved with a razor blade and quickly transferred into the vacuum chamber. The freshly exposed face is used as a substrate for the deposition of *n*-alkane. The cleaved surface may not be atomically flat, having kinks and ledges (Ward 2001). However, the kinks and ledges can initiate the nucleation process of the crystal growth (Ikeda et al. 2004).

(3) Substrates prepared by comelting: A benzoic acid (BA) substrate cannot be used in vacuum due to its high vapor pressure (133 Pa at 96°C). Comelting is a thin film preparation method based on the different melting points of the deposit and substrate. The melting point of the BA substrate (122°C) is higher than that of the deposit (96°C in the case of HC). When decreasing the temperature, the substrate will first crystallize and the HC deposit will then crystallize on the substrate surface. The advantage of the comelting method is there is no surface contamination.

(4) Substrates prepared by solution casting: Substrates with high vapor pressure or comparable melting point with the deposit cannot be prepared by vapor deposition or by comelting. Solution casting is possible. A dilute solution of substrate molecule is cast onto a clean glass slide and the solution is allowed to evaporate in the saturated solvent environment. The resultant thin films of substrates are then transferred to the vacuum chamber and used as a substrate for the epitaxial growth of linear alkanes. The substrates prepared by solution casting were potassium hydrogen phthalate (KHP) and *para*-bromo benzoic acid (*p*-BBA).

2.3 Preparation of n-alkane thin films

Thin films of *n*-alkanes were prepared on different substrates, described above, by comelting with the substrate, physical vapor deposition in vacuum, and solution casting. In general, the solution casting and comelting methods give a rough surface and the thin film is not uniform. The solution casting method was only used before the installation of the vacuum chamber, which was later found to produce superior thin films. The comelting method was only used for the BA substrate because of its high vapor pressure, not compatible with the vacuum. The sample preparation using a vacuum chamber is described below.

Vacuum chamber

Figure 2.1 (left) shows the evaporation setup in the vacuum chamber (DataComp. Scientific). A diffusion pump is used to provide the vacuum in the chamber (typically ~ 10^{-7} torr). A tungsten boat is used to hold the sample and provides resistive heating to evaporate the sample. A substrate holder is placed about 15 cm above the tungsten boat to support the substrate. A shutter, 5 cm above the tungsten boat, is moved into position before the sample starts evaporation and after the desired sample thickness is reached. A quartz crystal microbalance is mounted beside the substrate holder with the same height as the substrate holder. This crystal microbalance is used to monitor the deposition rate and sample thickness. The deposition rate (R) is a function of the source temperature according to

$$R = P\sqrt{2\pi mkT} \tag{2.1}$$

where P is the pressure of the vacuum chamber, m is the mass of the molecule, k is the Planck constant, and T is the evaporation source (tungsten boat) temperature.

Therefore, in the process of the formation of thin films, the deposition rate is controlled by adjusting the heating power of the tungsten boat.

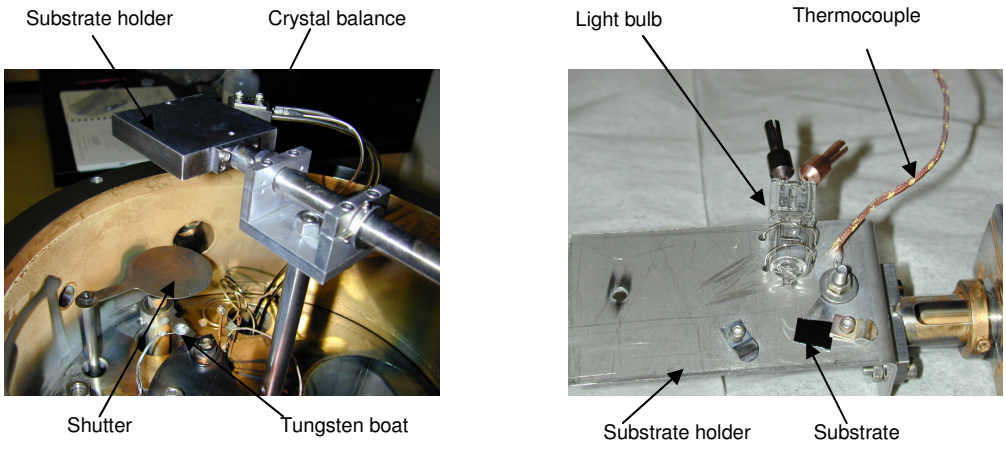

Figure 2.1 (left) Evaporation setup in the vacuum chamber. (right) Picture of modified substrate holder with light bulb heating system and a thermocouple

In order to control the substrate temperature during the sample deposition, a modified substrate holder is used (Figure 2.1 (right)). The heating of the substrate is provided by a simple light bulb that is mounted in the substrate holder. A thermocouple, mounted beside the light bulb, is used to measure the substrate temperature.

Preparation of *n*-alkane thin films

The preparation of *n*-alkane thin films by comelting and physical vapor deposition is described below.

(1) Comelting alkane with BA: A mixture (50:50) of BA and an *n*-alkane (HC) was heated on a hot plate until melting. The sample was then allowed to cool down in the air.

(2) *n*-alkane films prepared by PVD on different substrates: a small quantity (~10 mg) of the *n*-alkane sample was placed in the tungsten boat. The sample was then vaporized and deposited onto the substrate to the desired sample thickness, e.g. 100 ~ 200 nm for C 1s edge, as required for transmission measurements. When the *n*-alkane molecules are evaporated onto substrates at elevated substrate temperature, the substrates were preheated to a desired temperature and kept at that temperature during the deposition.

After the alkane thin films had been prepared, the substrate was removed and the *n*-alkane thin film had to be transferred to a Si_3N_4 membrane window (Silson Ltd.) for X-ray microscopy. The *n*-alkane thin film can be separated by dissolving the substrates. Substrates such as solution-cast KHP thin films, air-cleaved NaCl single crystals, and evaporated KCl thin films were dissolved in Millipore water, the BA substrate from comelting and *p*-BBA substrate from solution-cast were dissolved in pure ethanol, *p*-PBA substrate from evaporation was dissolved in acetone, and TA substrate from evaporation was dissolved in dimethyl sulfur oxide. The floating *n*-alkane thin films were picked up on Si_3N_4 membrane windows.

All substrates and *n*-alkane thin films were handled in dust free conditions in a laminar flow hood.

2.4 Characterization of n-alkane thin films

The morphology of *n*-alkane thin films prepared on different substrates and at different substrate temperature in vacuum was investigated by Scanning Transmission X-ray Microscopy (STXM). The orientation of *n*-alkane molecules in these thin films was investigated by polarization-dependent NEXAFS spectroscopy, recorded in the STXM microscope.

2.4.1 Scanning Transmission X-ray Microscopy (STXM)

Two STXM microscopes have been employed for this research: the NCSU-McMaster-Dow-polymer STXM (beamline 5.3.2 at Advanced Light Source (ALS), Berkeley, CA) on a bending magnet beamline, and Molecular Environmental Science STXM (beamline 11.0.2 at ALS, Berkeley, CA) on an Elliptically Polarized Undulator (EPU).

2.4.1.1 NCSU-McMaster-Dow-Polymer STXM

Figure 2.2 shows a schematic drawing of the NCSU-McMaster-Dow-Polymer STXM of beamline 5.3.2 at Advanced Light Source (Hitchcock 2003). The X-rays are emitted by the electrons when their trajectories are bent by a bending magnet. These X-rays are then monochromated by a spherical grating monochromator. The monochromated X-rays are focused by a Fresnel zone plate, which is a circular, variable line density, transmission diffraction grating. The sample is raster-scanned through the focal plane by a piezo stage. The transmitted X-rays are converted by a phosphor screen to visible photons, which are then detected by a photomultiplier tube. The spatial resolution of STXM can be as good as 35 nm and the energy resolution is about 100 meV. This system can be operated in air, vacuum, or helium environment (Ade et al. 2003; Kilcoyne et al. 2003).

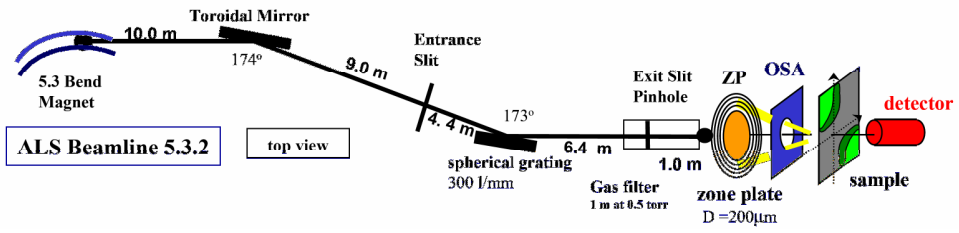

Figure 2.2 Schematic drawing of STXM at ALS beamline 5.3.2 (Hitchcock 2003)

In order to suppress the unwanted diffraction orders that would decrease the available signal-to-background ratio and allow the positive first diffraction order to pass, a zone plate central stop and an order sorting aperture (OSA) are used. The central stop is fabricated in the zone plate. The OSA, a slightly smaller pinhole, is placed between the zone plate and the sample. Figure 2.3 illustrates the role of a central stop and an OSA in isolating the radiation focused in the first diffractive order of a Fresnel zone plate (Kirz et al. 1995).

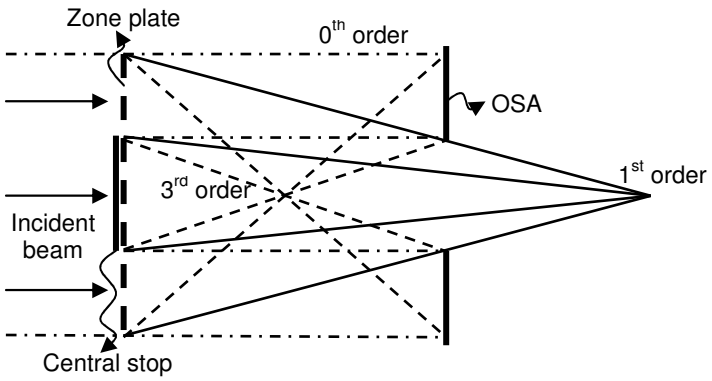

Figure 2.3 Schematic diagram of central stop and OSA in isolating the 1st order diffraction of a Fresnel zone plate (Kirz et al. 1995)

In these experiments, the OSA needs to be aligned properly to eliminate the higher order contamination, and the sample thickness has to be controlled in order to obtain reliable, trustworthy spectra. These factors will be discussed below in §3.3.

2.4.1.2 Molecular environmental science (MES) STXM

The molecular environmental science STXM is operating on an elliptically polarized undulator (EPU) beamline 11.0.2 at ALS, Berkeley. Except for the source of X-rays, MES-STXM is similar to polymer STXM, described above in §2.4.1.1. This section will focus on the structure of a linear undulator and an EPU and how the X-rays

are produced. A linear undulator is a periodic array of magnets as shown in Figure 2.4(a) (Top). Each individual magnet applies a force to the moving electrons, causing a slight deviation of their direction. The periodic magnet array thus causes small undulations of an electron that would otherwise travel along a straight line. The X-rays are thus produced when the electron moving direction is oscillated in this undulator (Margaritondo 2002). The EPU, whose magnetic structure is shown in Figure 2.4(b), is different from a linear undulator in that it is composed of four quadrants. Each quadrant is made up of four blocks of magnetic material with different magnetic field directions (Marks et al. 1998; Young et al. 2002). These allow for the control of the X-ray polarizations, as described below.

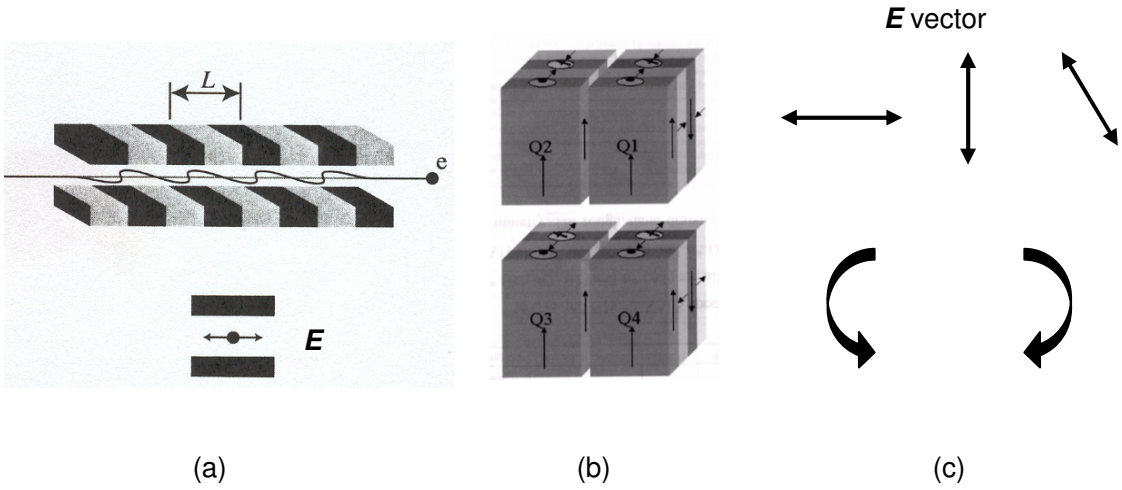

Figure 2.4 (a) (Top) Schematic of a linear undulator, (bottom) Electric field vector of X-rays produced from a linear undulator (Margaritondo 2002); (b) Magnetic structure of an EPU; (c) Electric field vector of X-rays produced from an EPU (Young et al. 2002)

2.4.1.3 Polarization of X-rays

The polarization and the degree of linear polarization of X-rays are very important in this project since we are going to measure polarization dependent NEXAFS spectra of the *n*-alkane thin films.

When the X-rays are produced by a bending magnet (Figure 2.5), from the side (ring plane) the electron looks like an oscillating charge (Margaritondo 2002). The ***E*** vectors of these X-rays are linearly polarized in the horizontal plane. The degree of this linear polarization is typically about 85% ~ 90% (Margaritondo 1988; Stöhr 1992; Margaritondo 2002). When viewing from a different point slightly above or below the ring plane, the circulating electron is seen moving along an elliptical curve, thus, the ***E*** vector is elliptically polarized above and below the plane, and these photons have circular polarization.

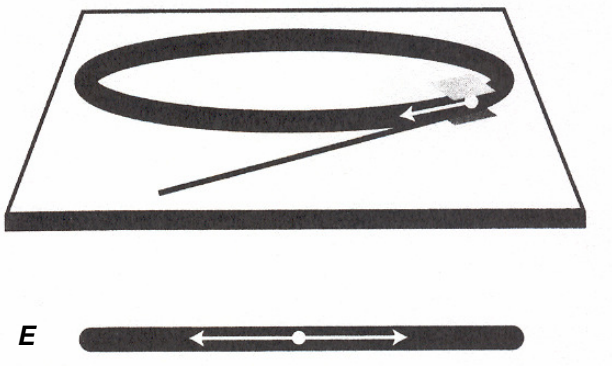

Figure 2.5 (top) Emission of X-rays by a bending magnet, (bottom) Seen from the side, the E vector of X-rays is linearly polarized

When the X-rays are produced by a linear undulator, as shown in Figure 2.4(a) (bottom), the electron looks like an oscillating charge in the horizontal plane; therefore, the ***E*** vector is linearly polarized. However, using EPU, a variety of polarizations (Figure 2.4(c)) can be obtained, from linear horizontal (0°) to linear vertical (90°)

continuously, and right circular polarization (RCP), left circular polarization (LCP) (Marks et al. 1998). The degree of linear polarization of the ***E*** vector for EPU is 100% +0/-1% (Kortright 2005).

Since the linear polarization of X-rays can not be changed in a bending magnet beamline, in order to obtain the angular dependent NEXAFS spectra, the sample has to be rotated around the surface normal from 0° to 180° to obtain the angular dependent NEXAFS spectra. In the EPU beamline, the polarization of X-rays can only be changed from 0° to 90°. The initial sample position has to be adjusted such that at EPU = 0, the ***E*** vector is parallel to the macromolecular backbone of the *n*-alkane molecules. The sample is then kept still, and the polarization of X-rays is changed between horizontal and vertical. Therefore, in both bending magnet-STXM and EPU-STXM measurements, a rotatable sample holder is needed to change the orientation of samples relative to X-rays. This will be described below.

2.4.1.4 Rotatable sample holder

Figure 2.6 shows the rotatable sample holder we made and used in the polymer-STXM measurements. This holder is composed of a support base and a rotatable handle, on which the sample is mounted. This holder allows for the rotation of the sample around the beam axis and enables us to take angular resolved NEXAFS spectra of laterally oriented *n*-alkane thin films.

In the above mentioned two STXMs, a rotatable sample holder had to be used to obtain the angular dependent NEXAFS spectra through the entire 180° angles. This is not necessary at the Canadian Light Source because the EPU beamline is built to be capable of changing the linearly polarized light from 0 to 180°.

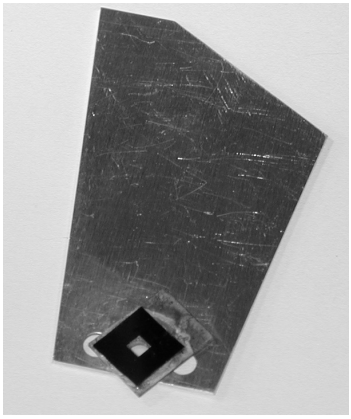

Figure 2.6 Rotatable substrate holder used in BL 5.3.2 and 11.0.2 STXM

2.4.2 NEXAFS microscopy and spectroscopy

From STXM, X-ray absorption images and NEXAFS spectra can be obtained. For imaging at a specific energy, the transmitted X-rays are recorded as a function of sample position by scanning the sample in the focal plane under computer control. The NEXAFS spectrum of a sample can be obtained directly by focusing on a spot and scanning the monochromator across the absorption edge, this is the so-called point scan. The point scan spectrum provides a quick estimation of what the sample is. The NEXAFS spectrum can also be acquired indirectly from line scan (Hitchcock 2003) or an image sequence (Jacobsen et al. 2000). Line scan is similar to the point scan except that the X-ray photons are scanned on a line across some structures in a sample. Figure 2.7 illustrates how the optical density NEXAFS spectrum can be obtained from line scan. First, a line including part of the sample and an open area is defined in a NEXAFS image (red line in the left image). And then this line is scanned across the absorption edge at a series of energies. In the case of *n*-alkane samples, the scanning

energy was 280 – 320 eV. The I and I_0 signals were integrated in the line scan image (middle) and converted to OD according to Eq. (1.5), the NEXAFS spectrum (right) from line scan is then obtained. This procedure is done in aXis2000 program (Hitchcock 2000).

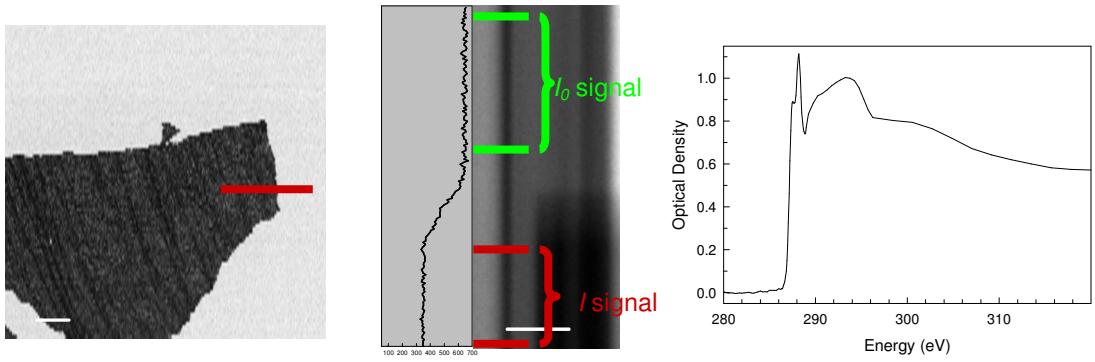

Figure 2.7 (left) X-ray absorption image at 287.6 eV of HC sample prepared on cleaved NaCl substrate. (middle) The line scan image based on the line defined in the left image. (right) NEXAFS spectrum obtained from the line scan.

In an image sequence, a series of images are taken throughout the near-edge spectral region. The spectrum can then be obtained by integrating signals from regions within this sequence of images, which is illustrated in Figure 2.8. This image sequence was obtained from a hexacontane sample. The images on the left were recorded at different energies, corresponding to the pre-edge, the C 1s $\rightarrow \sigma^*_{C\text{-}H}$ transition, the C 1s $\rightarrow \sigma^*_{C\text{-}C}$ transition, and the C 1s $\rightarrow$ continuum, respectively. The marked triangle area is an open area, through which the I_0 signal can be obtained. The square and circle areas are the two orientation components for this sample, which are best visualized in the image at 287.6 eV. The C 1s NEXAFS spectra extracted from the square and circle areas is shown in the right-hand figure.

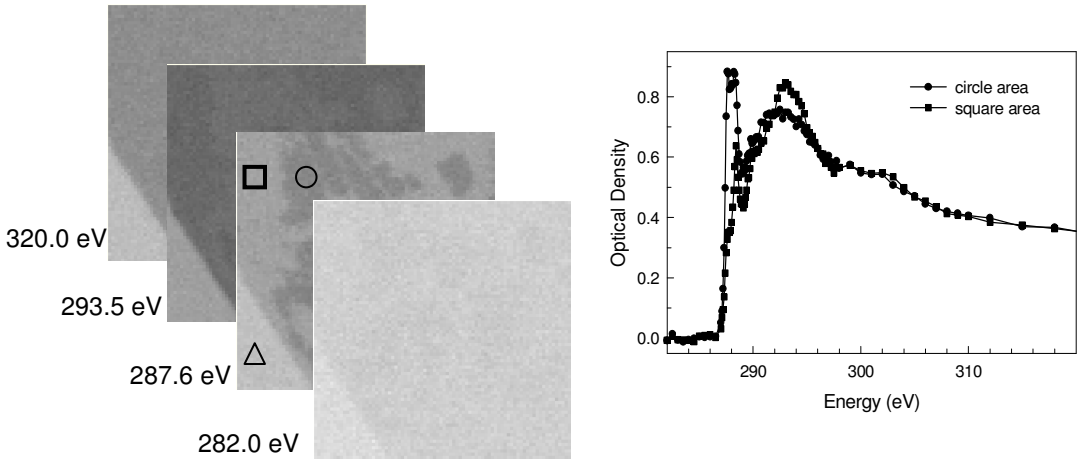

Figure 2.8 Stack requisition (left): a series of images are taken at different energies; (right) the NEXAFS spectra extracted from the square and circle areas

Radiation damage is a significant concern for *n*-alkane samples. If the sample is damaged, the spectrum is not trustworthy. A detailed radiation damage study is given in §3.2.1. In general, to avoid the accumulation of radiation doses that would cause damage to the sample, each spectrum was acquired from a unique sample area.

In line scan and an image sequence, the radiation damage can be reduced by defocusing (in line scan) and scanning a large sample area (in an image sequence) to attenuate the radiation doses. The NEXAFS spectrum obtained from an image sequence often shows a better signal-to-noise ratio compared to line scan because in an image sequence the signal is integrated over a large sample area, and thus one obtains better statistics (Urquhart et al. 1999). All spectra presented in this thesis are obtained from an image sequence if not otherwise specified.

Figure 2.9 shows the transmitted signals through sample I and through an open area I_0. In the I and I_0 signal curves, there is a dip at ~285 eV, due to the absorption by carbon contaminants deposited on the optical elements. In order to account for this

carbon absorption, the NEXAFS spectra are reported as optical density (OD) versus energy (eV) according to Eq. (1.5) OD = -ln (I/I_0), therefore, the decay due to source contamination can be normalized. On the other hand, the X-ray flux produced by the synchrotron radiation decays with time, i.e. the flux varies within the time scale of a spectrum acquisition. In order to eliminate this flux variation effect on the spectrum, the incident flux spectrum I_0 and sample spectrum I should be obtained simultaneously. Therefore, a hole is always included in the sample within the imaged region and the spectrum extracted from the hole is used as the incident flux I_0.

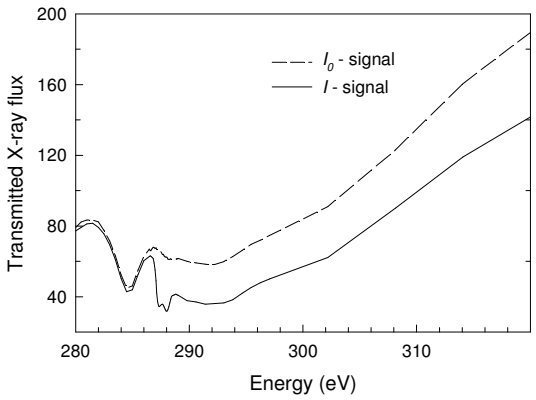

Figure 2.9 I_0 signal (dashed line) through the Si_3N_4 membrane and I signal through the sample (solid line) in the STXM microscope chamber at beamline 5.3.2 at ALS

At the carbon 1s edge, the energy calibration is done by introducing CO_2 into the microscope chamber while the sample is in place, allowing the spectrum of the sample and the calibrated CO_2 to be recorded simultaneously. The two absorption peaks in CO_2 corresponding to the C 1s → 3s ($\nu = 0$) (292.74 eV) and C 1s → 3p ($\nu = 0$) (294.96 eV) are used for calibration (Ma et al. 1991).

2.5 Theoretical methods

In order to study the LD of the NEXAFS features of *n*-alkanes, *ab initio* calculations were carried out on single alkane molecules (propane and nonane) and alkane clusters (propane and nonane clusters). The theoretical calculation results are presented in §3.4.

Ab initio calculations were carried out by using Kosugi's GSCF3 (Gaussian self consistent field version 3) package (Kosugi et al. 1980). These calculations are based on the Improved Virtual Orbital approximation (IVO), which explicitly takes into account the core hole in the Hartree-Fock approximation and are highly optimized for inner-shell excitation and ionization calculations (Hunt et al. 1969). In this approach, the 1s electron is removed directly from a molecular orbital, corresponding to a specific 1s orbital, as specified by the user. The improved virtual orbital provides a good approximation to the term value of the core excitation features at a specified core site (Kosugi et al. 1980).

The calculation is performed in three steps (Kosugi et al. 1980; Gordon et al. 2003). The first step calculates the eigenvectors and eigenvalues of molecular orbitals (MOs) in the ground state, which is also used to identify the core MO that will lose the electron. In the second step, the core ionized state of the molecule is calculated by removing the specified core electron and allowing the system to relax and reorganize in the presence of the core hole. The difference between the total energy of the ground state (first step) and core-ionized state (second step) corresponds to the ionization potential of that specific core electron in the ΔSCF approach. In the third step, the core excitation energies and transition probabilities are determined within the IVO

approximation. The accuracy of the core excitation energies depends on the basis set used. This calculation provides term values, oscillator strengths, excited orbital sizes, and the distribution of oscillator strengths along the x-, y-, and z- axis, and the orbital composition of each molecular orbital. The oscillator strength is the transition probability, which is related to the X-ray absorption cross section by Eq. (1.2) and Eq. (1.4), and to the experimental *OD* by Eq. (1.8). The term value is defined as the difference between the ionization potential and transition energy

Term value = IP – transition energy (2.2)

In order to theoretically study the LD of the NEXAFS features of *n*-alkanes, the character of each feature has to be clear. For the study of LD for NEXAFS features above the C 1s IP, minimal basis set IVO calculations were performed on an isolated nonane molecule (§3.4).

As shown in §1.5, the arguments on the character of NEXAFS features below the C 1s IP focus on whether the Rydberg transition is attenuated in the condensed phase. In order to differentiate the Rydberg and valence character, a calculation of the separation between the singlet and the triplet state is useful. If the core electron is excited to a pure Rydberg orbital, the interaction with other valence electrons in the molecules will be small. In contrast, if the core electron is excited to a valence orbital, there will be a much stronger interaction with the other electrons. By the Pauli exclusion principle, the excited electron will have less repulsion if it is in a triplet valence excited state than in a singlet valence excited state (Urquhart et al. 2005). Therefore, a greater difference in the singlet-triplet excitation energies is expected if the optical orbital has a larger valence character. An approximate guide as suggested by

Kosugi is that a singlet-triplet energy separation smaller than 0.05 eV is usually considered as Rydberg character (Kosugi 2000; Urquhart et al. 2005). In the fourth step of the calculation, the term value and oscillator strength, etc. are calculated as if the spin of the excited core electron changes, $\Delta S = 1$, as for a triple excited state.

The IVO calculations have the potential for spurious Rydberg – valence mixing (Kosugi 2000) as the energies of Rydberg states are generally more accurately calculated than valence. Therefore, the 'shielding refined IVO' calculation, which will be described in §3.4, has been carried out. In 'shielding refined IVO' calculations, separate SCF calculations are sequentially carried out for each core-to-valence and/or Rydberg excited state (Kosugi 2000). For example, to optimize the first excited state, the doublet core ionized state of the molecule for a specified core hole is calculated by freezing the (N-1)-electron part and the core hole. The IP between the ground state and this optimized ionized state is then calculated. The core to the first excited state is then calculated based on the optimized doublet core ionized state. The second, third, etc. excited states are subsequently calculated by freezing the core hole and the previously optimized excited states.

Chapter 3 Results and Discussion

A well-ordered *n*-alkane sample with lateral molecular orientation is required for angular dependent NEXAFS measurements. Details of these requirements are presented in §3.1. A variety of substrates have been examined to find which substrate is suitable for the growth of *n*-alkane thin film with lateral orientation (§3.2.3). Lateral orientation was found only on a few substrates. These lateral-oriented molecules were along different directions of the substrate surface, forming contrasting domains in the NEXAFS images. The domain size was small. Larger domains are needed so that a series of NEXAFS spectra can be acquired from the same domain at different angles. Therefore, the next step was to increase the domain size in the laterally oriented *n*-alkane thin films (§3.2.4). At the same time, since the sample is radiation sensitive, the kinetics of radiation damage was studied (§3.2.1) to give guidance as to how large a domain is needed for a series of spectra without the occurrence of significant radiation damage artifacts. With the preparation of larger, laterally oriented *n*-alkane domains, the absolute angular dependent NEXAFS spectra of these domains were acquired. Curve-fitting methods were used to analyze the angular dependence of specific spectroscopic features (§3.2.6). The degree of linear polarization of X-rays affects the intensity of a transition, therefore, an evaluation of this effect and its magnitude was given in §3.2.5. The above results are consolidated in a published paper (§3.3).

Theoretical calculations have been carried out to study the LD for the NEXAFS features of *n*-alkanes, presented in §3.4 as a manuscript. In the process to increase the domain size of laterally oriented *n*-alkane thin films, it was found that the morphology and molecular orientation of *n*-alkane thin films were affected by the chain length and substrate temperature. These results are summarized in a paper draft, presented in §3.5. General conclusions and future work are presented in §3.6 and §3.7, respectively.

3.1 Molecular geometry requirements

To measure the angular dependent NEXAFS spectra and determine the direction of the TDM of C 1s $\rightarrow \sigma^*_{C\text{-}C}$ transition, well-ordered *n*-alkane samples are required; preferably single crystals in which all the alkane chains are aligned in a single direction. In order to obtain angular resolved NEXAFS spectra, we need to project the ***E*** vector directly along the alkane chain axis, perpendicular to the chain axis, and all angles in between.

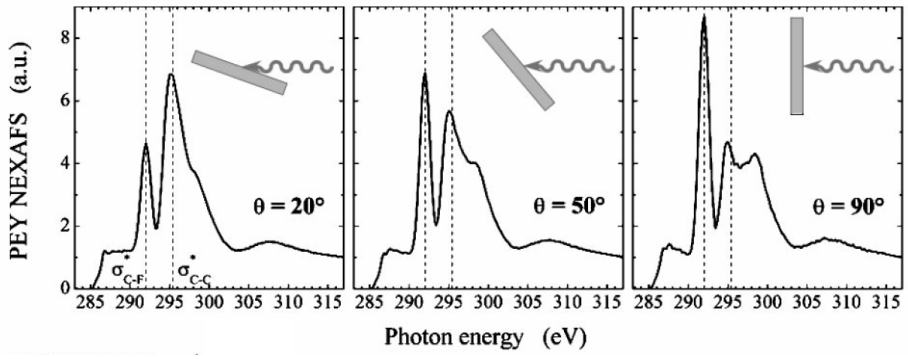

Figure 3.1 C 1s partial electron yield NEXAFS spectra from perfluorodecyltrichlorosilane SAMs collected at θ = 20°, 50°, and 90°, where θ is the angle between the sample normal and the ***E*** vector of the X-ray (Genzer et al. 2003)

In a typical angle resolved NEXAFS measurement of a surface adsorbed molecule, for example, in an electron yield measurement, a maximum range of 70° between the ***E*** vector and the alkane chain can be obtained between normal and glancing incidence (Kinzler et al. 1994; Genzer et al. 2003), as shown in Figure 3.1.

In transmission X-ray absorption geometry, it is possible to rotate the sample azimuthally over the entire 360 degree range. Different projections of the *n*-alkane molecular alignment and the ***E*** vector of X-rays are illustrated in Figure 3.2.

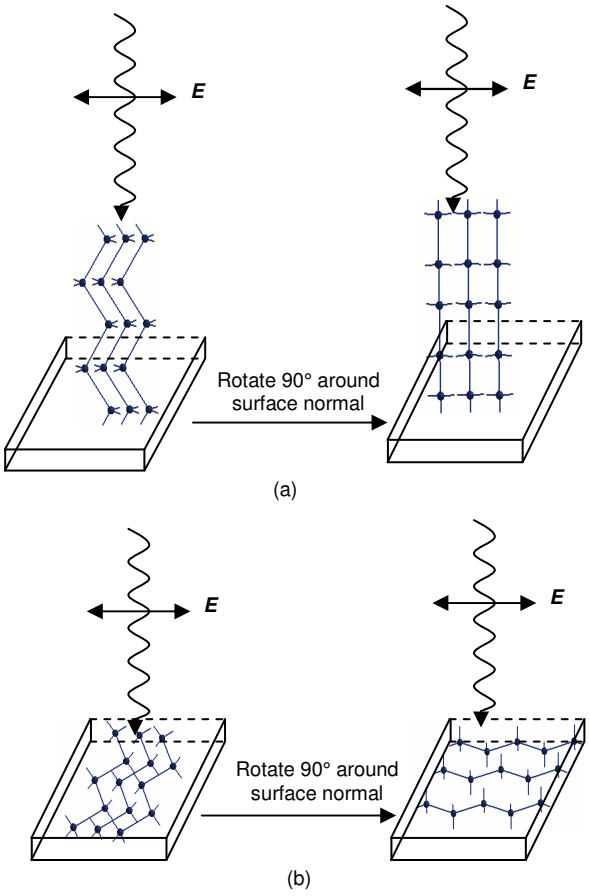

Figure 3.2 Schematic of alignment of *n*-alkane molecules relative to the substrate in a transmission measurement

When the X-rays are normally incident onto the sample surface (Figure 3.2(a)), which is the case for transmission measurements, the ***E*** vector is parallel to the sample

surface. If the *n*-alkane chains are oriented normal on the surface, then azimuthal rotation will not change the subtended angle between the ***E*** vector and macromolecular axis, i.e. the ***E*** vector is always perpendicular to the macromolecular axis. However, if the *n*-alkane chains are laterally oriented, i.e. parallel to the substrate surface, azimuthal rotation of the sample will change the subtended angle between the ***E*** vector and the alkane chain, from 90° to 0° as shown in Figure 3.2 (b). Consequently the intensity of NEXAFS resonances of *n*-alkane samples with lateral orientation will change with respect to the rotation angle.

Therefore, the desired molecular geometry in a transmission measurement is lateral orientation, i.e. the molecules lying along the substrate surface. Conventional thin film preparation involving LB and SAM processes often results in normal orientation or with tilt or disorder. This lateral orientation experimental geometry requirement creates some challenges for sample preparation. Epitaxial growth has been employed to prepare such samples.

3.2 NEXAFS spectroscopy of n-alkanes

Figure 3.3 shows a typical X-ray absorption spectrum of a HC sample that was deposited onto a cleaved NaCl (001) surface at room temperature in vacuum. Two sharp peaks are visible around 288 eV, below the C 1s IP. The IP position shown in this figure is estimated from that for the propane central carbon (Siegbahn et al. 1969). Above the IP there is a broad peak at ~292 eV and an even broader peak at ~302 eV. These peaks are assigned as C1s $\rightarrow \sigma^*_{C\text{-}C}$ transitions (Hitchcock and Ishii 1987; Stöhr, Outka et al. 1987). The assignment of NEXAFS features below the IP is controversial, as described in §1.5. The detailed assignments of these features will be given in the

calculation section below (§3.4). Nevertheless, we will use the conventional notation for each feature, i.e. C 1s $\rightarrow \sigma^*_{C\text{-}H}$ transitions at 287.6 eV and 288.2 eV, and C 1s $\rightarrow \sigma^*_{C\text{-}C}$ transitions at 293 eV and 302 eV (Stöhr, Outka et al. 1987).

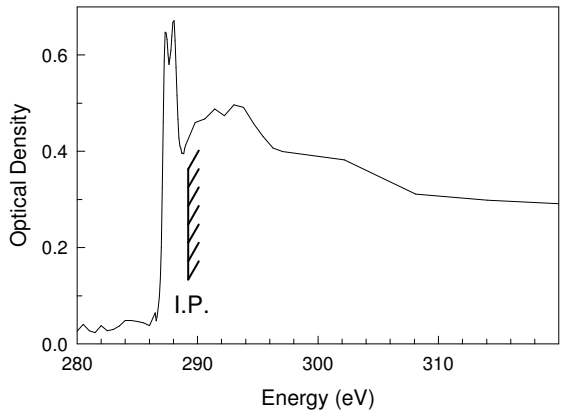

Figure 3.3 C 1s NEXAFS spectrum of HC sample

3.2.1 Radiation damage study

In NEXAFS spectroscopy of polymers, radiation damage (Rightor et al. 1997; Coffey et al. 2002) can be a significant concern. The nature of radiation damage is strongly dependent on the polymer being investigated (Zhang et al. 1995; Rightor et al. 1997). In *n*-alkane samples, we expect higher radiation sensitivity compared to aromatic molecules (Rightor et al. 1997). The manifestation of radiation damage to the *n*-alkane samples and the kinetic study of radiation damage will be presented below.

Manifestation of radiation damage to the *n*-alkane samples

Radiation damage to the *n*-alkane sample may have the following forms:

(1) Image contrast change: Figure 3.4(a) shows an X-ray absorption image of HC epitaxial growth on NaCl (001) surface after the inset square area was exposed to X-rays photon dose of 20 eV/nm^3. This image was taken at 287.6 eV. Outside the square area, dark and light domains can be differentiated by a clear boundary. Inside the

square area, no clear boundary between domains is observed. The square area becomes darker due to the radiation damage.

(2) Change in spectrum: The observation of new features in the NEXAFS spectrum, which can arise from the formation of C=C double bonds or cross-linking between adjacent chains, or loss of features as revealed in Figure 3.4(b). The dashed line represents the spectrum before radiation damage, in which the C 1s $\rightarrow \sigma^*_{C\text{-}H}$ transitions are dominant. A small sharp peak at 285.0 eV, corresponding to C 1s $\rightarrow \pi^*_{C=C}$ transition, indicates a little damage occurred in this scan. However, the overall shape of the spectrum is consistent with that of an undamaged sample. In the X-ray absorption spectrum obtained after the sample was damaged, the intensity of the sharp peak at 285.0 eV increased and the intensity of C 1s $\rightarrow \sigma^*_{C\text{-}H}$ transition (~288 eV) decreased. The overall shape of the spectrum differs greatly from that before radiation damage. The loss of intensity of the C 1s $\rightarrow \sigma^*_{C\text{-}H}$ transitions is accompanied by formation of C=C bonds.

The formation of C=C bond in the *n*-alkane molecules can be understood as follows: the X-ray radiation might cause the breakage of a C-H bond. If two adjacent C-H bonds are broken, a C=C bond will be formed. In the damaged NEXAFS spectrum, the intensity of the C 1s $\rightarrow \sigma^*_{C\text{-}H}$ transition decreased and the intensity of the C 1s $\rightarrow \pi^*_{C=C}$ transition increased, indicating that the number of C-H bonds decreased and that of C=C bonds increased. Therefore, the formation of C=C bonds is at the expense of C-H bond breakage in the *n*-alkane molecules.

(3) Mass loss: the observation of a decrease in intensity of the continuum is associated with mass loss. This can be caused by bond breaking, with smaller fractions leaving the sample, causing a decrease in intensity on the continuum of the NEXAFS spectrum.

(4) Reorientation: radiation dose might cause the reorientation of *n*-alkane chains. We have explored this in detail in §3.3.

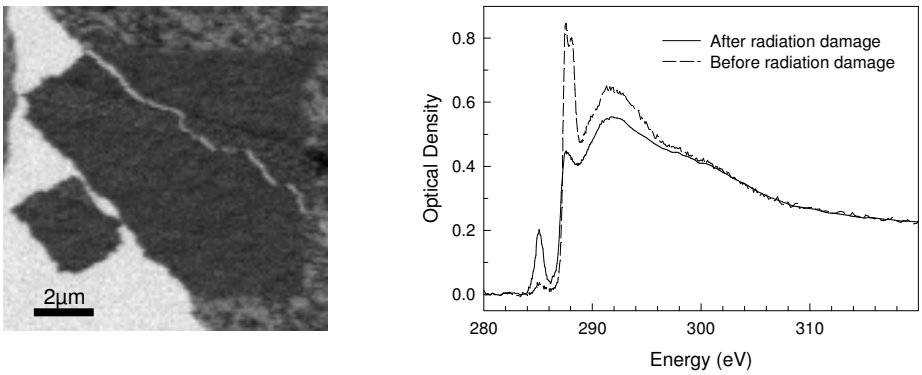

(a) (b)

Figure 3.4 (a) Visualization of radiation damage from X-ray absorption image. (b) Comparison of X-ray absorption spectra of n-alkane sample before (dashed line) and after (solid line) radiation damage

For our study, it is necessary to quantify the radiation damage kinetics of *n*-alkane molecules because a series of angular dependent C 1s X-ray absorption spectra are needed from the same sample. These must be acquired without significant radiation damage to the sample, which would distort these spectra.

Critical radiation dose (d_c)

Radiation damage usually causes a decrease in intensity of a feature. Sometimes it may cause formation of a new feature; therefore the intensity of the new feature will increase as seen in Figure 3.4 (b). Radiation damage is believed to be proportional to energy absorbed per unit volume. In order to quantify the damage rate, the spectral

optical density (*OD*) can be fitted to the following exponential expression (Coffey et al. 2002) :

$$OD = OD_{\infty} + C * \exp(-d / d_c) \quad (3.1)$$

where OD_{∞} is a constant representing the optical density remaining after infinite radiation dose, d is the radiation dose and d_c is the critical dose, which is a quantity that refers to the dose required for a 1/e attenuation of a particular spectroscopic feature lost by radiation (or the equivalent increase in a spectroscopic feature created by radiation damage).

Determination of d_c for each feature of *n*-alkane sample

To measure the kinetics of radiation damage, a small sample area (4 μm ×4 μm) was exposed to X-ray photons. The strategy here was to first introduce a large radiation dose to this area at one energy to deliberately damage the sample. And then the same sample area was imaged at other energies to monitor the spectral change after this exposure. To introduce a large radiation dose, the selected area was imaged at 340.0 eV, at which no specific NEXAFS absorption features occur and all carbon atoms in the sample will absorb X-rays equally. A large dwell time (10 ms) was used to accelerate radiation damage. The pixel spacing was set to match the spot size of the beam, ensuring even exposure. To monitor the spectral change after this exposure, the same sample area was imaged at energies at which big spectral change occurred upon radiation damage as indicated in Figure 3.4 (right). These energies were 285.0 eV, corresponding to the C 1s $\rightarrow \pi^*_{C=C}$ transition, and 288.1 eV, corresponding to the C 1s $\rightarrow \sigma^*_{C-H}$ transition. The dwell time for these images was much shorter (1 ms) to ensure that the radiation dose from these scans was minimal.

In order to quantify the radiation damage rate of each feature, the measured images were converted to optical density according to Eq. (1.5). The radiation dose of each image was calculated according to

$$d = \frac{E \times n_1 \times n_2}{V \times eff.} \tag{3.2}$$

where: d — radiation dose (eV/nm^3)

E — energy at which the sample was damaged (eV)

n_1 — number of photons absorbed per pixel (I_0-I)

n_2 — number of pixels

V — volume of the damaged sample

eff. — efficiency of the photomultiplier tube detector (assumed to be 20%) (Kilcoyne, Tyliszczak et al. 2003)

After obtaining the value of *OD* and radiation dose *d*, the *OD* was then plotted as a function of radiation dose *d* and fitted with the above Eq. (3.1). The fitted results are shown in Figure 3.5. The solid lines are exponential fits from which the critical doses for each transition were derived. The optical density of the C 1s $\rightarrow \sigma^*_{C\text{-}H}$ transition exhibits an exponential decay while the C 1s $\rightarrow \pi^*_{C=C}$ transition exponentially increases. The optical density of the C 1s $\rightarrow$ continuum exhibited a slight increase with radiation dose, probably caused by the photon deposition during these measurements.

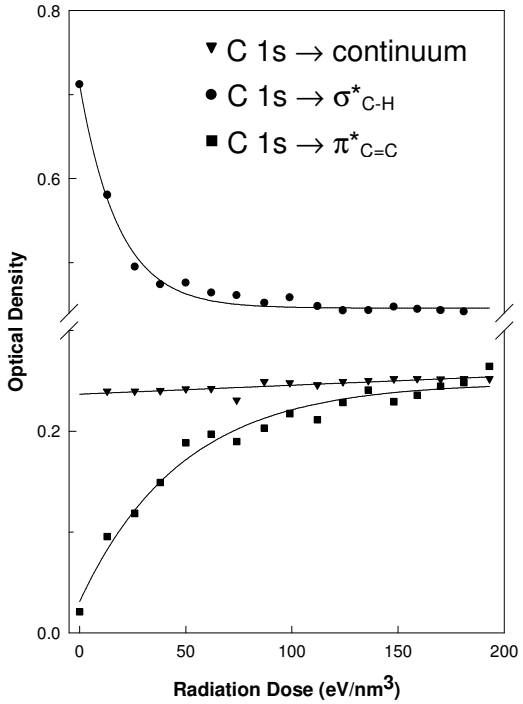

Figure 3.5 Dependence of OD of each feature on radiation dose of X-rays

Based on these calculations, the critical radiation dose (d_c) for the C 1s $\rightarrow$ $\pi^*_{C=C}$ and the C 1s $\rightarrow$ σ^*_{C-H} transitions was 48 eV/nm^3 (increase) and 18 eV/nm^3 (decrease), respectively. These results indicate that the C 1s $\rightarrow$ σ^*_{C-H} transition in *n*-alkane is the most radiation sensitive feature. In order to obtain a trustworthy NEXAFS spectrum, the accumulated radiation dose should be below the critical dose of the C 1s $\rightarrow$ σ^*_{C-H} transition, 18 eV/nm^3. Therefore, to obtain ten NEXAFS spectra from a 200 nm thick *n*-alkane sample without significant radiation damage, the sample has to be at least 13 μm $\times$13 μm large.

3.2.2 Measurement of molecular orientation and morphology

As introduced in §1.3, the molecular orientation can be derived from the NEXAFS spectroscopy. This section will focus on, from a microscopic scale, how to extract information regarding molecular orientation and thin film morphology from the NEXAFS spectroscopy and microscopy by using examples. These examples are selected from our own *n*-alkane thin films.

Molecular orientation - lateral

Figure 3.6(a) and (b) present X-ray microscopy images, recorded at 287.6 eV for (a) and 330.0 eV for (b), of an HC thin film (120 nm), epitaxially grown onto cleaved NaCl (001) where the substrate temperature (T_s) was kept at room temperature (RT) during deposition. Figure 3.6 (c) shows the extracted spectra from the dark and light domains present in Figure 3.6 (a).

Strong image contrast is observed in Figure 3.6(a), recorded at the energy of a C 1s $\rightarrow \sigma^*_{C\text{-}H}$ transition, while there is no contrast in Figure 3.6(b), recorded at an energy in the post-edge continuum. The origin of the X-ray absorption image contrast is shown by

$$I = I_0 \exp(-\mu \cdot \rho \cdot t) \tag{3.3}$$

where the meaning of each symbol is identical to those defined in Eq. (1.6).

The image contrast in Figure 3.6(a) may arise from either the presence of different chemical components or molecular orientation (reflected in the mass absorption coefficient μ) or from differences in sample thickness (t). Given the purity of the source material HC (98%) and the effect of distillation by evaporation in a vacuum chamber, the presence of other chemical species can be excluded.

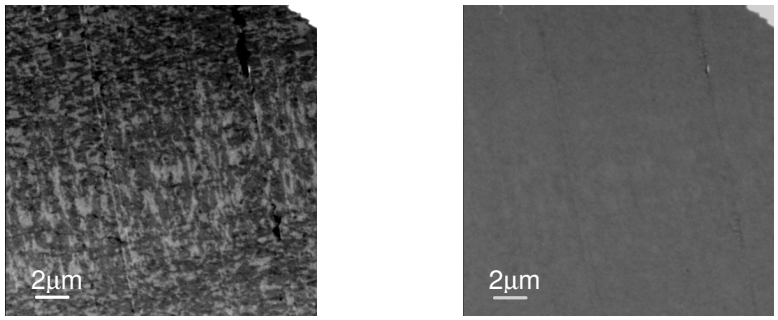

(a) (b)

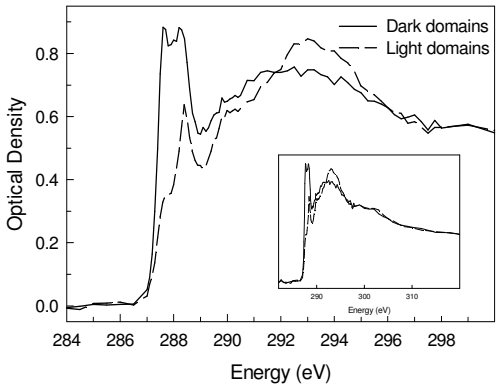

(c)

Figure 3.6 X-ray absorption images of a film of HC (epitaxially grown on air-cleaved NaCl) recorded at (a) 287.6 eV, (b) 330 eV, (c) NEXAFS spectra extracted from the light (dashed line) and dark (solid line) domains in HC image (a). The inset presents the full scale spectra.

Whether this image contrast is caused by molecular orientation or sample thickness variation can be clarified by recording an X-ray absorption image at energies where no spectroscopic features are present. For the *n*-alkane sample, there are no spectroscopic features above 315 eV and the mass absorption coefficient reflects the atomic photoionization cross section. Therefore, if the sample is uniform, i.e. no variation in sample thickness, the image recorded above 315 eV should not exhibit any image contrast. Otherwise if image contrast is observed above 315 eV, the sample is

not uniform, and therefore the contrast observed in the image at 287.6 eV is a result of sample thickness variation.

The fact that for this sample, no appreciable contrast can be observed in the image at 330 eV leads us to conclude that this sample is uniform. The uniformity of this sample can be also verified by the identical postedge of the two spectra extracted from the dark and light domains in Figure 3.6(a) because the optical density in the postedge is proportional to the sample thickness according to Eq. (1.6). Therefore, this sample is uniform and the image contrast in Figure 3.6(a) can be attributed entirely to *different molecular orientations* present in the thin film (i.e. the variation in μ with the molecular orientation). The intensity of the C 1s $\rightarrow \sigma^*_{C\text{-}H}$ transitions varies with the molecular orientation, indicating that this sample is well ordered with the HC molecules oriented, laterally, on the sample surface.

Molecular orientation - normal

Figure 3.7 shows the C 1s NEXAFS spectra of the HC sample, prepared on evaporated KCl thin films, before (solid line) and after (dashed line) the sample holder was rotated by 90°. The 'after rotation' spectrum has been offset for clarity. In the solid line spectrum, the C 1s $\rightarrow \sigma^*_{C\text{-}H}$ transitions are dominating, indicating that the ***E*** vector of X-rays is perpendicular to the macromolecular backbone, i.e. the ***E*** vector is along the C-H bonds. This might be caused by two situations: the molecules are laterally oriented on the substrate and the ***E*** vector happens to be along the C-H bonds; or the molecules are normally oriented on the substrate, in the transmission measurement, the ***E*** vector is always along the C-H bonds and the rotation of the sample will not change this dominance (cf. Figure 3.2 (a)). This can be verified by rotating the sample by 90°

around the surface normal. The corresponding NEXAFS spectrum after rotation was represented by the dashed line, in which the C 1s $\rightarrow \sigma^*_{C\text{-}H}$ transitions are still dominant. The C 1s $\rightarrow \sigma^*_{C\text{-}H}$ transitions exhibit maximum intensity in both spectra, indicating that the HC molecules are normal to the substrate surface.

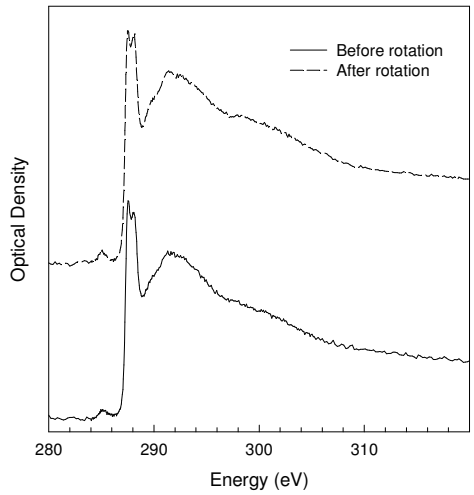

Figure 3.7 C 1s NEXAFS spectra of HC thin films, prepared on evaporated KCl thin films, before (solid line) and after (dashed line) the sample holder was rotated by 90°. The second trace is shifted for clarity.

Thin film morphology

As shown in Figure 3.6, the HC films deposited on cleaved NaCl (001) surface at room temperature are continuous and uniform, as revealed in the images and spectra. Figure 3.8 presents an X-ray microscopy image recorded at 287.6 eV of a HTC film (120 nm thick), deposited onto a cleaved NaCl (001) surface, which was maintained at room temperature during deposition (T_s = RT). In this figure, a combination of raft-like structures (vertical and horizontal bars, oriented 90^o to each other) and disk-like structures (round domains) is observed. Among the raft-like and disk-like structures, voids are visible. There are no HTC molecules in these void areas. NEXAFS spectra extracted from the raft-like and disk-like domains are presented in Figure 3.8 (right).

The spectrum extracted from a vertically-oriented bar shows maximum absorption at ~293 eV, corresponding to C 1s → $\sigma^*_{C\text{-}C}$ transition. The spectrum from a horizontally-oriented bar has maximum at ~288 eV (C 1s → $\sigma^*_{C\text{-}H}$ transition), indicating that the macromolecular axis of HTC molecules in each raft-element are parallel to the substrate surface, but oriented normal to the longitudinal direction of the element. Some defects (raft elements that are not orthogonally oriented) can be attributed to the flotation of the sample on H_2O as the NaCl substrate is removed.

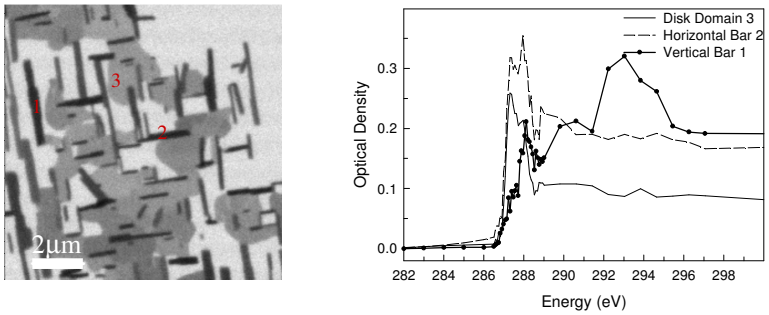

Figure 3.8 X-ray absorption images of a film of HTC (epitaxially grown on air-cleaved NaCl) recorded at 287.6 eV (left), and NEXAFS spectra (right) extracted from the contrasting domains in the HTC image

In addition to the raft elements, "disk-like structures" are observed between the raft elements. These disk-like structures are thinner than the raft-like structures as revealed in the spectra. The NEXAFS spectra show that HTC molecules in these domains are oriented normal to the substrate surface (solid line in Figure 3.8 (right)), which is different from those molecules in the raft-like structure. Therefore, in this HTC sample, lateral and normal orientations are present. The image contrast in the X-ray absorption image is caused by both the molecular orientation difference and sample thickness variation.

A comparison between Figure 3.6 and Figure 3.8 reveals that the morphology and molecular orientation of the HTC sample are quite different from the HC sample. NEXAFS spectroscopy and microscopy have exhibited their capability to provide information on molecular orientation and morphology of *n*-alkane thin films at the microscopic scale.

3.2.3 Substrate dependent *n*-alkane molecular orientation

As introduced in §1.6, *n*-alkane thin films can be grown on a variety of substrates. In order to obtain laterally oriented *n*-alkane thin films, different substrates were explored. The molecular orientation of thin films of *n*-alkane hexacontane (*n*-$C_{60}H_{122}$, HC) prepared on different substrates has been investigated by NEXAFS spectroscopy and microscopy. The results indicate that the molecular orientation of the *n*-alkane is strongly dependent on the substrates. This section only shows substrates on which the lateral molecular orientation of *n*-alkanes has been obtained. The other explored substrates are shown in §A1.

3.2.3.1 HC films prepared on solution-cast KHP substrate

The first substrate that was tried was solution-cast potassium hydrogen phthalate (KHP) crystals. This selection was based on a report that pentacontane and hexacontane molecules have been epitaxially grown on solution-cast KHP substrates (Zhang et al. 1989). These molecules are laterally oriented to the substrate surface along two directions. The angle between these two directions is about 70°, corresponding to the subtended angle between the two <110> directions of the KHP (001) surface.

Figure 3.9(a) shows an X-ray absorption image of HC prepared on solution-cast KHP substrate. This image was acquired at 287.6 eV. Contrasting banded structures were observed. Within each banded structure, small domains with contrast were visible. The C 1s NEXAFS spectra extracted from the dark and light domains are presented in Figure 3.9(b). These two spectra have the identical postedge optical density. The optical density of the C 1s $\rightarrow \sigma^*_{C\text{-}H}$ transitions and C 1s $\rightarrow \sigma^*_{C\text{-}C}$ transitions changed with contrast. These results indicate that the HC molecules were laterally oriented on the substrate surface, this sample had uniform thickness, and the image contrast observed in the image was due to molecular orientation. The domain size was visually estimated to be in the sub-micron scale.

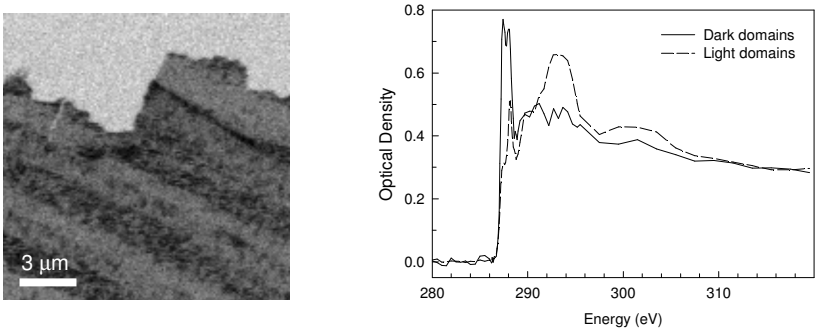

(a) (b)

Figure 3.9 (a) X-ray absorption image of HC sample prepared on solution-cast KHP. This image was taken at 287.6 eV. (b) NEXAFS spectra correspond to the dark (solid line) and light (dashed line) domains in image (a)

3.2.3.2 HC on cleaved NaCl (001) surface

Cleaved alkali halide surfaces have long been used as the substrate for the epitaxial growth of *n*-alkane thin films. These thin films have been studied experimentally (Koutsky et al. 1966; Walton et al. 1968; Wellinghoff et al. 1974; Ishida et al. 1993) and theoretically. Theoretical calculations (Mauritz et al. 1973; Mauritz et al. 1978) reveal the preferred orientation for *n*-alkane molecules is to lie on rows of the sodium

ions in the <110> directions where the permanent dipoles of the CH_2 units are perpendicular to the substrate surface (001) face. Figure 3.10(a) shows the orthorhombic subcell structure of paraffin (Balta Calleja 1965). The subcell parameters for paraffin are $a_s = 7.58$ Å, $b_s = 4.94$ Å and $c_s = 2.54$ Å, (s denotes subcell). Each unit contains two paraffin molecules. Figure 3.10(b) shows the epitaxial growth of paraffin on cleaved NaCl (001) face (Willems 1958). The contact plane is the (010) plane of PE parallel to the (001) face of NaCl with the macromolecular axis of PE (*c*-axis) is along the crystallographically equivalent <110> directions of NaCl (Wittmann et al. 1983).

Therefore, cleaved NaCl (001) surface was the second substrate we have tried for the epitaxial growth of HC samples.

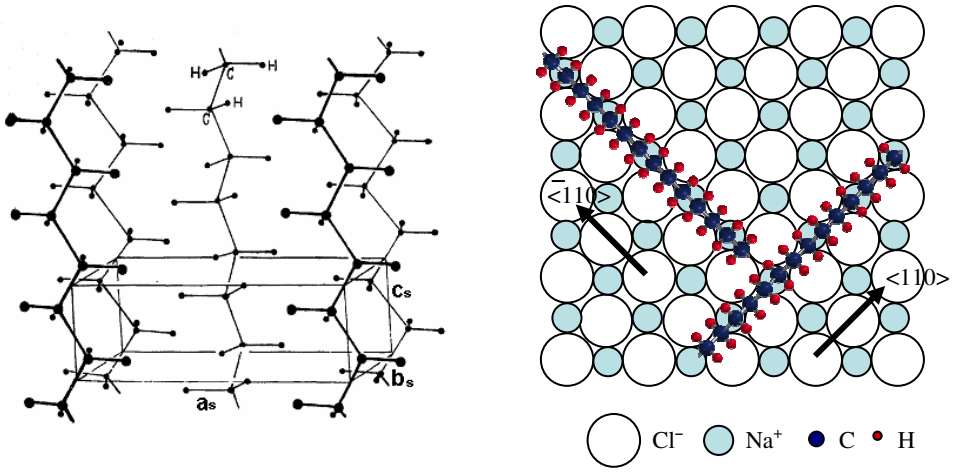

(a) (b)

Figure 3.10 (a) Orthorhombic subcell structure of paraffin. ($a_s = 7.58$ Å, $b_s = 4.94$ Å and $c_s = 2.54$ Å) (b) Epitaxial growth of paraffin on NaCl (001) face

The X-ray absorption images and NEXAFS spectra of this HC sample were shown in Figure 3.6, above. The detailed analysis shown in §3.2.2 indicated that the HC molecules on cleaved NaCl (001) surface were laterally oriented on the NaCl surface, this sample had uniform thickness, and the image contrast observed in the image was

due to molecular orientation. The domain size was visually estimated be in the tens of nanometer.

3.2.3.3 HC on evaporated terephthalic acid (TA)

TA has never been reported as the substrates for growth of *n*-alkanes thin films. We selected TA because of its structure similarity to benzoic acid (BA), containing a benzene ring and the COOH group. Unlike comelting of BA, TA was a successful substrate for inducing lateral orientation of *n*-alkane molecules. The TA substrate was prepared in vacuum. Figure 3.11 shows an X-ray absorption image of HC films formed on evaporated TA substrates and the NEXAFS spectra extracted from the dark and light domains. The image contrast in the left image and the different OD of C 1s $\rightarrow$ $\sigma^*_{C\text{-}H}$ (~288 eV) and C 1s $\rightarrow$ $\sigma^*_{C\text{-}C}$ transitions (~ 293 eV) in these two spectra indicated the HC molecules were laterally oriented on TA substrate.

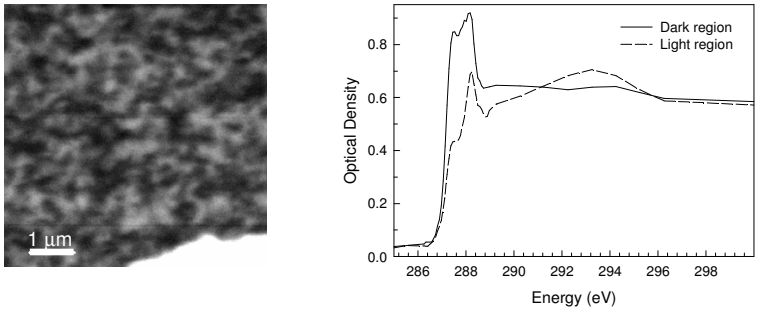

Figure 3.11 X-ray absorption image (left) of HC films formed on evaporated TA substrates and NEXAFS spectra (right) extracted from the dark and light domains

In addition to the above substrates, we have tried other organic and inorganic substrates. These substrates were: solution-cast *p*-bromo benzoic acid (*p*-BBA), evaporated *p*-phenyl benzoic acid (*p*-PBA) thin film, evaporated KCl thin film and Si_3N_4 membrane windows. The results of HC thin films formed on these substrates are

presented in §A1. Briefly, the X-ray absorption spectroscopy and microscopy showed that HC molecules were normally oriented on the substrate surface when prepared on a solution-cast *p*-BBA substrate, on Si_3N_4 membrane windows and on an evaporated KCl thin film. The HC thin film did not have a uniform thickness when prepared on an evaporated *p*-PBA thin film.

The different molecular orientation of HC observed on the above various substrates can be understood in terms of the different molecule-substrate interactions. The molecule-molecule interaction strength is nearly the same for lateral and normal orientation for a multilayer sample. If the molecule-substrate interaction is stronger than the molecule-molecule interaction, then the HC molecules tend to lie along the substrate surface. If the molecule-substrate interaction is weak, then normal orientation tends to occur.

For the same molecules, the strength of the molecule-substrate interaction depends on the properties of the substrate. The cleaved NaCl (001) surfaces and solution-cast KHP surfaces are ionic crystalline substrates, which exhibit a long range surface order. In addition to the van der Waals interactions, there are additional ionic interaction and induced dipole interactions. Therefore, the HC molecules are oriented laterally on such substrate surfaces. For the TA substrate, the observation of lateral orientation of HC leads us to conclude that there is strong interaction between HC molecule and TA surface. However, it is not clear what causes such strong interaction.

Summary on substrate dependency of molecular orientation

Based on the above results, the HC molecules assume normal orientation when prepared on bare Si_3N_4 membrane windows, evaporated *p*-BBA thin films, evaporated

KCl thin films, and melted BA thin films. While on cleaved NaCl (001) surface, solution-cast KHP, and evaporated TA thin films, the lateral orientation of HC molecules were achieved. However, the domain size of the lateral orientation of HC thin films is so small, in the range of tens nanometers. Multi-spectra can not be taken for this kind of samples because it is hard to track the position when rotating the sample and radiation damage will not allow it. Therefore, the next step is to increase the single orientation domain size.

Strategies to increase domain size

Several strategies including improvement of the substrate preparation, annealing of the thin films, and preparing thin films at elevated substrate temperatures, have been employed to increase the size of laterally oriented domains in the HC thin films.

It is expected that larger substrate crystal surface will favor the formation of larger domains of deposits. For KHP substrates, larger KHP crystals can be obtained when chelating with ethylenediaminetetraacetic acid, which can be cleaved just like NaCl single crystal (Srinivasan et al. 1999). This has been used as a substrate for HC deposition. The X-ray absorption microscopy and microscopy (data shown in §A2) shows that the HC sample prepared on such substrates contained small contrasting domains in which the HC molecules are laterally oriented on the substrate along different directions. Therefore, the domain size of HC crystals did not improve on such substrates.

Rapid thermal annealing after the film formation (Torsi et al. 1995) and preparing the thin film at an elevated substrate temperature (Bouchoms et al. 1999) are the two methods usually employed to improve the size of the crystallites. The former involves

rapidly increasing the temperature above the melting point, leaving the sample at this high temperature for a few seconds, and then slowly cooling down to allow recrystallization. This method has been successfully used for α-hexathienylene thin films to improve the size of the crystallites to tens of microns (Torsi et al. 1995; Lovinger et al. 1996). The second method has been applied to the pentacene molecules on SiO_2 substrates (Bouchoms et al. 1999). Maximum single crystal size of ~15 μm is found when the pentacene molecules are deposited at a substrate temperature of 80°C. Here, we prepared the thin HC films on cleaved NaCl (001) surface and TA thin film substrates in a vacuum chamber at elevated substrate temperatures in order to increase the domain size.

For TA thin film substrates, the HC molecules were deposited on it at different substrate temperature of 36°C and 54°C. The X-ray absorption spectroscopy and microscopy results (data shown in §A3) show that the HC sample prepared on TA substrates at different substrate temperature contained small domains with contrast and the HC molecules in each domain with contrast are laterally oriented on the substrate along different directions. Therefore, the domain size of HC crystals did not improve on TA substrates at different substrate temperature.

For NaCl substrates, the HC molecules were deposited at different substrate temperatures. It is found that the average domain size of HC crystals prepared on such substrates increased at higher substrate temperature. The details are given in §3.2.4 and §3.5.

3.2.4 Dependency of domain size on substrate temperature (T_s)

This section presents the results for the largest domain size we have obtained for this sample. Figure 3.12 (a) presents an X-ray microscopy image recorded at 287.6 eV of an HC thin film evaporated onto freshly cleaved NaCl, where the substrate temperature was held at 45°C during evaporation. The contrast in this sample is much more uniform, consisting of an open area (white) where no sample is present, a matrix, and some dispersed domains. The contrast inverts when the sample is rotated by ~70° (Figure 3.12 (b)) about the photon axis (NB bending magnet image, x-ray electric field vector is horizontal). The dark lines observed in Figure 3.12 (b) are most likely due to the sample reorientation caused by the small radiation dose incurred when taking defocused spectra along these lines. The radiation damage threshold for chemical change is much higher than that for reorientation (see §3.3 and §3.2.1). From this polarization contrast and inversion, we see that the sample consists of a major phase aligned in one direction and a number of minor phases, aligned at right angles to the major phase. This is further developed through spectroscopy of the major phase, below.

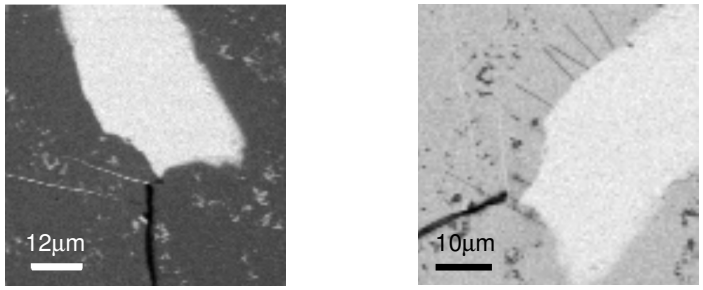

(a) (b)

Figure 3.12 NEXAFS images of HC epitaxially grown onto cleaved NaCl (001) surface in vacuum with T_s = 45°C. Images were taken at 287.6 eV with the sample rotated 70°

The increase in the domain size when the sample is deposited at 45°C relative to the sample deposited at room temperature suggests that some energy is required to overcome the diffusion energy barrier E_a to grow larger crystals as indicated in Eq. (1.22). For the sample prepared at room temperature, the molecular movement on the substrate is limited as there is less thermal energy to overcome the E_a. This will be explored in §3.5.

The sample deposited at a substrate temperature of 45°C has larger domains, which we use for our angle-resolved NEXAFS measurements. The substrate temperature effects on molecular orientation and domains size will be investigated in detail in §3.5.

3.2.5 Comparison of NEXAFS spectra from bending magnet and EPU

Angle-resolved NEXAFS spectra can be measured by using a bending magnet and an EPU source. A difference between these two X-ray sources is the degree of linear polarization, which has been shown to affect the intensity of a NEXAFS resonance (Stöhr 1992). In the bending magnet measurements, the ***E*** vector of X-rays is elliptical in the horizontal plane. The degree of linear polarization is estimated to be 85~90% (Margaritondo 1988; Stöhr 1992). A recent measurement indicates the degree of linear polarization is 67% in the 5.3.2 STXM at ALS (Watts et al. 2006). In the EPU measurements, the degree of linear polarization has been measured to be 100% +0/-1% (Kortright 2005). The polarization of X-rays for this polarization can be changed from horizontal (EPU = 0°) to vertical (EPU = 90°) (Young et al. 2002). Figure 3.13 compares the NEXAFS spectra of an HC sample obtained by using a bending magnet and an EPU source. These spectra were acquired with the ***E*** vector oriented along the

macromolecular backbone, i.e. θ = 0°. The HC sample was prepared on cleaved NaCl (001) surface at T_s = 45°C.

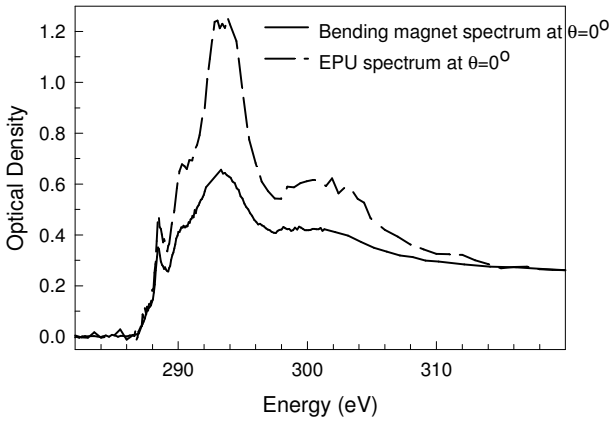

Figure 3.13 Comparison of spectra obtained from bending magnet and EPU

Large systematic differences were observed between the Carbon 1s spectra recorded using the bending magnet STXM (BL 5.3.2) and the EPU sourced MES-STXM (BL 11.0.2) microscope, as presented in Figure 3.13. In particular, the intensities of all strong transitions are attenuated in the bending magnet spectrum. There are two pertinent origins for spectroscopic distortion: photon ellipticity and higher harmonic photon contamination. The degree of polarization of X-rays produced from EPU is believed to be 100% and 85~90% from bending magnet. The increased ellipticity of a bending magnet source is expected to decrease the magnitude of the linear dichroism. However, ellipticity is not the likely origin of all of these differences. In this geometry, increased photon ellipticity would decrease the intensity of the 293.5 eV C 1s $\rightarrow \sigma^*_{C\text{-}C}$ transition but increase the intensity of the pre-edge C 1s $\rightarrow \sigma^*_{C\text{-}H}$ transition. However, all strong spectroscopic features are attenuated in the bending magnet spectra shown in Figure 3.13.

Higher harmonic contamination is a particular concern for the bending magnet STXM, which uses a spherical grating monochromator (SGM). The SGM monochromator is known to produce significant 2^{nd} and 3^{rd} order harmonics. In contrast, the plane grating monochromator on the MES-STXM beamline does not produce higher harmonics as efficiently. As higher harmonics will not be absorbed by the sample with the same efficiency as the first harmonic photons, both the I and I_o signals in Eq. (1.5) will be artificially higher than for a pure 1^{st} order radiation source, and the magnitude of the optical densities will be suppressed. In the STXM microscope, the order sorting aperture (Figure 2.3) should filter out most of the higher harmonic photons, which will be diffracted into the 2^{nd} order focus, but small misalignments can also lead to higher harmonic pollution. Higher harmonics can also be transmitted directly through the central stop of the zone plate if this component is not thick enough. Because of the distortion of the bending magnet NEXAFS spectra due to 2^{nd} order photon flux and the photon ellipticity, the EPU data will only be used for the subsequent analysis of the absolute angle dependence of HC.

3.2.6 Analysis of angle resolved NEXAFS spectra — curve fitting

A curve fitting technique was employed to quantitatively analyze the angular dependence of each resonance in the NEXAFS spectrum of *n*-alkanes. From the angular dependence of each transition, the direction of the TDM of the C 1s $\rightarrow \sigma^*_{C\text{-}C}$ transition, as well as that for the other transitions, can then be determined.

Several methods are used to analyze the angle resolved NEXAFS spectra of *n*-alkanes. The conventional method is the difference spectrum method (Outka et al. 1987; Outka et al. 1988; Stöhr 1992). This method produces a resonant background and

only three well-separated resonances (C 1s $\rightarrow \sigma^*_{C\text{-}H}$, C 1s $\rightarrow \sigma^*_{C\text{-}C}$, and C 1s $\rightarrow \sigma^*_{C\text{-}C'}$) of an alkane spectrum have been recognized (Outka et al. 1988); (Kinzler et al. 1994) as shown in Figure 3.14..

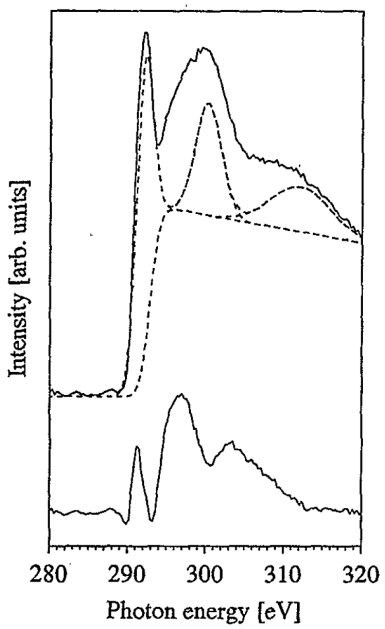

Figure 3.14 Curve fitting of the C 1s NEXAFS spectrum of three layers of Ca arachidate recorded at a photon incidence angle of 50°. (Lower part) background (residuum) used in the fitting process (Kinzler et al. 1994)

However, a high resolution NEXAFS spectrum of hexatriacontane (n-$C_{36}H_{74}$) clearly reveals two peaks in the C 1s $\rightarrow \sigma^*_{C\text{-}H}$ resonance (Ohta et al. 1990). These two peaks are separated by only 0.6 eV. Such strongly overlapped features exclude directly using this difference spectrum method to analyze these resonances as the magnitude of the overlapping peaks in the difference spectra partially cancel each other. Therefore, deconvolution of these resonances via peak fitting for the raw angular-resolved NEXAFS spectra has been employed to obtain the alkyl chain tilt angle of hexadecanethiol on Au (111) substrate (Willey et al. 2004) and chain orientation of hexane multilayer on n-alkanethiolate ($C_6H_{13}S$) monolayer (Kondoh et al. 2001). In our

high resolution NEXAFS spectra of HC samples, even more resonances are visible and these resonances are strongly overlapped, sometimes, with opposite polarization dependence. Therefore, the regularly used difference spectrum method is not suitable for such complicated spectra.

In this thesis, deconvolution of the resonances in the NEXAFS spectra of the *n*-alkane sample was accomplished by *simultaneously* fitting spectra acquired at a series of different subtended angles between the ***E*** vector and HC macromolecular backbone.

These angular dependent NEXAFS spectra were obtained on the MES-STXM microscope. In order to match the EPU = 0° to θ = 0°, i.e. at EPU =0°, the ***E*** vector is oriented along the macromolecular backbone of the *n*-alkanes; the sample was rotated around the surface normal. The NEXAFS spectrum at EPU = 0° was taken after each rotation. When the intensity of the resonance at 293.5 eV reached a maximum, that sample position is the position at which the ***E*** vector is oriented along the macromolecular backbone of the *n*-alkanes, i.e. θ = 0°. And then the sample was kept in that position, the polarization of EPU was changed from 0° to 90° at 10° increment, corresponding to θ = 0°, 10°, …, 90°.

These raw NEXAFS spectra were fitted by using the MGAUSS program (Tyliszczak 1995). This program allows the *simultaneous* fitting of multiple spectra to a common set of parameters, with the capability of constraining specific parameters across the entire dataset. For a series of NEXAFS spectra acquired for one molecule at different angles, we expect the *intensities* of specific peaks to vary, but their position and width will be invariant. Therefore, we constrained our fit so that the energy and the width of each feature would vary identically in the fits of all spectra but the intensity of

this feature could vary independently. To achieve the best fit of the 10 spectra recorded with different subtended angles θ, 8 Gaussian curves corresponding to the spectral features, (the number of Gaussian peaks was determined by observing all angle-dependence spectra), an error step function corresponding to the ionization edge of carbon (fixed at 289.7 eV, 1.0 eV lower than the ionization potential of propane in the gas phase), and an orientation independent background were used. The parameters for the positions and shapes of the various NEXAFS resonances with angular dependent intensity are listed in Table 3.1.

Table 3.1: Parameters used in MGAUSS fit.

Peak position (eV)	287.63	288.23	288.51	289.1	291.5	293.5	296	301
FWHM(eV)	0.51	0.68	0.54	2.3	1.3	3.6	6	8

Figure 3.15 shows the curve fitting results of the angular dependence of the NEXAFS spectra of HC films prepared at T_s = 45°C, obtained at 11.0.2 STXM of EPU, at 10 subtended angles between the ***E*** vector and HC alkyl backbone, θ = 0°, 10°, 20°, 30°, 40°, 50°, 60°, 70°, 80°, and 90°.

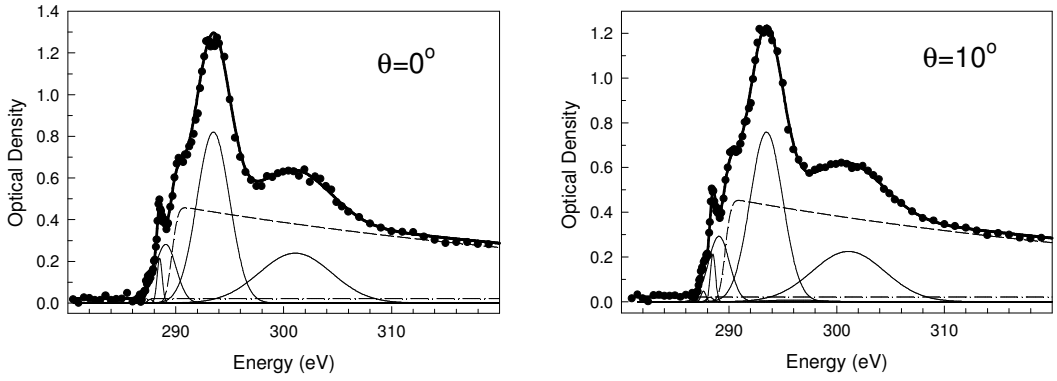

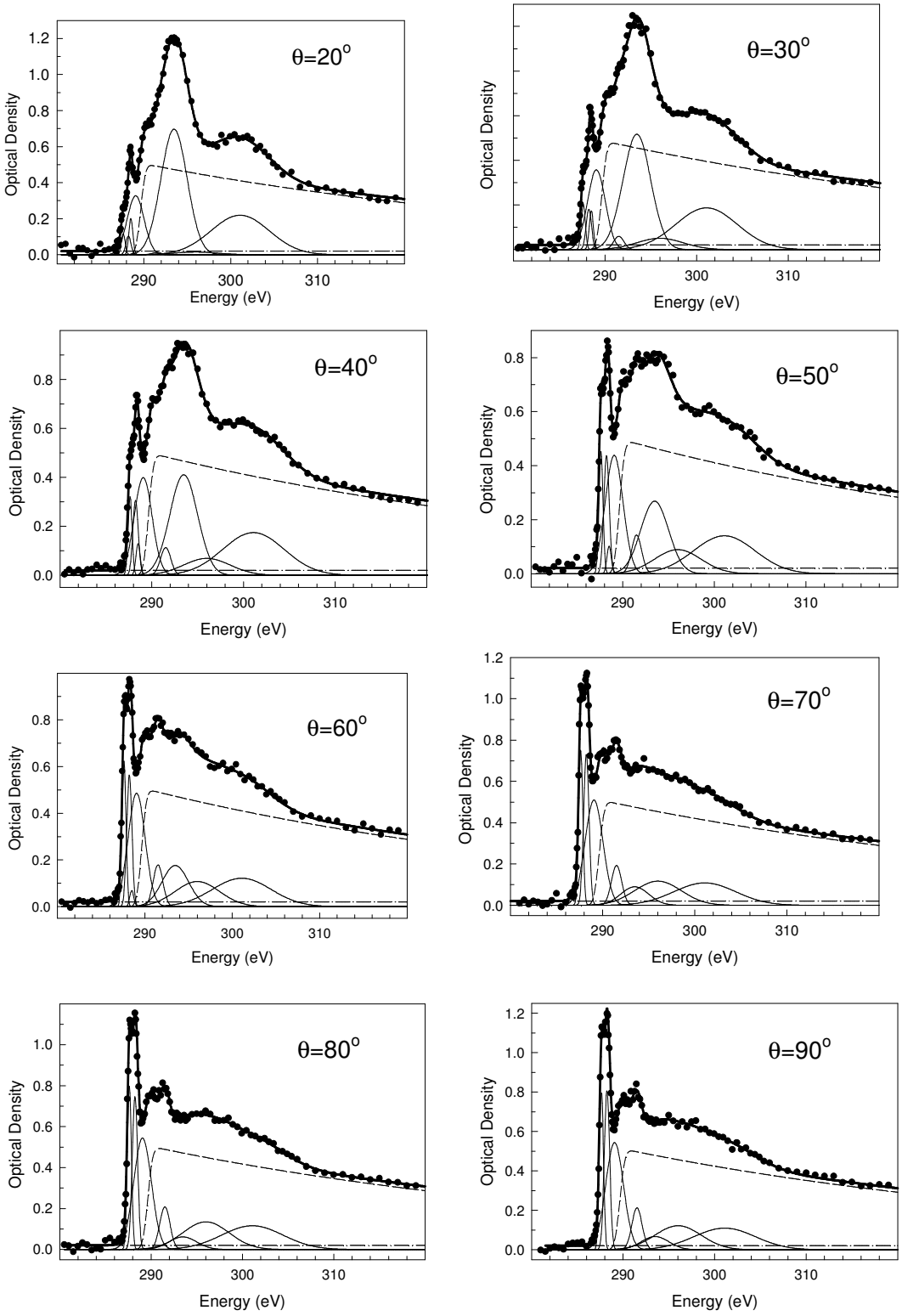

Figure 3.15 Fits of the C 1s NEXAFS spectra of HC thin films at different angles from 0° to 90° in 10° increments

The dotted line represents the experimentally measured spectra; the thick solid line is the best-fit spectra from MGAUSS; thin solid lines are the Gaussian peaks; the dashed line the error step function, representing the atomic photoionization cross section below and above the absorption edge, and the dash-dot line the background. The intensity of the C 1s $\rightarrow \sigma^*_{C\text{-}H}$ transition and the C 1s $\rightarrow \sigma^*_{C\text{-}C}$ transition varied with the subtended angle θ between the electric field vector and the HC alkyl backbone, indicating that this sample is well oriented. The detailed analysis of the angle-resolved C 1s NEXAFS spectra was given in §3.3.

3.3 Linear dichroism in the X-ray absorption spectra of n-alkanes

This section documents the linear dichroism in the NEXAFS spectra of an HC samples prepared on cleaved NaCl (001) surfaces. The detailed analysis of the angular resolved NEXAFS spectra of the HC samples is given. The results show that the transition dipole moment associated with the C 1s $\rightarrow \sigma^*_{C\text{-}C}$ transition is oriented along the macromolecular chain axis, contradicting the predictions of the building block model. Four features are revealed below the C 1s IP of *n*-alkanes. The intensity of the first two features exhibits an opposite angular dependence compared to that for the C 1s $\rightarrow \sigma^*_{C\text{-}C}$ transition, while the third feature exhibits the same angular dependence as the C 1s $\rightarrow \sigma^*_{C\text{-}C}$ transition. This work has been published in *Journal of Physical Chemistry A*, 2005, 109(51), 11724-11732. This work is presented here in its as-accepted form.

The author of this thesis developed the sample preparation methods, prepared the samples, acquired the NEXAFS spectra, and fit the angular-resolved NEXAFS spectra. In close collaboration with Dr. Urquhart, this work was published.

The author of this thesis obtained Dr. Urquhart's agreement to present the work in this thesis.

Linear Dichroism in the X-ray Absorption Spectra of Linear n-alkanes

Juxia Fu and Stephen G. Urquhart *

Department of Chemistry, University of Saskatchewan, 110 Science Pl, Saskatoon, Saskatchewan, Canada S7N 5C9

The nature of the linear dichroism in the Near Edge X-ray Absorption Fine Structure (NEXAFS) spectra of linear n-alkanes is a matter of long standing controversy. Linear dichroism in the Carbon 1s $\rightarrow \sigma^*_{C\text{-}C}$ transition has been interpreted within a building-block model and a molecular orbital model, leading to two different descriptions for the angular dependence of this feature. When used for measurement of molecular orientation, the application of these two different models will lead to different results. We have explored the linear dichroism in the Carbon 1s NEXAFS spectra of single crystals of the linear n-alkane hexacontane (n-$C_{60}H_{122}$). An analysis of the angular dependence in this spectrum shows that the transition dipole moment associated with Carbon 1s $\rightarrow \sigma^*_{C\text{-}C}$ transition is oriented along the macromolecular chain axis, contradicting the predictions of the building block model. However, other transitions are observed in the $\sigma^*_{C\text{-}H}$ and the $\sigma^*_{C\text{-}C}$ bands that are orthogonal to the dominant transitions for each band. We also observe that radiation damage can be manifest in the form of molecular reorientation in highly ordered organic thin films.

Corresponding author: email stephen.urquhart@usask.ca

Submitted June 6, 2005 to JPCB, Accepted October 25, 2005

Introduction

Linear dichroism (LD)[1-3] is the anisotropic absorption of linearly polarized electromagnetic radiation (EMR). LD spectroscopy is widely used to measure the orientation of biomaterials such as DNA,[4] proteins, polypeptides,[5] molecules adsorbed on surfaces,[6] self-assembled monolayers (SAMs),[7] Langmuir-Blodgett films,[8] rubbed polymers,[9] etc. Linear dichroism studies have been carried out by a wide variety of spectroscopic techniques, including surface enhanced Raman spectroscopy (SERS),[10] attenuated total reflectance (ATR) spectroscopy,[11] infrared reflection absorption spectroscopy (IRRAS),[12] polarization modulation IRRAS spectroscopy,[12] near-edge X-ray absorption fine structure (NEXAFS) spectroscopy[6,13] and NEXAFS spectromicroscopy.[13]

NEXAFS spectroscopy[6] is an ideal technique for probing the molecular orientation of organic materials because sharp core level excitations for carbon, nitrogen, oxygen and fluorine occur in the soft X-ray region. Features in NEXAFS spectra are typically described in terms of one electron transitions from core levels to unoccupied valence orbitals of π^* and σ^* symmetry, as well as Rydberg orbitals. These spectroscopic features can be used to identify the chemical composition of materials[14-16] and their angle dependence can be used to measure the orientation of specific chemical moieties.[6,17-20]

The intensity of the NEXAFS resonances depends on the angle θ between the electric field vector of X-rays (E) and the direction of transition dipole moment (TDM, μ_{if}) according to:

$$I \propto \left| E \bullet \mu_{if} \right|^2 \propto \cos^2 \theta \qquad (1)$$

where μ_{if} is the TDM for the one electron transition from the initial state ψ_i to the final state ψ_f according to:

$$\mu_{if} = \left\langle \psi_f \middle| \mu \middle| \psi_i \right\rangle \qquad (2)$$

For example, for a 1s $\rightarrow$ π^* transition, the TDM is perpendicular to the nodal plane of the π-bond. The transition intensity varies as $I = A\cos^2\theta$, where A describes the angle-integrated cross section and θ is as defined above.

In unsaturated molecules, the symmetry of the π^* orbital creates an unambiguous relationship between the molecular frame and the TDM for the core $\rightarrow$ π^* transition. Examples of the use of core $\rightarrow$ π^* transitions for measurement of molecular orientation include polymer surfaces such as polyimides[9] and polystyrene[21] as well as many small molecules adsorbed on single crystal surfaces.[6]

In saturated molecules such as n-alkanes, the character of the 1s $\rightarrow$ σ^* transitions is controversial. As a starting point, there is a long standing, perhaps never-ending controversy regarding the assignment of continuum features as σ^* shape resonances. There is specific disagreement regarding the assignment of Carbon 1s $\rightarrow$ $\sigma^*_{C\text{-}C}$ transitions in simple hydrocarbons such as ethane.[22] If, for the sake of discussion, we accept that continuum resonances in the Carbon 1s NEXAFS spectra of n-alkanes can be considered as Carbon 1s $\rightarrow$ $\sigma^*_{C\text{-}C}$ transitions, our next step is to consider their character. Unlike unsaturated molecules, the TDM vector for Carbon 1s $\rightarrow$ $\sigma^*_{C\text{-}C}$ transitions cannot easily be projected onto the molecular frame. There are two common models for the $\sigma^*_{C\text{-}C}$ excited state: a building block (BB) model and a molecular orbital (MO) model. These models and the consequences of their selection will be discussed in

detail below. Even if the continuum features observed in the NEXAFS spectra of n-alkanes cannot be properly assigned as Carbon 1s $\rightarrow \sigma^*_{C\text{-}C}$ transitions, measurement of their angle dependence still remains relevant as these spectroscopic features continue to be for measurements of molecular orientation, despite the ambiguity in their theoretical justification.

In the building block (BB) model proposed by Outka, Stöhr and co-workers,[23] a molecule is viewed as an assembly of diatomic subunits or "building blocks". Linear alkanes are treated as the assembly of individual C-C "building blocks", and the angle dependence of the Carbon 1s $\rightarrow \sigma^*_{C\text{-}C}$ transition arises from the sum of the TDM's of the individual C-C building blocks, each TDM aligned along each C-C bond. Since this model implicitly considers the electronic structure as the sum of the properties of *specific bonds between diatomic pairs*, this is in essence a *valence bond* description. In contrast to this BB model, Hähner *et al.*[7] have used a molecular orbital (MO) approach to consider the angle dependence of the C 1s NEXAFS spectra of n-alkanes. A molecular orbital can be delocalized over all or part of a molecule and not (necessarily) localized to a specific bond pair. Intuitively, we expect the $\sigma^*_{C\text{-}C}$ molecular orbital will be delocalized and aligned along the macromolecular axis of the n-alkane chain, rather than oriented along specific C-C bonds. As a consequence, the TDM of the Carbon 1s $\rightarrow \sigma^*_{C\text{-}C}$ transition should be aligned along the macromolecular axis in the MO model. The predicted angle dependence for the Carbon 1s $\rightarrow \sigma^*_{C\text{-}C}$ transition in the NEXAFS spectrum of a linear n-alkane molecule based on the BB and the MO model is presented in Figure 1. This angle dependence is expressed as a function of the angle between the electric field vector (E) and the macromolecular chain axis of the n-alkane.

The BB model is constructed by adding up the bond specific contributions where the TDM is aligned along individual C-C bonds and the sum is derived using appropriate C-C-C bond angles.[24] The MO model assumes that the TDM is directed along the chain axis as a delocalized $\sigma^*_{C\text{-}C}$ molecular orbital.[7]

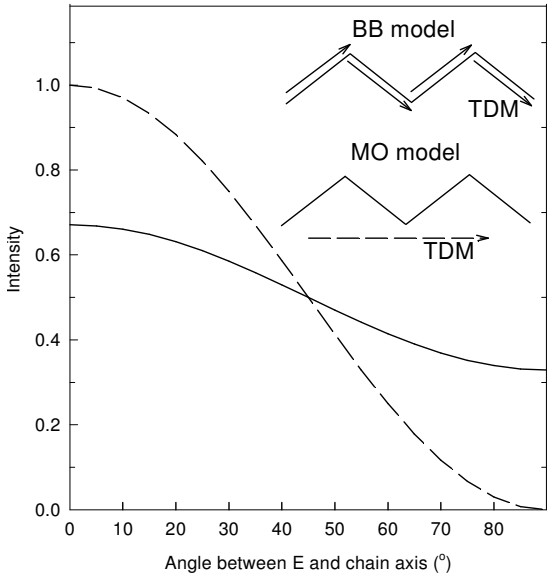

Figure 1 Relationship between the transition intensity and the angle between the transition dipole moment (TDM) and the electric field vector (E) for the Carbon 1s NEXAFS spectra of linear alkanes, calculated within the building block (BB; solid line) and the molecular orbital (MO; dashed line) models. The intensity scale is defined according to $I = A\cos^2\theta$, where A describes the angle-integrated cross section (A = 1 in this figure).

Both models show that the intensity of the Carbon 1s $\rightarrow \sigma^*_{C\text{-}C}$ transition is at a maximum when the electric field vector is directed along the chain axis ($\theta = 0°$) and reaches a minimum when the electric field vector is perpendicular to the chain axis ($\theta = 90°$). The key difference between these models is the magnitude of the change. In the MO model, the intensity of the Carbon 1s $\rightarrow \sigma^*_{C\text{-}C}$ transition is predicted to go to zero at $\theta = 90$ while this transition never goes to zero intensity in the BB model. The

difference between models can be understood by considering the $\cos^2\theta$ dependence for bond-specific contributions in the BB model. The MO and BB models are, of course, idealizations. This fact provides all the more reason why precise experimental measurement of this linear dichroism is required, as these theoretical idealizations are the current basis of experimental methods for measuring molecular orientation.

Both the BB and the MO model have been widely used in the literature for the analysis of the orientation of alkanes such as alkyl thiol and semi-fluorinated self-assembled monolayers adsorbed on planar surfaces (see references [25], [26]). Here, the analysis is quite complex: the orientation of the spectroscopic TDM is described by a tilt angle (α) relative to the surface normal and an azimuthal angle about the surface normal (ϕ).[6] This azimuthal dependence will be averaged when multiple domains are present, such as in a typical self-assembled monolayer film.[6] The model relating the TDM to the molecular axis is then used to relate the spectroscopic angle dependence to the molecular orientation, using either the BB or the MO model. Several other factors can affect the magnitude of the linear dichroism. With any degree of azimuthal disorder, the intensity of the Carbon 1s $\rightarrow \sigma^*_{C\text{-}C}$ transition can not go to zero – even in the MO description – unless the alkane chain is oriented exactly normal to the sample surface ($\alpha = 0$). Disorder in the chain conformation and photon ellipticity will also reduce the magnitude of the linear dichroism.

To understand the linear dichroism in the Carbon 1s NEXAFS spectrum of linear alkanes, we need to experimentally characterize the absolute angle dependence of transitions found in its spectrum. For this, we require a highly-ordered sample, preferably a single crystal. In particular, we wish to avoid the azimuthal averaging

present in self-assembled monolayers. We also wish to measure the spectra of hexacontane (HC) at all possible angles between the x-ray electric field vector and the molecular chain axis. In a typical angle resolved NEXAFS measurement of a surface adsorbed molecule, the angle explored ranges between glancing (~20^o) to normal (90^o) incidence. Several possible orientations of the n-alkane molecule in *transmission geometry* are presented in Figure 2, where it is possible to rotate the sample azimuthally around the photon axis. When n-alkane chains are oriented normal to the sample surface, azimuthal rotation will not change the angle between the electric field vector and the alkane backbone axis (Figure 2a). However, if the alkane chains are induced to lie parallel to the sample surface (e.g. lateral orientation), azimuthal rotation can change the angle between the electric field vector and the alkane backbone axis, from 90° to 0°, as shown in Figure 2b. Consequently the angle dependence of the Carbon 1s $\rightarrow \sigma^*_{C\text{-}C}$ transition can be fully explored. We require a sample with the n-alkane chains laterally oriented in the plane of the sample surface.

This geometry requirement creates challenges for sample preparation. The simplest methods – solvent deposition of n-alkanes or the self-assembly of alkyl thiols – result in films where the chains are oriented approximately normal to the sample surface, usually with some disorder. We have selected epitaxial growth[27-29] on crystalline surfaces to prepare samples where the n-alkane molecules are oriented in the sample plane, using methods developed for electron crystallography.[30,31] Our results show that the alkane molecules prepared in this manner are laterally oriented. By controlling the deposition conditions, we can prepare films with smaller or larger oriented domains.[32]

Scanning Transmission X-ray Microscopy (STXM) is used to acquire angle resolved Carbon 1s NEXAFS spectra of a well-ordered, laterally oriented hexacontane (HC) thin film at a range of azimuthal angles. In the STXM microscope, it is possible to rotate the sample azimuthally around the photon axis, change the x-ray polarization vector inclination (with an elliptically polarized undulator source), select specific sample areas, evaluate the presence of domains with different molecular orientation, and monitor the radiation dose. We have determined the absolute angle dependence of the transitions in this spectrum, and with this data considered the validity of the molecular orbital and the building block models for the angle dependence of the Carbon 1s spectrum of n-alkanes.

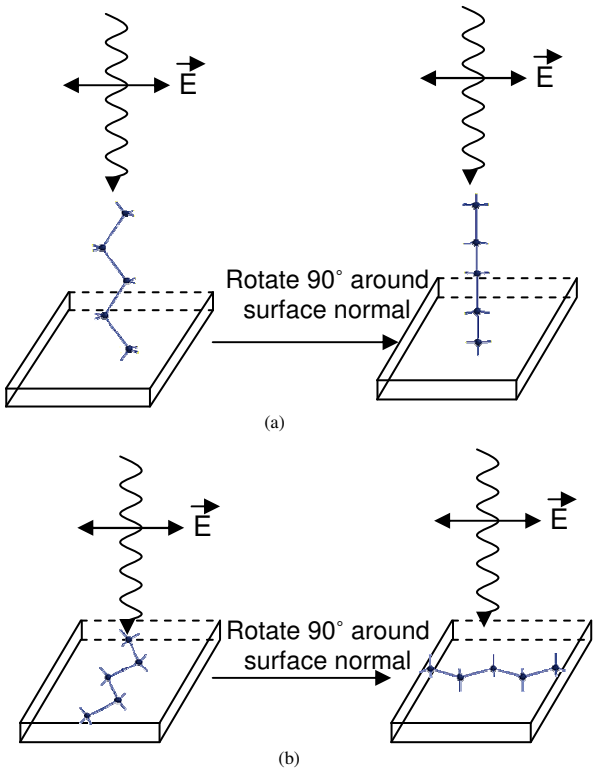

Figure 2 Schematic of alignment of linear alkane molecules relative to the substrate and the x-ray electric field vector. (a) alkane molecule oriented normal to the substrate surface; electric field vector parallel to the substrate surface; (b) alkane molecules laterally oriented; electric field vector parallel to the substrate surface.

2. Experimental Section

2.1 Materials and sample preparation

The linear alkane used in this study was hexacontane (n-$C_{60}H_{122}$, HC) (Sigma Aldrich, 98% purity), used without further purification. The single crystal NaCl substrates used were surplus FTIR windows. Clean surfaces were prepared by cleaving the NaCl single crystal to expose a fresh (001) crystal plane. The substrates were placed in a high vacuum chamber (Datacomp Scientific), and the evaporation was performed in a vacuum of 10^{-7} torr from a resistively heated tungsten boat. The average thickness of the deposited films was measured with a quartz crystal microbalance. In order to have adequate absorption at the Carbon 1s core edge, the sample thickness was maintained in the 100 - 150 nm range. A quartz light bulb heater and a thermocouple were used to control the temperature of the NaCl substrate during the HC deposition. After deposition, the NaCl substrate was dissolved in water (obtained from a Millipore water purification system, 18 MΩ) to separate the HC thin films from the substrate. The floating HC films were picked up on Si_3N_4 windows [Silson Ltd.] for x-ray microscopy experiments.

2.2. NEXAFS Spectroscopy

NEXAFS images and spectra were recorded at the Advanced Light Source (ALS) in Berkeley on two Scanning Transmission X-ray Microscopes (STXM): the Polymer-STXM at beamline 5.3.2[33] and the molecular environmental sciences MES-STXM at beamline 11.0.2.[34] The Polymer STXM is on a bending magnet source, where we expect a photon polarization of 80 – 90% ellipticity, oriented in the horizontal plane. The MES-STXM is mounted on an elliptically polarized undulator (EPU) source,

where the linear polarization can be inclined from horizontal to vertical (e.g. 0 – 90°).[35] The degree of linear polarization on this EPU has been measured to be 100% (+0/-1%) linearly polarized at several different inclinations.[36] The resolving power of the monochromator was 1900 for the 5.3.2 STXM beamline and 2500 for the 11.0.2 MES-STXM beamline.

All spectra were acquired in transmission mode and are reported as optical density versus energy (eV). The optical density (OD), derived from the Beer-Lambert law, is obtained from $OD = -\ln(\frac{I}{I_0}) = \mu \cdot \rho \cdot t$, where for a given X-ray energy, I_0 is the incident flux (measured through a hole in the thin film), I is the transmitted flux through the sample, t is the sample thickness, μ is the mass absorption coefficient, and ρ is the density. Since this sample is sensitive to radiation, special precautions were taken when obtaining fine scale images and spectra. To avoid the accumulation of radiation damage, each spectrum was acquired from a unique sample area.

3. Results and discussion

3.1. Carbon 1s NEXAFS Spectroscopy of Hexacontane

Figure 3 presents Carbon 1s NEXAFS spectra of a well-oriented HC thin film recorded at two different angles of the x-ray electric field vector with respect to the chain axis, along with the Cartesian coordinate system used for this molecule. The molecule HC belongs to the point group C_{2h} and we use the following coordinate system to describe its orientation: All carbon atoms lie in the yz plane, the overall macromolecular axis is along the z-axis and the CH_2 groups lie in the xy plane.

In Figure 3, the absence of a 285 eV feature demonstrates the low level of radiation damage in this typical exposure time. The band at ~288 eV (below the

ionization potential) is traditionally assigned as the Carbon 1s $\rightarrow \sigma^*_{C\text{-}H}$ band.[7,23,37] This band has the strongest intensity when the electric field vector is perpendicular to the alkane chain, e.g. oriented in the CH_2 or xy plane (line with data points in Figure 3). In early electron energy loss spectra of gas phase alkanes, this pre-edge band was assigned as 3s and 3p / $\pi^*(CH_2)$ transitions.[38] The similarity of the Carbon 1s spectra of gaseous and condensed cyclic alkanes led Hitchcock *et al.* to conclude that $\sigma^*_{C\text{-}H}$ character was dominant in this mixed Rydberg / valence character state.[39] When Carbon 1s spectra of alkanes were recorded with much higher energy resolution, features were unambiguously assigned as Rydberg transitions,[35,40,41] although discussion of the degree of valence character is ongoing.[42,43] Curiously, Bagus *et al*.[25,44] concluded that pre-edge resonances in the Carbon 1s spectra of *condensed* alkanes were predominantly Rydberg character even though it is generally expected that Rydberg states will be quenched in the solid state. Recent DFT calculations of Weiss *et al* for n-octane show mixed valence – Rydberg character.[43]

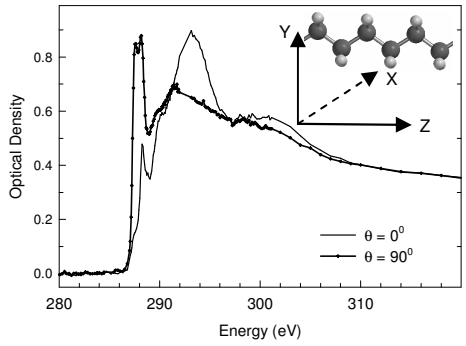

Figure 3 Carbon 1s NEXAFS spectra extracted from orthogonally oriented domains of HC, deposited on a freshly cleaved NaCl (001) surface at a room temperature substrate during evaporation. The spectrum (solid line) is extracted from domains that correspond to the angle θ=0°, i.e. with the E vector oriented along the macromolecular backbone. The spectrum (line + data point) is extracted from domains that correspond to the angle θ = 90°, i.e. with the E vector oriented perpendicular to the

macromolecular backbone. The molecular schematic illustrates the Cartesian coordinate conventions used in this paper.

The resonances observed *above* the ionization threshold are often described within two variations of the shape resonance model. A *chemical orbital* model relates the character of the continuum resonances to the character of the unoccupied molecular orbitals,[45,46] in which these resonances are described as "core → σ* resonances" embedded in the continuum. This approach has the advantage of providing a direct relationship between the molecular structure and its spectrum through the familiar and predictive language of molecular orbital theory. Alternatively, continuum resonances are described by the trapping of the outgoing photoelectron by a potential barrier of the molecule;[47] this model is computationally studied with multiple scattering calculations.[48]

These shape resonances are frequently used in a building block approach, where the spectrum of a complex molecule is treated as the assembly of diatomic or psuedodiatomic fragments.[6] This building block model is the basis of the controversial bond length correlation method,[6,49] as well as the BB approach for linear dichroism described above.[6] Recently, Piancastelli provided a critical review of these shape resonance interpretations.[22] Multiple excitation, shake-up continuum and shake-off continuum features are also considered as the origin of continuum features.

In the Carbon 1s NEXAFS spectrum of alkanes, there are two dominant features above the ionization potential that show angular dependence: a strong band at ~293 eV, and a weaker band at 301.1 eV. For convenience, we will use the traditional assignments of these transitions, e.g. as Carbon 1s → $\sigma^*_{C\text{-}C}$ and Carbon 1s → $\sigma^*_{C\text{-}C}$', respectively.[7]

3.2 Preparation of Laterally Oriented HC Thin Films

As outlined above, we require well-ordered n-alkane single crystals where the chains are oriented laterally in the sample plane and where the crystalline domains are large enough to permit the acquisition of several sequential spectra from the same domain. Radiation damage is a concern, and our sample area must be large enough to distribute the radiation dose from several sequential scans over a large enough sample volume to minimize the appearance of radiation damage. To estimate the sample area required, we performed a study of the radiation damage kinetics for HC following established procedures.[50,51] This procedure provides the critical dose – the radiation dose for the 1/e attenuation of the intensity of a particular transition or the corresponding increase in the intensity of a transition due to radiation damage. For HC, we found that the critical dose was 12 eV/nm^3 for the attenuation of the Carbon 1s $\rightarrow$ $\sigma^*_{C\text{-}H}$ transition and 32 eV/nm^3 for the increase in the Carbon 1s $\rightarrow$ $\pi^*_{C=C}$ transition, the latter corresponds to the formation of C=C double bonds by radiation damage.[52] With a guideline of keeping the total radiation damage below the critical dose for the Carbon 1s $\rightarrow$ $\sigma^*_{C\text{-}H}$ transition, we estimated that we would require an area of at least ~170 μm^2 in order to acquire 10 spectra at different sample angles with dwell times and scan lengths typical for adequate statistics.

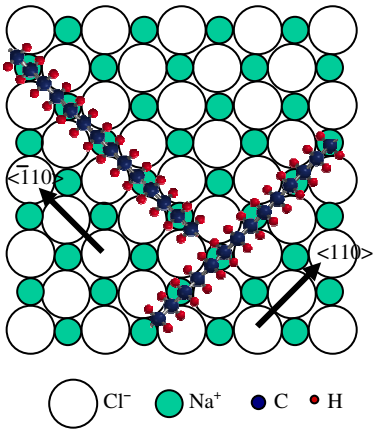

Figure 4 Expected epitaxial relationship between HC molecules and the NaCl (001) surface. The HC molecules (only 14 carbon atoms shown) are preferentially aligned along the two crystallographically equivalent <110> and <$\bar{1}$10>directions on (001) surface.

The expected epitaxial relationship between the NaCl (001) substrate and the HC molecules is shown in Figure 4. The high symmetry (cubic structure) and the ionic field force of NaCl induce the HC molecules to align on the NaCl (001) face along the crystallographically equivalent <110> and <$\bar{1}$10> directions.[31,53-55]

Oriented domains in samples prepared at room temperature are too small for reliable angle resolved NEXAFS spectroscopy measurements,[32] particularly within the radiation damage limits described above. However, we found that we can modify the size of these domains by controlling the substrate temperature during film deposition.[30,31,56] Figure 5a presents an x-ray microscopy image recorded at 287.6 eV of an HC thin film evaporated onto freshly cleaved NaCl(001) where the substrate temperature was held at 45°C during deposition. The image contrast is more uniform, consisting of an open area, a matrix (dark grey), and smaller dispersed domains (light grey). In Figure 5b, the image contrast inverts when the sample is rotated by ~70^o about the photon axis (NB this measurement was made using the bending magnet

polymer STXM, where the x-ray electric field vector is horizontal). This sample consists of a majority phase aligned in one direction and a number of minority phases aligned at right angles to the majority phase. The morphological differences of this sample relative to the sample deposited at room temperature suggests that some additional energy is required to create larger crystals of HC by epitaxial growth.[30] For the sample prepared at room temperature, there is less thermal energy to promote molecular diffusion and molecular movement on the substrate is limited. This leads to a higher effective density of nucleation sites and the formation of smaller crystallites. The sample deposited with a substrate temperature of 45°C has large enough domains for our intended angle resolved NEXAFS measurements.

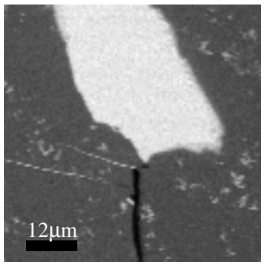

(a)

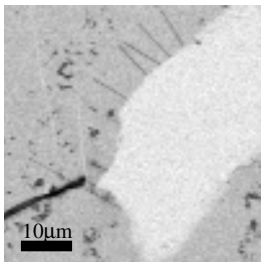

(b)

Figure 5 X-ray microscopy images of HC films epitaxial growth onto a freshly cleaved NaCl (001) surface by thermal evaporation with substrate temperature of 45°C during evaporation. These images were acquired with an x-ray energy of 287.6eV. For image (b), the sample has been rotated by 70°.

3.3. Measurement of the Angular Dependence of NEXAFS Spectra

Angle-resolved NEXAFS spectra were measured on the bending magnet polymer-STXM (beamline 5.3.2) and elliptical polarized undulator (EPU) MES-STXM

microscopes (beamline 11.0.2) at the Advanced Light Source. Since the bending magnet source is horizontally polarized, the sample must be rotated azimuthally around the photon axis using a rotation cell to measure the linear dichroism. Since the orientation of a particular domain is not initially known, measurements were made at a series of angles and the intensity of the Carbon 1s $\rightarrow \sigma^*_{C\text{-}H}$ band was monitored as a function of angle. The angle at which the intensity of the Carbon 1s $\rightarrow \sigma^*_{C\text{-}H}$ band reaches a minimum or a maximum was defined as $\theta = 0°$ and $\theta = 90°$, respectively. In the EPU measurements, the x-ray polarization can be changed from horizontal (EPU=0°) to vertical (EPU=90°) by shifting the EPU phase.[57] Nevertheless, it was still necessary to rotate the sample manually for the EPU measurements, as the 0 – 90 degree range of linear polarization inclination can not cover the full angle range if the molecular domains are not perfectly aligned in the horizontal or vertical directions. Here, we only report the EPU data as we found a systematic attenuation in the intensity of stronger transitions in the bending magnet spectra. There are two potential origins for these differences: photon ellipticity and higher harmonic photon contamination. The increased ellipticity of a bending magnet source will decrease the *magnitude* of the linear dichroism, e.g. decrease the intensity of the 293.5 eV Carbon 1s $\rightarrow \sigma^*_{C\text{-}C}$ transition and increase the intensity of the orthogonally oriented pre-edge Carbon 1s $\rightarrow \sigma^*_{C\text{-}H}$ transition, or vice versa. However, we found that the intensity of all strong features was attenuated in the bending magnet spectra, indicating that ellipticity alone is not responsible for the difference.

Higher harmonic contamination is a particular concern for the bending magnet STXM which uses a spherical grating monochromator (SGM). The SGM

monochromator produces significant second and third order harmonics, while the plane grating monochromator of the MES-STXM beamline does not produce higher harmonics as efficiently. As higher harmonics will not be absorbed by the sample as efficiently as first order photons, both the I and I_o signals will be artificially higher than for a pure radiation source, and the magnitude of the optical densities will be suppressed, as we observe.

Several causes of higher order contamination are specific to the STXM microscopes used for these experiments. The order sorting aperture should filter out higher harmonic photons, but small misalignments will lead to the transmission of these higher harmonics. These higher harmonics can be transmitted directly through the central stop of the zone plate focusing element if this element is not thick enough to prevent transmission at the energies of the harmonics.

Because the bending magnet spectra are systematically distorted, we will only use data acquired with the EPU source (MES-STXM) for the subsequent analysis. Proper consideration of these experimental factors is essential when acquiring NEXAFS spectra for linear dichroism studies.

Figure 6 presents the Carbon 1s NEXAFS spectra of HC, recorded at 10 different angles, using the EPU source.

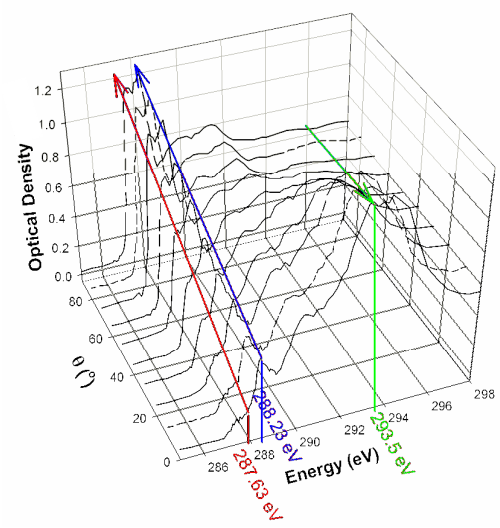

Figure 6 Carbon 1s NEXAFS spectra of an oriented HC thin film, prepared at a substrate temperature of 45°C during evaporation, presented as a function of angle. These data were recorded using the MES – STXM microscope, by inclining the direction of the linear polarization and rotating the sample.

We have used the MGAUSS program[58] to determine the angle dependence of features in our set of NEXAFS spectra. MGAUSS allows us to simultaneously fit the entire set of spectra to a common set of linked and independent parameters. In the angle resolved spectra, we expect the *intensities* of specific features to vary but their *position* and *width* to remain invariant. Therefore, we constrained the energy and the width of spectroscopic features so they vary *identically* for all of the spectra in the simultaneous fit, while allowing the intensity of each feature to vary independently. To achieve the best fit of the 10 spectra recorded with different angles θ, 8 Gaussian curves were used to correspond to the spectral features and an error step function[6] was used to model the ionization edge of carbon. This error step function was fixed at 289.7 eV, 1.0 eV lower than the ionization potential of propane in the gas phase.[59] An orientation independent background was also used. The parameters for the positions

and shapes of the various NEXAFS resonances with angular dependent intensity are listed in Table 1.

Table 1 Energy and full width at half maximum of transitions optimized from the MGAUSS fit of the Carbon 1s spectra of HC.

Peak position (eV)	287.63	288.23	288.51	289.1	291.5	293.5	296.0	301.1
FWHM (eV)	0.51	0.68	0.54	2.28	1.31	3.56	5.97	7.90

Figure 7 presents the angular dependence of Carbon 1s NEXAFS spectra of HC films obtained on the MES-STXM at 3 representative angles, θ = 0°, 50° and 90°.

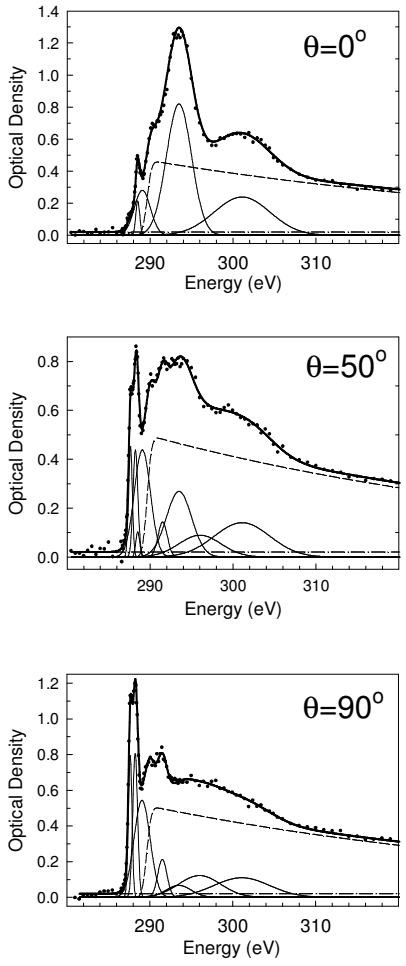

Figure 7 Fits of the Carbon 1s NEXAFS spectra of HC films at three representative angles (θ=0°, 50°, and 90°), fitted by MGAUSS program. These data were obtained using the elliptically polarized undulator (ALS beamline 11.0.2), for an HC sample

deposited onto the NaCl(001) surface at a substrate temperature of 45°C during evaporation. The dotted line represents the experimental measured spectra; the thick solid line represents the best fitted spectra; thin solid line, Gaussian peaks; dashed line, error step function; and dash-dot line, background.

Figure 8 presents the optical density of each resonance as a function of angle (θ) and $\cos^2\theta$. The $\cos^2\theta$ plot provides a diagnostic of experimental quality, as experimental linear dichroism data should have a $\cos^2\theta$ dependence (see equation 1). The $\cos^2\theta$ plots in Figure 8 are linear with the exception of the trace for the 293.5 eV feature. The linearity of all but one trace demonstrates that the experiment is free from major artifacts, and several reasons can be provided for the deviation of the one trace from linearity. This transition is the most intense continuum resonance, so it will be most sensitive to deficiencies in the functions used for the fit. We note that the continuum resonances are not the symmetric Gaussians as used in the fit, but rather are asymmetrically broadened by vibration.[6] Nevertheless, we fit these features with symmetric Gaussian functions as the addition of more functions to model this asymmetry would lead to overlap with other resonances, and prevent us from tracking a specific resonance as a function of angle. This error will be highest when the 293.5 eV feature is most intense. However, this approach is a necessary compromise for the analysis of our data. When the 293.5 eV feature is at its minimum intensity, we find that radiation induced molecular reorientation prevents us from observing zero intensity for this transition. This effect will be discussed below.

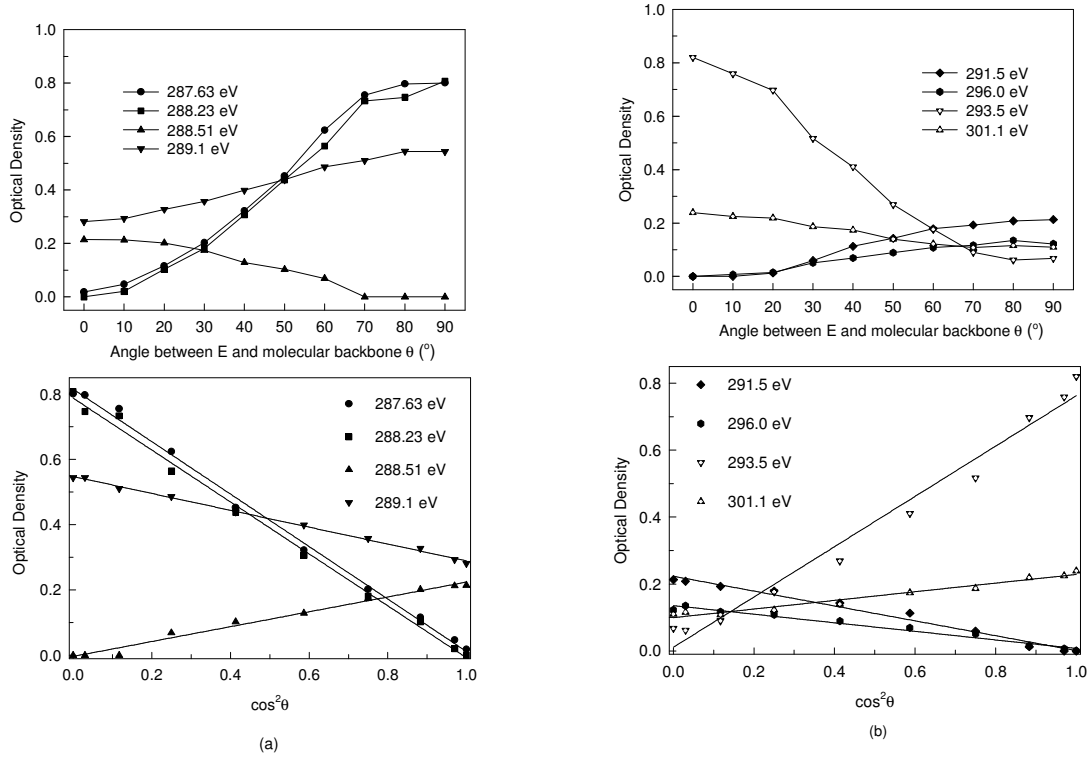

Figure 8 The optical density of resonances in the Carbon 1s NEXAFS spectrum of HC as a function of angle θ and $\cos^2\theta$.

Four resonances were observed below the ionization potential in the spectral fit: at 287.63 eV, 288.23 eV, 288.51 eV and 289.1 eV (see Table 1). The resonances at 287.63 eV and 288.23 eV show a strong angle dependence with a maximum intensity when the electric field vector is oriented normal to the HC chain. The third resonance, at 288.51 eV, has an opposite angle dependence and a maximum intensity when the electric field vector is oriented along the macromolecular axis. The fourth Gaussian in the fit, at 289.1 eV, is unexpectedly broad and straddles the ionization potential. The inclusion of this Gaussian function is required for a good fit of the data, but given its character and the fact that we cannot observe this feature in the raw spectra, we do not assign it direct physical significance.

The first two transitions are considered to be Carbon 1s $\rightarrow \sigma^*_{C\text{-}H}$ transitions, as the TDM is oriented in the plane of the CH_2 group (e.g. xy plane, orthogonal to the

macromolecular backbone). The energy separation between these two resonances is 602 meV, in close agreement with the theoretical calculation value of 650 meV for n-octane.[43]

The intensity of the first two transitions goes nearly to zero when the electric field vector is aligned along the macromolecular backbone ($\theta = 0°$). This contrasts with the results of Hähner *et al*,[7] in which the intensity of the C-H band decreases to approximately 30% of the maximum feature intensity. However, the data of Hähner *et al* does not have adequate energy resolution to resolve this third transition. The inclusion of the third transition in the fit, with its orthogonal angle dependence, will result in the incorrect angular dependence observed by Hähner *et al*. Ironically, their C-H angle dependence looks like the hypothesized "building block" angle dependence (Figure 1), although this interpretation is not plausible for the planar CH_2 geometry. This observation demonstrates that adequate spectral resolution is required to properly characterize the angle dependence in these spectra. Conclusions regarding the electronic structure and molecular orientation based on insufficiently resolved spectra should be viewed with caution.

What is the spectroscopic character of the third pre-edge transition? We are reluctant to characterize this transition as a Carbon 1s $\rightarrow \sigma^*_{C\text{-}H}$ transition, as its TDM is oriented along the z axis, orthogonal to the CH_2 plane. We have considered that this transition might originate from the terminal CH_3 groups on the HC chain, as we expect a "C-H" component from the terminal CH_3 groups oriented along the macromolecular backbone direction. However, a stoichiometric calculation shows that this hypothesis is improbable. In HC, there are 6 C-H bonds in the terminal CH_3 groups versus 116 C-H

bonds in methylene groups, i.e. 5% of the C-H spectroscopic intensity will originate from the CH_3 group. Therefore the third peak is greater than would arise from stoichiometric considerations of the CH_3 group. Since this transition lacks the symmetry of a C-H resonance, a simple orbital picture of energy separated C-H and C-C σ^* bands do not hold. This C-H band has components in all three Cartesian.

We may be able to rationalize the character of this third transition by considering the role of Rydberg – valence mixing in the Carbon 1s NEXAFS spectrum of HC. The Carbon 1s $\rightarrow$ 3s transition, and the Carbon 1s $\rightarrow$ 3p Rydberg transition components directed in the xy plane can mix with states of $\sigma^*_{C\text{-}H}$ character.[42] Further, we expect that states of Rydberg character will be quenched in the solid state, so the transitions directed in the xy plane will be predominantly valence $\sigma^*_{C\text{-}H}$ character in condensed alkanes. In contrast, the 3p Rydberg component directed along the z axis can not mix with states of $\sigma^*_{C\text{-}H}$ character and will remain as "pure Rydberg", with some quenching in the molecule, likely blue shifted relative to the unquenched atomic Rydberg. We believe that the origin of this third peak is an incompletely quenched $3p_z$ Rydberg transition, which can by symmetry not support mixing with states of $\sigma^*_{C\text{-}H}$ character. Such mixed and unmixed Rydberg states are observed in the gas phase NEXAFS spectra of simple alkanes.[42]

Above the ionization potential, four resonances are resolved in the fit: at 291.5 eV, 293.5 eV, 296.0 eV, and 301.1 eV (see Table 1, Figure 8b). Each transition can be directly observed in at least a subset of the experimental data. The strong 293.5 eV and 301.1 eV transitions are assigned as Carbon 1s $\rightarrow$ $\sigma^*_{C\text{-}C}$ and Carbon 1s $\rightarrow$ $\sigma^*_{C\text{-}C}$' transitions, respectively, by Stöhr *et al.*[60], Hähner *et al.*[7] and Weiss *et al.*[43]

Our angle dependence data show that the intensity of the resonances at 293.5 eV and 301.1 eV is strongest when the electric field vector is aligned along the macromolecular or z axis. This is consistent with $\sigma^*_{C\text{-}C}$ character. In contrast, the resonances at 291.5 eV and 296.0 eV exhibit an opposite angular dependence, with maximum transition intensity occurring when the electric field vector is normal to the macromolecular axis. These transitions lack the symmetry expected for a Carbon 1s $\rightarrow$ $\sigma^*_{C\text{-}C}$ transition, in either the BB or MO model, and like the third (288.51 eV) transition in the C-H band, do not fit into a simplistic $\sigma^*_{C\text{-}C}$ orbital picture. The origin of these transitions is unclear.

Interestingly, it appears that features with a TDM along all three Cartesian components (xy plane, z axis) are observed in the $\sigma^*_{C\text{-}C}$ band just as in the $\sigma^*_{C\text{-}H}$ band. The observation of multiple, overlapping peaks in the $\sigma^*_{C\text{-}C}$ band with an orthogonal orientation dependence raises a caution about the use of these spectra for orientation analysis.

The Carbon 1s $\rightarrow$ $\sigma^*_{C\text{-}C}$ transition at 293.5 eV exhibits the largest change with angle. This observation begs the question: does the angle dependence of this resonance follow the BB or the MO picture? We find that the ratio of the maximum to minimum optical density for this resonance is 13, approximately 6.5 times larger than the ratio based on the BB model. This result unambiguously excludes the BB model as a valid interpretation for this transition. On first glance, the MO model does not appear to be valid either as this would require the intensity of the transition to go to zero at $\theta = 90^o$. We will present several reasons why the transition might not go to zero: photon ellipticity, sample disorder and radiation damage. Photon ellipticity can be excluded as

the degree of linear polarization on the EPU beamline is 100% (+0/-1%). A small degree of disorder might be present in the as-deposited HC samples. Radiation may also cause a decrease in the degree of molecular alignment. Figure 9 presents the NEXAFS spectra of the oriented HC sample (from Figure 7, θ =0°) obtained after a small radiation dose (0.43 eV/nm^3) and a larger radiation dose (2.0 eV/nm^3). Comparison of these spectra shows that the optical density of the first resonance of Carbon 1s $\rightarrow \sigma^*_{C\text{-}H}$ (287.63 eV) *increased* with radiation dose while the optical density of Carbon 1s $\rightarrow \sigma^*_{C\text{-}C}$ (293.5 eV) transition *decreased*. These *linear dichroism changes* indicate that the HC chains no longer have the same degree of alignment after the higher radiation dose. These exposures are well below the critical doses required for *chemical* changes in HC, which leads to the loss of C-H bond (12 eV/nm^3) and formation of C=C bonds (32 eV/nm^3, see §3.2). Indeed, the loss of C-H bond would attenuate the 288 eV region but have no effect on the Carbon 1s $\rightarrow \sigma^*_{C\text{-}C}$ transitions. However, since we see a clear linear dichroism effect – an *increase* in the Carbon 1s $\rightarrow \sigma^*_{C\text{-}H}$ transition and a *decrease* in the Carbon 1s $\rightarrow \sigma^*_{C\text{-}C}$, these changes can be directly attributed to molecular reorientation.

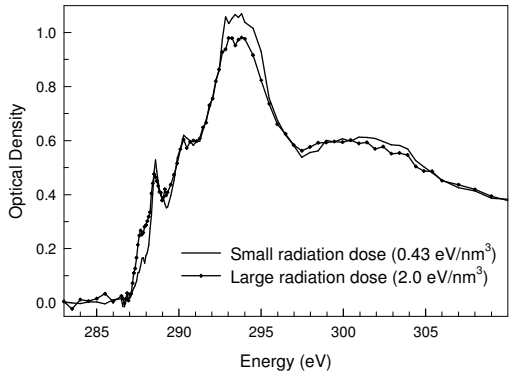

Figure 9 Molecular reorientation in HC induced by radiation dose.

The origin of this reorientation is a matter of speculation. One might consider that a temperature rise from the radiation exposure might induce molecular reorientation, although these radiation doses (2.0 eV/nm^3) are very low. A more likely scenario is that the radiation exposure causes fragmentation of the HC chains, where the fragments can reorient at ambient temperatures. Only one C-C bond needs to be broken to change HC (n-$C_{60}H_{122}$) into two C_{30} fragments (or any other logical combination of fragment lengths). As the melting point of a C_{30} chain (65~67 °C) is ca. 30 °C below that of HC, chain fragmentation from radiation damage will lead to a distribution of shorter molecular chains which can then undergo melting or reorientation at lower temperatures. The *chemical* effect of breaking *one bond* in a relatively long chain might not be visible spectroscopically, while the *physical* changes from the reduced melting point certainly can be. This observation is very unusual, as most radiation damage in NEXAFS spectroscopy is observed as chemical changes.[50,51] These changes are analogous to the loss in crystallinity observed with radiation exposure in electron crystallography measurements.

4. Conclusions

Linear dichroism in the Carbon 1s NEXAFS spectra of n-hexacontane has been systematically explored. HC crystals with lateral orientation were prepared by epitaxial growth on a cleaved NaCl (001) surface.

This study shows that failure to properly resolve spectroscopic features with a differing angle dependence will lead to an erroneous measurement of the angle dependence of the NEXAFS spectra, and from this, an incorrect description of the

spectroscopic transition dipole moment. These errors are likely to lead to an inaccurate measurement of molecular orientation based on the angle resolved NEXAFS spectra.

The analysis of angle resolved NEXAFS spectra indicate that the transition dipole moment (TDM) for the Carbon 1s $\rightarrow \sigma^*_{C\text{-}C}$ transition at 293.5 eV in linear alkanes is oriented along the macromolecular backbone, most closely corresponding to the molecular orbital model and explicitly excluding the building block model. However, transitions are observed in both the $\sigma^*_{C\text{-}C}$ and the $\sigma^*_{C\text{-}H}$ band that are oriented orthogonal to the primary transitions. These transitions do not fit into the conventional $\sigma^*_{C\text{-}H}$ and $\sigma^*_{C\text{-}C}$ band descriptions.

We observe that radiation damage can be manifest as a change in molecular orientation at a dose significantly below that for the observation of conventional x-ray radiation damage in the form of chemical bond breakage and formation.

Acknowledgements

This research was supported by the Natural Sciences and Engineering Research Council, the Canadian Foundation for Innovation, the Saskatchewan Synchrotron Institute, the University of Saskatchewan and the Chemistry Department of the University of Saskatchewan. The authors are grateful to A.L.D. Kilcoyne and T. Tylizczak for help with the operation of the STXM microscopes at the ALS. The use of the ALS 5.3.2 STXM is supported by NSF DMR-9975694, DOE DE-FG02-98ER45737, Dow Chemical, an NSERC MFA, and the Canadian Foundation for Innovation. The ALS is supported by the Director, Office of Science, Office of Basic Energy Sciences, of the U.S. Department of Energy under Contract No. DE-AC03-76SF00098.

References:

(1) Norden, B. *Applied Spectroscopy Reviews* **1978**, *14*, 157.

(2) Rodger, A.; Norden, B. *Circular dichroism and linear dichroism*; Oxford University Press: Oxford, 1997.

(3) Schellman, J.; Jensen, H. P. *Chemical Reviews* **1997**, *87*, 1359.

(4) Crain, J. N.; Kirakosian, A.; Lin, J. L.; Gu, Y. D.; Shah, R. R.; Abbott, N. L.; Himpsel, F. J. *Journal of Applied Physics* **2001**, *90*, 3291.

(5) Charney, E. *Quarterly Reviews of Biophysics* **1988**, *25*, 1.

(6) Stöhr, J. *NEXAFS Spectroscopy*; Springer-Verlag, 1992; Vol. 25.

(7) Hahner, G.; Kinzler, M.; Woll, C.; Grunze, M.; Scheller, M. K.; Cederbaum, L. S. *Physical Review Letters* **1991**, *67*, 851.

(8) Kinzler, M.; Schertel, A.; Hähner, G.; Wöll, C.; Grunze, M. *J. Chem. Phys.* **1994**, *100*, 7722.

(9) Samant, M. G.; Stöhr, J.; Brown, H. R.; Russell, T. P.; Sands, J. M.; Kumar, S. K. *Macromolecules* **1996**, *29*, 8334.

(10) Ianoul, A.; Fleury, F.; Duval, O.; Waigh, R.; Jardillier, J. C.; Alix, A. J. P.; Nabiev, I. *Journal of Physical Chemistry B* **1999**, *103*, 2008.

(11) Pelletier, I.; Laurin, I.; Buffeteau, T.; Desbat, B.; Pezolet, M. *Langmuir* **2003**, *19*, 1189.

(12) Pelletier, I.; Bourque, H.; Buffeteau, T.; Blaudez, D.; Desbat, B.; Pezolet, M. *Journal of Physical Chemistry B* **2002**, *106*, 1968.

(13) Ade, H.; Hsiao, B. *Science* **1993**, *262*, 1427.

(14) Urquhart, S. G.; Ade, H. *Journal of Physical Chemistry B* **2002**, *106*, 8531.

(15) Urquhart, S. G.; Hitchcock, A. P.; Smith, A. P.; Ade, H. W.; Lidy, W.; Rightor, E. G.; Mitchell, G. E. *J. Electron Spectrosc. Relat. Phenom.* **1999**, *100*, 119.

(16) Cooney, R. R.; Urquhart, S. G. *J. Phys. Chem. B;* **2004**, *108*, 18185.

(17) Stöhr, J.; Outka, D. A. *Physical Review B* **1987**, *36*, 7891.

(18) Stöhr, J.; Samant, M. G.; Cossy-Favre, A.; Diaz, J.; Momoi, Y.; Odahara, S.; Nagata, T. *Macromolecules* **1998**, *31*, 1942.

(19) Genzer, J.; Sivaniah, E.; Kramer, E. J.; Wang, J.; Xiang, M.; Char, K.; Ober, C. K.; Bubeck, R. A.; Fischer, D. A.; Graupe, M.; Jr., R. C.; Shmakova, O. E.; Lee, T. R. *Macromolecules* **2000**, *33*.

(20) Genzer, J.; Sivaniah, E.; Kramer, E. J.; Wang, J. G.; Korner, H.; Char, K.; Ober, C. K.; DeKoven, B. M.; Bubeck, R. A.; Fischer, D. A.; Sambasivan, S. *Langmuir* **2000**, *16*, 1993.

(21) Fischer, D. A.; Mitchell, G. E.; Yeh, A. T.; Gland, J. L. *Applied Surface Science* **1998**, *133*.

(22) Piancastelli, M. N. *J. Electron Spectroscopy and Related Phenomena* **1999**, *100*, 167.

(23) Outka, D. A.; Stohr, J.; Rabe, J. P.; Swalen, J. D.; Rotermund, H. H. *Physical Review Letters* **1987**, *59*, 1321.

(24) Hu, H.; Dorset, D. L. *Acta Cryst.* **1989**, *b45*, 283.

(25) Bagus, P. S.; Weiss, K.; Schertel, A.; Wöll, C.; Braun, W.; Hellwig, C.; Jung, C. *Chemical Physics Letters* **1996**, *248*, 129.

(26) Genzer, J.; Sivaniah, E.; Kramer, E. J.; Wang, J. G.; Korner, H.; Xiang, M. L.; Char, K.; Ober, C. K.; DeKoven, B. M.; Bubeck, R. A.; Chaudhury, M. K.; Sambasivan, S.; Fischer, D. A. *Macromolecules* **2000**, *33*, 1882.

(27) Pashley, D. W. *Advances of Physics* **1965**, *14*, 327.

(28) Wellinghoff, S.; Rybnikar, F.; Baer, E. *Journal of Macromol Sci.----Phys.* **1974**, *B10*, 1.

(29) Wittmann, J. C.; Lotz, B. *Prog.Polym.Sci.* **1990**, *15*, 909.

(30) Zhang, W. P.; Dorset, D. L. *Journal of Polymer Science: Part B: Polymer Physics* **1989**, *27*, 1433.

(31) Ueda, Y.; Ashida, M. *Journal of Electron Microscopy* **1980**, *29*, 38.

(32) Fu, J.; Urquhart, S. G. *In preparation* **2005**.

(33) Kilcoyne, A. L. D.; Tyliszczak, T.; Steele, W. F.; Fakra, S.; Hitchcock, A. P.; Franck, K.; Anderson, E.; Harteneck, B.; Rightor, E. G.; Mitchell, G.; Yang, L.; Warwick, T.; Ade, H. *Journal of Synchrotron Radiation* **2003**, *102*, 125.

(34) Tyliszczak, T.; Warwick, T.; Kilcoyne, A. L. D.; Fakra, S.; Shuh, D. K.; Yoon, T. H.; Jr., G. E. B.; Andrews, S.; Chembrolu, V.; Strachan, J.; Acremann, Y. *AIP Conference Proceedings 705* **2004**, 1356.

(35) Ma, Y.; Chen, C. T.; Meigs, G.; Randall, K.; Sette, F. *Physical Review A* **1991**, *44*, 1848.

(36) Kortright, J., personal communication.

(37) Haack, N.; Ceballos, G.; Wende, H.; Baberschke, K.; Arvanitis, D.; Ankudinov, A. L.; Rehr, J. J. *Physical Review Letters* **2000**, *84*, 614.

(38) Hitchcock, A. P.; Ishii, I. *Journal of Electron Spectroscopy and Related Phenomena* **1987**, *42*.

(39) Hitchcock, A. P.; Newbury, D. C.; Ishii, I.; Stöhr, J.; Horsley, J. A.; Redwing, R. D.; Johnson, A. L.; Sette, F. *J. Chem. Phys.* **1986**, *85*, 4849.

(40) Remmers, G.; Domke, M.; Kaindl, G. *Physical Review A* **1993**, *47*, 3085.

(41) Ueda, K.; Okunishi, M.; Chiba, H.; Shimizu, Y.; Ohmori, K.; Sato, Y.; Shigemasa, E.; Kosugi, N. *Chemical Physics Letters* **1995**, *236*, 311.

(42) Urquhart, S. G.; Gillies, R. *Journal of Physical Chemistry A* **2005**, *109*, 2151.

(43) Weiss, K.; Oestroen, H.; Triguero, L.; Ogasawara, H.; Garnier, M. G.; Pettersson, L. G. M.; Nilsson, A. *Journal of Electron Spectroscopy and Related Phenomena* **2003**, *128*, 179.

(44) Weiss, K.; Woll, C.; Johannsmann, D. *Journal of Chemical Physics* **2000**, *113*, 11297.

(45) Hitchcock, A. P.; Brion, C. E.; Van der Wiel, M. J. *Journal of Physics B: Atom. Molec. Phys.* **1978**, *11*, 3245.

(46) Farren, R. E.; Sheehy, J. A.; Langhoff, P. W. *Chemical Physics Letters* **1991**, *177*, 307.

(47) Dehmer, J. L. *Journal of Chemical Physics* **1972**, *56*, 4496.

(48) Thiel, W. *Journal of Electron Spectroscopy* **1983**, *31*, 151.

(49) Sette, F.; Stöhr, J.; Hitchcock, A. P. *Chemical Physics Letters* **1984**, *110*, 517.

(50) Rightor, E. G.; Hitchcock, A. P.; Ade, H.; Leapman, R. D.; Urquhart, S. G.; Smith, A. P.; Mitchell, G.; Fischer, D.; Shin, H. J.; Warwick, T. *J. Phys. Chem. B* **1997**, *101*, 1950.

(51) Coffey, T.; Urquhart, S. G.; Ade, H. *Journal of Electron Spectroscopy and Related Phenomena* **2002**, *122*, 65.

(52) The radiation dose was calculated by Dose = (E x n1 x n2) / (V x eff.) where E is the energy at which the image was taken, n1 is the number of absorbed photons per pixel, n2 is the number of pixels, V is the volume of the sample and eff. is the efficiency of the detector, here we assume 30%.

(53) Ashida, M.; Ueda, Y.; Watanabe, T. *Journal of Polymer Science: Polymer Physics Edition* **1978**, *16*, 179.

(54) Mauritz, K. A.; Baer, E.; Hopfinger, A. J. *Journal of Polymer Science: Polymer Physics Edition* **1973**, *11*, 2185.

(55) Wittmann, J. C.; Hodge, A. M.; Lotz, B. *Journal of Polymer Science: Polymer Physics Edition* **1983**, *21*, 2495.

(56) Shimizu, H.; Tanigaki, N.; Nakayama, K. *Jpn. J. Appl. Phys.* **1995**, *34*, L701.

(57) Young, A. T.; Arenholz, E.; Marks, S.; Schlueter, R.; Steier, C.; Padmore, H. A.; Hitchcock, A. P.; Castner, D. G. *Journal of Synchrotron Radiation* **2002**, *9*, 270.

(58) Tyliszczak, T. MGAUSS Program, McMaster University.

(59) Siegbahn, K.; Nordling, C.; Johansson, G.; Hedman, J.; Heden, P. F.; Hamrin, K.; Gelius, U.; Bergmark, T.; Werme, L. O.; Manne, R.; Baer, Y. *ESCA applied to free molecules*; Amsterdam, North-Holland Pub. Co., 1969.

(60) Stöhr, J.; Outka, D. A.; Baberscke, K.; Arvanitis, D.; Horsley, J. A. *Phys. Rev. B* **1987**, *36*, 2976.

3.4 Theoretical calculations

This section documents the calculation results of the linear dichroism for the NEXAFS resonances of *n*-alkane molecules. This work is in preparation and presented here as a manuscript.

The author of this thesis designed the cluster models, did the calculations on the isolated alkane molecule and alkane clusters, and prepared the manuscript in close collaboration with Dr. Urquhart.

The author of this thesis obtained Dr. Urquhart's agreement to present the work in this thesis.

Linear Dichroism in the NEXAFS Spectra of n-alkanes – a theoretical study

Juxia Fu[a], *Harald Ade*[b], *Stephen G. Urquhart*[a,*]

[a]Department of Chemistry, University of Saskatchewan, Saskatoon, SK, S7N 5C9

[b]Department of Physics, North Carolina State University, Raleigh, NC, 27695

The ab initio calculations were used to calculate the C 1s NEXAFS spectra of an isolated nonane molecule, nonane cluster, and propane cluster. The linear dichroism for the NEXAFS resonances above the C 1s IP is investigated by calculating the isolated nonane molecule using minimal basis set. The character of the NEXAFS resonances below the C 1s IP is determined by comparing the calculated NEXAFS spectra of an isolated nonane molecule and nonane cluster. The linear dichroism for these features is then determined.

Version: alkane-LD-calc-v0.7.doc, last modified: August 18, 2006
* Corresponding author: email Stephen.urquhart@usask.ca

1. Introduction

Alkanes are simple organic materials. They are the major components of Langmuir-Blodgett (LB) films and self-assembled monolayers (SAM). The molecular orientation of the alkane chain is important for the measurement of the tilt angle of such films with respect to the substrate. Therefore, the accurate measurement of the alkane orientation is essential. Near edge X-ray absorption fine structure (NEXAFS) spectroscopy has been employed quite often to determine this alkane orientation from the linear dichroism of the absorption spectra near the C 1s absorption edge.[1-3]

In the NEXAFS spectra of n-alkanes, two types of resonances are identified with the C 1s ionization potential (IP) as a threshold. For the NEXAFS resonances below the C 1s IP, the character of these resonances is controversial. Traditionally, Rydberg character has been considered to be "quenched" upon condensation[4] and the features below C 1s IP are assigned as C 1s $\rightarrow \sigma^*_{C\text{-}H}$ valence transitions.[1,4,5] However, Bagus *et al.*[6] have assigned these features as C 1s $\rightarrow$ Rydberg transitions, based on high quality *ab initio* calculations of an *isolated* propane molecule. However, their computational model is problematic as an *isolated* propane molecule lacks any of the critical intermolecular interactions that should lead to modification of Rydberg states in the condensed phase. Matrix effects have been considered in the calculation of the NEXAFS spectra of propane on a small cluster (a trimer and a septamer).[7] However, these clusters have a small radius and are therefore very likely to lead to anomalous Rydberg states. Figure 1 compares the C 1s NEXAFS spectrum of gaseous and condensed phase neopentane.[8] It is evident that there are large differences between gaseous and condensed phase spectra, due to the quenching of Rydberg states.

Therefore, in order to accurately determine the electronic behavior in condensed molecules, the intermolecular interaction, even weak, has to be considered. The explanation based on calculations of isolated molecules is insufficient.[9]

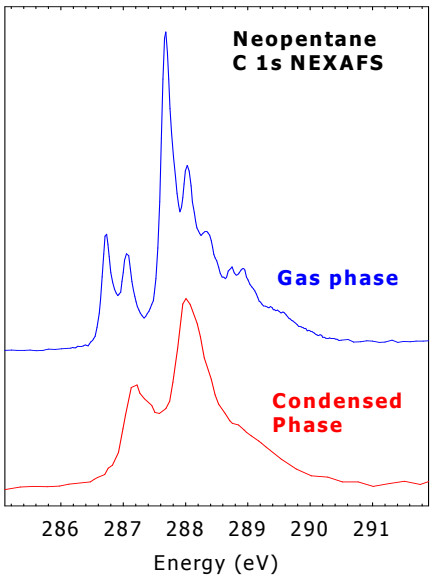

Figure 1 C1s NEXAFS spectra of neopentane in gas phase and condensed phase[8]

The NEXAFS resonances observed above the C 1s IP for n-alkanes are often described within two variations of the shape resonance model. A chemical orbital model relates the character of the continuum resonances to the character of the unoccupied molecular orbitals,[10] in which these resonances are described as C 1s $\rightarrow$ $\sigma^*_{C\text{-}C}$ resonances embedded in the continuum. This approach has the advantage of providing a direct relationship between the molecular structure and its spectrum through the familiar and predictive language of molecular orbital theory. Alternatively, continuum resonances are described by the trapping of the outgoing photoelectron by a potential barrier of the molecule.[11] In addition, multiple excitation, shake-up

continuum, and shake-off continuum features are also considered as the origin of continuum features.[12]

The linear dichroism for the first C 1s $\rightarrow \sigma^*_{C\text{-}C}$ resonance is often used to derive the alkane molecular orientation from the polarization dependent NEXAFS spectra. However, the transition dipole moment (TDM) of this transition is under debate. In the building block (BB) model, the TDM of this transition is considered to be along the individual C-C bond.[1,13] While the molecular orbital (MO) model[2,3] considers the TDM is along the macromolecular axis. Both models are extensively used in the literatures to derive the molecular orientation of LB and SAMs. We have measured the absolute angle dependent NEXAFS spectra of hexacontane (n-$C_{60}H_{122}$) thin films,[14] in which we showed that the building block model used by many groups provides an inaccurate measurement of the orientation on alkyl molecules

The objective of this paper is dual: for the NEXAFS resonances above the C 1s IP, we wish to gain insight of the TDM for these resonances from theoretical calculations. For the NEXAFS resonances below the C1s IP, we wish to gain insight about the Rydberg-valence mixing in these features for condensed *n*-alkanes, and therefore to determine the TDM of each feature below the C 1s IP. To do so we employed the self-consistent field Hartree-Fock (SCF-HF) method to calculate the NEXAFS spectra of an isolated nonane molecule, nonane cluster, and propane cluster.

2. Calculation

ab initio calculations have been performed using Kosugi's GSCF3 package[15] on isolated *n*-alkane molecules and clusters designed to model a solid. These calculations are based on the Improved Virtual Orbital approximation (IVO), which explicitly takes

into account the core hole in the Hartree-Fock approximation and are highly optimized for inner-shell excitation and ionization calculations.[16] In this approach, the 1s electron is removed directly from a molecular orbital, corresponding to a specific 1s orbital, as specified by the user. The improved virtual orbital provides a good approximation to the term value of the core excitation features at a specified core site.[15]

To obtain the character of the NEXAFS features above the IP, the GSCF3 calculations were carried out on a single nonane molecule using minimal basis set, which is described in §2.3. The nonane (n-C_9H_{20}) molecule is long enough so that the effect of the end CH_3 groups on the electronic structure of the central CH_2 group can be ignored, therefore, the calculation on the central CH_2 group can be used as a model for the carbon atoms in longer n-alkane chain. For the NEXAFS features below the C 1s IP, the GSCF3 calculations were carried out on a single nonane molecule, nonane cluster, and propane cluster using moderate basis set (§2.3). These calculations were performed at two levels of theory – IVO that has been described above and 'shielding refined IVO' that will be described in §2.4, using the Gaussian-type basis set of Huzinaga *et al*.[17] The molecular geometry and the design of the cluster used in these calculations are discussed in §2.1 and §2.2, respectively.

2.1 Molecular Geometry

The molecular geometries used in GSCF3 calculations were determined with the commercial package Spartan '04[18] *ab initio* calculations at the 6-31G* level. The coordinate system is chosen such that the C-C-C chain is in the x-z plane with the global molecular axis parallel to the x axis. The y axis was then perpendicular to the

plane of C-C-C chains. The CH_2 groups are in the y-z plane. Figure 2 shows the geometry of the nonane molecule in the gas phase calculation.

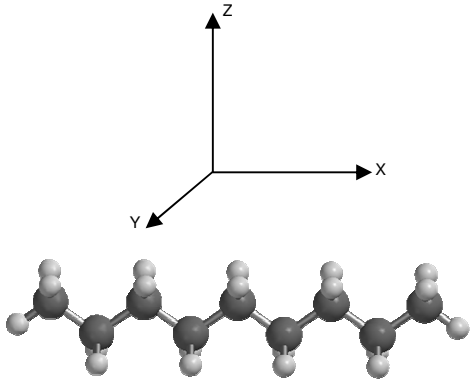

Figure 2 Molecular geometry of nonane used in GSCF3 calculation. The macromolecular axis is along x-axis with the C-C-C plane in the x-z plane. The H-C-H plane is perpendicular to the x-axis.

2.2 The design of the n-alkane clusters

It is known that, in the solid-state, the *n*-alkanes (C_nH_{2n+2}) in general adopt three structurally distinct groups: triclinic ($12 < n$ (even) < 26), orthorhombic (n (even) ≥ 36 and n (odd)), and monoclinic ($28 < n$ (even) ≤ 36).[19,20] An orthorhombic structure was used in constructing the alkane solid model, with the unit cell parameters[21] a = 7.48 Å, b = 4.97 Å, and $\theta = 48°$, as indicated in Figure 3.

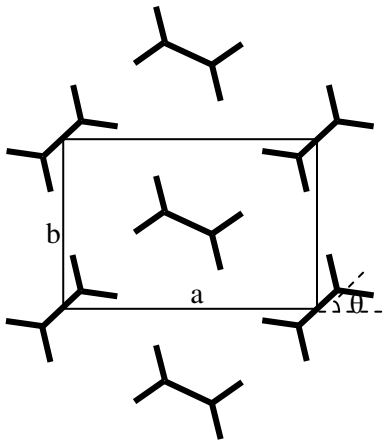

Figure 3 Top view of alkane cluster. This cluster is composed of seven molecules. The central Carbon atom of the central chain is calculated. This spatial arrangement is the same as in the *n*-alkane crystal.

The cluster radius must be greater than the radial extent of the optical orbitals, otherwise artificial states will be supported in the vacuum outside the cluster.[8] The number of molecules in each cluster (i.e. the size of the cluster) was chosen such that the radius of the first few excited states is within the cluster size, and that the cluster calculations are within the computer capability. The top view of the spatial arrangement (projection on the a-b plane in the unit cell) of alkane molecules in a cluster is shown in Figure 3.

The propane cluster is composed of seventeen propane molecules, with seven of them in the middle layer and five in the top and the bottom layers. The nonane cluster is composed of five nonane molecules and two pentane molecules. The side view of these two clusters is presented in Figure 4 left and right, respectively. These clusters should represent the intermolecular interaction (van der Waals forces) influencing the central carbon of the cluster (i.e. the central carbon of the central chain).

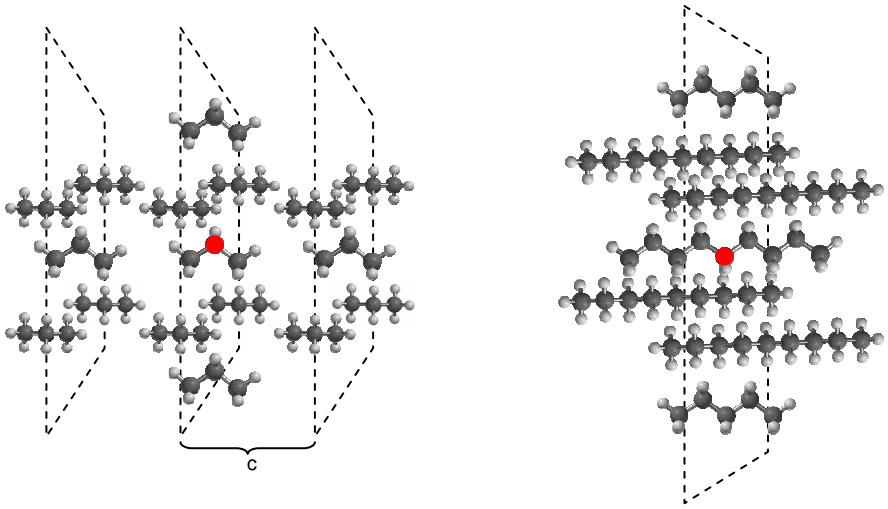

Figure 4 Side view of propane cluster (left), side view of nonane cluster (right). The dark balls represent carbon atoms and the white balls represent hydrogen atoms. The colored carbon is the calculated carbon in the GSCF3 calculations.

2.3 Selection of basis sets

In order to describe "valence" unoccupied molecular orbitals, a minimal basis set is used. To describe the excitation to the unoccupied orbitals (valence or Rydberg character) below the C 1s IP for n-alkanes, a basis set with more polarization function ("moderate" basis set) is used. This moderate basis set should be able to (a) accurately represent the possibility of excitation into diffuse Rydberg or Rydberg-like orbitals and (b) have no artificial Rydberg states that are generated from diffuse functions that extend beyond the model cluster; the latter is a balance between cluster diameter and basis set selection.

Minimal basis set calculations

A minimal basis set calculation is intended to isolate "valence" spectral features (e.g. of σ^* character) as this minimal basis set lacks the flexibility to support Rydberg transitions. In expanded basis set calculations, the calculation contains many transitions above the IP that can be considered as the artifacts of the extensive basis set. A minimal basis set is composed of a minimum number of basis functions required to represent all of the electrons on each atom, for example, only five functions, 1s, 2s, $2p_x$, $2p_y$, and $2p_z$, are needed to describe the electrons in a Carbon atom. Therefore, the number of occupied and unoccupied molecular orbitals is the same as the number of atomic orbitals. The character of each molecular orbital can be deduced from the atomic orbitals that contribute to this molecular orbital. A minimal basis set IVO calculation for the single nonane molecule is shown in Table 1. A contracted basis set of (73 6) for central carbon, (43 4) for other carbons, (6) for hydrogen atoms was used.

Moderate basis sets calculations

A minimal basis set IVO calculation only produces 'valence' spectral features as seen above. In order to represent the possibility of transitions to Rydberg-like orbitals below the IP, split basis functions, polarization functions, and diffuse functions are used. These split basis functions allow for the description of the aspherical atomic environments in molecules. The polarization functions allow the displacement of the orbital center from the nucleus position since the molecular orbitals are not totally symmetric. The diffuse functions are needed in order to describe the electron distribution at large distance from the atomic positions.

In our calculations, we used a *moderate basis set,* compared to the extensive basis set[22] used by Urquhart et al. for the isolated methane, ethane, propane, isobutene, and neopentane molecule. For the single nonane molecule (Table 2), the moderate basis set was (411121 3111) for central carbon, (621 41) for other carbons, (41) for hydrogen atoms. This basis set was expanded from the primitive basis set (73 6), (63 5), and (5), respectively. For the nonane cluster (Table 4) and propane cluster (Table 5) the same basis set as for the single nonane molecule was used for the central chain in the cluster. For other chains, an unexpanded basis set (43 4) for carbons atom and (4) for hydrogen atom was used. In order to account for the presence of a Rydberg state, polarization functions were applied to the core excited carbon atom. These polarization functions were ζ_d = 1.335 and 0.288, diffuse functions were ζ_p = 0.044, and ζ_s = 0.075 and 0.0253. This moderate basis set is capable of supporting Rydberg transitions, as justified below. This is slightly reduced relative to the "truncate" basis set used by Urquhart et al. for a propane molecule embedded in Ne atoms.[22]

2.4 'Shielding refined IVO' calculations

A core excited N-electron molecule can be considered as consisting of an 'active part' (the core hole and the excited optical electron) and a 'passive part' (the other N-1 electrons). In the IVO calculations, the excited (optical) orbitals are optimized in the potential of the passive cation. As the core $\rightarrow$ Rydberg transitions converge to a core-ionization threshold corresponding to the core-ionized (N-1) electron cation, this passive (N-1) electron part provides a good description of the electronic environment of these transitions. For core $\rightarrow$ valence transitions, the shielding effect of the excited electron on its valence optical orbital is not taken into account in the calculation of the passive (N-1) electron. As a result, the nucleus is overshielded and the calculated energy of valence transitions is shifted to higher energy. Therefore, in these IVO calculations, the energies of Rydberg states are generally more accurately calculated than valence state energies. The energy of Rydberg and valence excited states thus has a different systematic error, so predictions of the mixing between these states will be anomalous. This shielding effect can be corrected by recalculating the passive (N-1) part with the core hole vacancy and the optical orbital occupancy. The more accurately shielded passive (N-1) electron part is used in subsequent IVO calculations. This is also called 'shielding refined IVO' calculation.[23]

The 'shielding refined IVO' calculations were carried out on single nonane molecule (Table 3), nonane cluster (Table 4) and propane cluster (Table 5) with moderate basis sets.

3. Results

3.1 LD in NEXAFS valence features

Table 1 presents the calculated energies, term values, oscillator strengths, orbital size and the oscillator strength along the three Cartesian coordinates based on IVO *ab inito* calculations for a CH_2 group of an isolated nonane molecule with a minimal basis set. There are 28 unoccupied molecular orbitals. Only the orbitals with non-zero oscillator strength are listed in Table 1.

The IP calculated for the central CH_2 group of a single nonane molecule is 298.412 eV, far above the experimental C 1s IP of propane (290.7 eV as determined by X-ray photoelectron spectroscopy[24]), owing to the inflexibility of this basis set in reproducing relaxation following core excitation. As all core excited states have a small size (<2.0 Å), the absence of Rydberg character in a minimal basis set calculation is apparent. By examining molecular orbital plot and the atomic contribution for each excited state, those excited states composed of only carbon p_y orbitals and hydrogen 1s orbitals are of pure $\sigma^*_{C\text{-}H}$ character. While those excited states composed of carbon 2s and $2p_x$ atomic orbitals are of $\sigma^*_{C\text{-}C}$ character.

Table 1: Calculated Energies, Term Values, Oscillator Strengths, Orbital Size, and Oscillator strength along the x-, y-, and z- Cartesian coordinates based on IVO ab initio calculations for a CH_2 group of an isolated nonane molecule calculated with a minimal basis sets[a]

Ionization potential 298.41 eV							
Energy (eV)	TV[b]	Oscillator strength	Size (Å)	Orbital character	OS(x)	OS(y)	OS(z)
300.52	-2.11	0.0244	1.900	σ^*_{C-H}	0.0000	0.0000	**0.0244**
300.80	-2.39	0.0266	1.675	σ^*_{C-H}	0.0000	**0.0266**	0.0000
301.45	-3.04	0.0222	1.706	σ^*_{C-C}	**0.0222**	0.0000	0.0000
304.73	-6.32	0.0019	2.732	σ^*_{C-H}	0.0000	0.0000	**0.0019**
304.92	-6.51	0.0057	2.857	σ^*_{C-H}	0.0000	**0.0057**	0.0000
305.25	-6.84	0.0006	3.543	σ^*_{C-C}	**0.0006**	0.0000	0.0000
305.41	-7.00	0.0007	2.839	σ^*_{C-H}	0.0000	0.0000	**0.0007**
306.71	-8.30	0.0027	3.598	σ^*_{C-C}	**0.0027**	0.0000	0.0000
306.91	-8.50	0.0021	3.783	σ^*_{C-H}	0.0000	**0.0021**	0.0000
306.97	-8.56	0.0032	3.561	σ^*_{C-H}	0.0000	0.0000	**0.0032**
307.44	-9.03	0.0001	4.348	σ^*_{C-H}	0.0000	0.0000	**0.0001**
307.86	-9.45	0.0002	3.867	σ^*_{C-C}	**0.0002**	0.0000	0.0000
307.92	-9.61	0.0004	4.271	σ^*_{C-H}	0.0000	0.0000	**0.0004**
308.37	-9.96	0.0007	3.838	σ^*_{C-C}	**0.0007**	0.0000	0.0000
308.81	-10.4	0.0008	3.927	σ^*_{C-H}	0.0000	**0.0008**	0.0000
309.01	-10.6	0.0010	4.758	σ^*_{C-C}	**0.0010**	0.0000	0.0000
309.11	-10.7	0.0004	4.521	σ^*_{C-H}	0.0000	**0.0004**	0.0000
309.71	-11.3	0.0004	4.352	σ^*_{C-H}	0.0000	0.0000	**0.0004**
309.81	-11.4	0.0003	4.159	σ^*_{C-C}	**0.0003**	0.0000	0.0000
310.61	-12.2	0.0004	4.781	σ^*_{C-H}	0.0000	0.0000	**0.0004**
310.91	-12.5	0.0001	4.352	σ^*_{C-H}	0.0000	**0.0001**	0.0000

a. The minimal basis sets used in this calculation were: (73 6) for central carbon, (43 4) for other carbons, (6) for hydrogen atoms

b. Term Value (TV) = Ionization Potential – Energy

For the excitation to the σ^*_{C-H} valence orbitals, the calculated transition intensity – oscillator strength shows a strict orthogonality, either along the y-axis or along the z-axis, no contribution from the x-axis, indicating that the TDM of these σ^*_{C-H} valence transition is along the y- or z-axis, perpendicular to the macromolecular backbone.

For the excitation to σ^*_{C-C} valence orbitals, the oscillator strength only has contribution from x-axis, i.e these transitions are possible only along the macromolecular backbone. If the BB model were valid for the C 1s $\rightarrow \sigma^*_{C-C}$ transition, i.e. the TDM along the individual C-C bond, the transition intensity would have projection along the macromolecular backbone and perpendicular to the macromolecular backbone as well. However, our calculation shows the transition probability of C 1s $\rightarrow \sigma^*_{C-C}$ is along the macromolecular backbone. Therefore, the BB model is not supported theoretically, and the TDM of C 1s $\rightarrow \sigma^*_{C-C}$ is along the macromolecular backbone. The remaining features are much weaker compared to the above mentioned three features. It is hard to identify the character of these features.

Experimentally, three σ^*_{C-C} features are identified in the continuum of the NEXAFS spectra of n-alkanes.[14] In this minimal basis set IVO calculation, three strong features are revealed in the continuum in which two are pure σ^*_{C-H} character and one σ^*_{C-C} character. This experimental and theoretically inconsistency is interesting. Further investigation is needed.

3.2 LD in NEXAFS features below the IP

3.2.1 Justification for moderate basis set

Table 2 presents the calculated energies, term values, oscillator strengths, orbital size, and singlet-triplet separation based on IVO ab inito calculations for a CH_2 group of an isolated nonane molecule with a moderate basis set.

Table 2: Calculated Energies, Term Values, Oscillator Strengths, Orbital Size, and singlet-triplet separation based on IVO ab initio calculations for a CH_2 group of an isolated nonane molecule calculated with a moderate basis set.[a]

Ionization potential 290.288 eV						
Energy (eV)	TV[b]	Oscillator strength	Size (Å)	Orbital character		ΔE(S-T) (eV)
				Major	Minor	
288.05	2.24	0.0020	3.598	3s	$3p_x/3p_z$	0.115
288.90	1.39	0.0040	3.248	$3p_y$	3s	0.095
289.07	1.22	0.0006	3.412	$3p_z$	3s	0.031
290.07	0.22	0.0003	3.594	$3p_x$	$3s/3p_z$	0.006

a. The basis sets used in this calculation were: basis set: (411121 3111) for central carbon, (621 41) for other carbons, (41) for hydrogen atoms. The polarization functions were ζ_d = 1.335 and 0.288, and diffuse functions ζ_p = 0.0440, ζ_s = 0.075, and 0.0253.
b. Term Value (TV) = Ionization Potential – Energy

The calculated C1s IP with this moderate basis set is 290.288 eV, which is close to the experimental value of 290.7 eV of propane.[24] This moderate basis set IVO calculation reveals four excited states below the C 1s IP. These orbitals have larger orbital size (>3 Å) and weaker oscillator strength, indicating that these resonances have Rydberg character. The singlet-triplet energy difference for the first two core excited states, 0.115 eV and 0.095 eV, respectively, implies some valence character, which is consistent with a recent study of gaseous *n*-alkanes, where a small degree of $\sigma^*_{C\text{-}H}$ valence character contributes to Rydberg dominant excited states that have appropriate symmetry.[22] The remaining two excited states exhibit large orbital size, small singlet – triplet separation, indicating they are of Rydberg character. This moderate basis set is

thus adequate for describing Rydberg core excited states. Thus validated, we will use this moderate basis set to describe Rydberg character in condensed phase cluster calculations, below.

3.2.2 Character of each NEXAFS feature below the IP

A Rydberg orbital can be identified by its large radius, weak oscillator strength, and a small difference between its singlet and triplet excitation energy. At the carbon 1s edge, Rydberg core excited states have a radius greater than ~3 – 4 Å, for small and larger molecules, respectively. The oscillator strength is usually less than 0.01 for Rydberg transitions. A state with a singlet-triplet energy difference less than 0.05 eV is usually considered to be a Rydberg state.[23]

Table 3 presents the results of 'shielding refined IVO' calculations performed for the central carbon atom in a single nonane molecule. A comparison of Table 2 (regular IVO) and Table 3 ('shielding refined IVO') reveals an enhancement of the valence character in the first two excited states in gas phase nonane. The size of the optical orbital decreased by 0.121 Å and 0.063 Å, respectively, for the first two excited states from the calculations without shielding, and the singlet-triplet separation increased by 0.057 eV and 0.033 eV, respectively. This indicates that the first two transitions have significant valence character and that the estimation of this valence character improves when Rydberg – valence mixing is more accurately considered. For the remaining two excited states, the orbital size did not change substantially and the singlet-triplet separation remains less than 0.05 eV, indicating that these core excited states have predominant Rydberg character.

Table 3: Calculated Energies, Term Values, Oscillator Strengths, Orbital Size, and singlet-triplet separation based on 'shielding refined IVO' calculations for a central CH_2 group of an isolated nonane molecule.[a]

	Energy (eV)	TV[b] (eV)	IP[c] (eV)	Oscillator strength	Size (Å)	Orbital character		ΔE(S-T) (eV)
						Major	Minor	
CH_2	287.92	2.60	290.52	0.0028	3.477	3s	$3p_z$	0.172
	288.77	1.71	290.48	0.0052	3.185	$3p_y$	3s	0.128
	288.93	1.48	290.41	0.0003	3.421	$3p_z$	3s	0.016
	289.97	0.44	290.41	0.0004	3.544	$3p_x$	3s	0.007

a. The basis sets used in this calculation were: (411121 3111) for central carbon, (621 41) for other carbons, (41) for hydrogen atoms. The polarization functions were ζ_d = 1.335 and 0.288, and diffuse functions ζ_p = 0.0440, ζ_s = 0.075 and 0.0253.
b. Term Value = Ionization Potential – Energy
c. Ionization potential is calculated based on ΔSCF method, where the energy difference is between the ground state molecule and core-excited cation, where the (N- 1) electron component has been calculated with the screening for the excited electron in the optical orbital.

Table 4: Calculated Energies, Term Values, Oscillator Strengths, Orbital Size, and singlet-triplet separation based on 'shielding refined IVO' calculations for a central CH_2 group of a nonane cluster.[a]

	Energy (eV)	TV[b] (eV)	IP[c] (eV)	Oscillator Strength	Size (Å)	Orbital character		ΔE(S-T) (eV)
						Major	Minor	
CH_2	289.07	2.96	292.03	0.0076	2.738	3s	$3p_{x, y, z}$	0.402
	289.86	2.19	292.04	0.0114	2.684	3s	$3p_{x, y, z}$	0.369
	290.41	1.21	291.62	0.0001	3.034	3s / $3p_z$	$3p_{x, y}$	0.003
	290.97	0.48	291.45	0.0008	3.320	$3p_x$	3s	0.019

a. The basis sets used in this calculation were: (411121 3111) for central carbon of central chain, (621 41) for other carbons of central chain, (41) for hydrogen atoms of central chain, (43 4) for carbons in other chains, (4) for hydrogen atom in other chains. The polarization functions were ζ_d = 1.335 and 0.288, and diffuse functions ζ_p = 0.0440, ζ_s = 0.075 and 0.0253.
b. Term Value (TV) = Ionization Potential – Energy
c. Ionization potential is calculated based on ΔSCF method, where the energy

difference is between the ground state molecule and core-excited cation, where the (N- 1) electron component has been calculated with the screening for the excited electron in the optical orbital.

The results of 'shielding refined IVO' calculations of a single nonane molecule and a nonane cluster are presented in Table 3 and Table 4. Upon condensation, all transitions have a "blue shift" relative to corresponding values for the single nonane molecule, consistent with experimental results and previous theoretical calculations.[8] Molecular orbital size for the first two excited states shows a significant change from the gas phase to solid phase (3.477 Å (g) to 2.738 Å (s), 3.185 Å (g) to 2.684 Å (s)). For the remaining two core excited states, a large change is not observed. A greater singlet-triplet energy separation is also observed for the first two core excited states, increasing from 0.172 and 0.128 eV to 0.402 and 0.369 eV, respectively. This indicates that the first two core excited states are dominated by valence character and the second two are of Rydberg character in the condensed phase of *n*-alkanes.

In order to estimate the effect of the end CH_3 groups on the electronic structure of the central CH_2 groups, Table 4 and Table 5 compare the excitation energy, orbital size, oscillator strength, and singlet-triplet separation from 'shielding refined IVO' calculations of the nonane and propane clusters. A red shift is observed in the propane cluster due to the presence of methyl groups near the methylene core in propane. A larger orbital size and smaller singlet-triplet separation is observed in the propane cluster. The first two excited states have greater valence character in the nonane cluster. The relative strength of the first two transitions is 1 : 2.27 for propane, and 1 : 1.50 for nonane, respectively. It is expected as the chain becomes longer; the relative intensity of these two features would become equal. We have seen experimentally that

in the NEXAFS spectra of tetracontane,[25] these two peaks have almost identical intensity.

Table 5: Calculated Energies, Term Values, Oscillator Strengths, Orbital Size, and singlet-triplet separation based on 'shielding refined IVO' calculations for a central CH_2 group of a propane cluster.[a]

	Energy (eV)	TV[b] (eV)	IP[c] (eV)	oscillator strength	Size (Å)	Orbital character		ΔE(S-T) (eV)
						Major	Minor	
CH_2	288.93	3.02	291.94	0.0049	3.026	3s	$3p_{x, y, z}$	0.367
	289.79	2.20	291.99	0.0111	2.859	3s	$3p_{x, y, z}$	0.332
	290.16	1.41	291.58	0.0001	3.401	$3p_x$	$3s / 3p_{y, z}$	0.001
	290.40	1.24	291.64	0.0002	3.205	$3p_z / 3s$	$3p_{x, y}$	0.031

a. The basis sets used in this calculation were: (411121 3111) for central carbon of central chain, (621 41) for other carbons of central chain, (41) for hydrogen atoms of central chain, (43 4) for carbons in other chains, (4) for hydrogen atom in other chains. The polarization functions were ζ_d = 1.335 and 0.288, and diffuse functions ζ_p = 0.0440, ζ_s = 0.075 and 0.0253.
b. Term Value (TV) = Ionization Potential – Energy
c. IP is calculated based on ΔSCF method, where the energy difference is between the ground state molecule and core-excited cation, where the (N-1) electron component has been calculated with the screening for the excited electron in the optical orbital.

From these results, we conclude that the first two core excited states have a greater valence character in the condensed phase. In contrast, due to the relatively large molecular orbital size and smaller singlet-triplet energy separation (< 0.05 eV), the remaining two core excited states have retained their Rydberg character in the condensed phase. This can be understood by considering the distribution of oscillator strength for each excited state along the x-, y-, and z-axis.

The contribution of the oscillator strength along the x-, y-, and z- axes of a single nonane molecule and cluster has been calculated and tabulated in Table 6. For the single molecule and cluster model, the first two core excited states have oscillator

strengths oriented in the y- and z- axes, e.g. in the C-H plane. It is therefore possible for the valence (σ^*_{C-H}) and Rydberg states to mix.[22] The cluster shows some mixing in the yz plane. Therefore, in the gas phase, these two peaks are dominated by Rydberg character, while in the condensed phase, the Rydberg character has been quenched and these two peaks are dominated by valence character. The fourth excited state in the nonane cluster (the third in the propane cluster) only has a contribution along the x-axis (perpendicular to the C-H plane), therefore, there is no way for the valence and Rydberg to mix, i.e. the fourth excited state of nonane cluster (the third of propane cluster) is of pure Rydberg character in the gas and condensed phases.

Table 6: Calculated oscillator strength distributed along the x-, y- and z- direction for propane and nonane cluster.

		OS(x)	OS(y)	OS(z)
Nonane single molecule with moderate basis sets	LUMO	0.0000	0.0000	**0.0020**
	LUMO+1	0.0000	**0.0040**	0.0000
	LUMO+2	0.0000	0.0000	0.0006
	LUMO+3	0.0003	0.0000	0.0000
Nonane single molecule with 'shielding refined IVO' calculation	LUMO	0.0000	0.0000	**0.0028**
	LUMO+1	0.0000	**0.0052**	0.0000
	LUMO+2	0.0000	0.0000	**0.0003**
	LUMO+3	**0.0004**	0.0000	0.0000
Propane cluster	LUMO	0.0000	0.0013	**0.0035**
	LUMO+1	0.0000	**0.0108**	0.0004
	LUMO+2	**0.0001**	0.0000	0.0000
	LUMO+3	0.0000	0.0000	**0.0002**
Nonane cluster	LUMO	0.0000	0.0027	**0.0049**
	LUMO+1	0.0000	**0.0102**	0.0013
	LUMO+2	0.0000	0.0000	0.0001
	LUMO+3	0.0008	0.0000	0.0000

3.2.3 LD for the NEXAFS features below the C 1s IP for n-alkanes

In the above calculations, the first two transitions in the nonane cluster and propane cluster are oriented in the CH_2 plane (yz plane) and perpendicular to the

macromolar axis (x-axis). They are dominated by the C 1s $\rightarrow \sigma^*_{C\text{-}H}$ transitions in the condensed phase. In the angular dependent NEXAFS spectra,[14] the first two transitions exhibit strong angular dependence with maximum intensity at $\theta = 90°$ (***E*** vector perpendicular to the macromolecular backbone) and near-zero intensity at $\theta = 0°$ (***E*** vector parallel to the macromolecular backbone). Therefore, the TDMs of these first two transitions are perpendicular to the macromolecular axis. However, a recent observed dichroism in the C 1s $\rightarrow \sigma^*_{C\text{-}H}$ transitions of single crystals of *n*-tetracontane reveals that the TDM of these two transitions are along a- and b- axis of the orthorhombic unit cell of the n-tetracontane crystal.[25]

The third transition in the propane cluster (the fourth in the nonane cluster) only exhibits intensity along the macromolecular backbone (z-axis) and no absorption in the CH_2 plane (yz plane). This transition is of Rydberg character as analyzed before. In the angular dependent NEXAFS spectra,[14] the third transition exhibits the same angular dependence as the C 1s $\rightarrow \sigma^*_{C\text{-}C}$ transition, therefore, the TDM of this transition is along the macromolecular backbone.

4. Conclusion

We have examined the linear dichroism for the NEXAFS resonances of n-alkanes by carrying out ab initio theoretical calculations on an isolated nonane molecule, a nonane cluster, and a propane cluster. For the NEXAFS resonances above the C 1s IP, we found that the transition dipole moment of C 1s $\rightarrow \sigma^*_{C\text{-}C}$ transition is along the macromolecular backbone. For the NEXAFS resonances below the C 1s IP, when the intermolecular interaction in the condensed phase n-alkanes is considered, for the features oriented in the CH_2 plane the Rydberg transition is most likely to be quenched

and the valence character is dominant. The TDM of these valence features is in the CH_2 plane, perpendicular to the macromolecular axis. However, for the feature along the macromolecular backbone, there is no valence character. This is a pure Rydberg transition with its TDM along the macromolecular axis.

References:

(1) Outka, D. A.; Stöhr, J.; Rabe, J. P.; Swalen, J. D.; Rotermund, H. H. *Physical Review Letters* **1987**, *59*, 1321.

(2) Hähner, G.; Kinzler, M.; Wöll, C.; Grunze, M.; Scheller, M. K.; Cederbaum, L. S. *Physical Review Letters* **1991**, *67*, 851.

(3) Kinzler, M.; Schertel, A.; Hähner, G.; Wöll, C.; Grunze, M.; Albrecht, H.; Holzhüter, G.; Gerber, T. *Journal of Chemical Physics* **1994**, *100*, 7722.

(4) Hitchcock, A. P.; Newbury, D. C.; Ishii, I.; Stohr, J.; Horsley, J. A.; Redwing, R. D.; Johnson, A. L.; Sette, F. *Journal of Chemical Physics* **1986**, *85*, 4849.

(5) Stöhr, J.; Outka, D. A.; Baberschke, K.; Arvanitis, D.; Horsley, J. A. *Physical Review B* **1987**, *36*, 2976.

(6) Bagus, P. S.; Weiss, K.; Schertel, A.; Wöll, C.; Braun, W.; Hellwig, C.; Jung, C. *Chemical Physics Letters* **1996**, *248*, 129.

(7) Weiss, K.; Bagus, P. S.; Wöll, C. *Journal of Chemical Physics* **1999**, *111*, 6834.

(8) Urquhart, S. G.; Gillies, R. *Journal of Chemical Physics* **2006**, *124*, 234704.

(9) Ade, H.; Urquhart, S. G. NEXAFS spectroscopy and microscopy of natural and synthetic polymers. In *Chemical Applications of Synchrotron Radiation*; Sham, T.-K., Ed.; World Scientific Publishing Co. Pte. Ltd.: Singapore, 2002; pp 285.

(10) Hitchcock, A. P.; Brion, C. E.; Van der Wiel, M. J. *Journal of Physics B: Atom. Molec. Phys.* **1978**, *11*, 3245.

(11) Dehmer, J. L. *The Journal of Chemical Physics* **1972**, *56*, 4496.

(12) Piancastelli, M. N. *Journal of Electron Spectroscopy and Related Phenomena* **1999**, *100*, 167.

(13) Stöhr, J.; Outka, D. A. *Physical Review B* **1987**, *36*, 7891.

(14) Fu, J.; Urquhart, S. G. *Journal of physical Chemistry A* **2005**, *109*, 11724.

(15) Kosugi, N.; Kuroda, H. *Chemical Physics Letters* **1980**, *74*, 490.

(16) Hunt, W. J.; Goddard, W. A. *Chemical Physics Letters* **1969**, *3*, 414.

(17) Huzinaga, S.; Andzelm, J.; Klobukowski, M.; Radzio-Andzelm, E.; Sasaki, Y.; Tatewaki, H. *Gaussian basis sets for molecular orbital calculations*; Elsevier: Armsterdam, The Netherlands, 1984.

(18) Spartan'04 windows; 1.0.1 ed.; Wavefunction, Inc.: Irvine, 2004.

(19) Hastie, G. P.; Johnstone, J.; Roberts, K. J.; Fischer, D. *Journal of the Chemical Society-Faraday Transactions* **1996**, *92*, 783.

(20) Nyburg, S. C.; Potworowski, J. A. *Acta Crystallographica* **1973**, *B29*, 347.

(21) Smith, A. P. *Journal of Chemical Physics* **1953**, *21*, 2229.

(22) Urquhart, S. G.; Gillies, R. *Journal of physical Chemistry A* **2005**, *109*, 2151.

(23) Kosugi, N. *"Advanced course in application of GSCF3 to inner-shell excitation"* **2000**.

(24) Siegbahn, K.; Nordling, C.; Johansson, G.; Hedman, J.; Heden, P. F.; Hamrin, K.; Gelius, U.; Bergmark, T.; Werme, L. O.; Manne, R.; Baer, Y. *ESCA applied to free molecules*; Amsterdam, North-Holland Pub. Co., 1969.

(25) Zou, Y.; Araki, T.; Appel, G.; Kilcoyne, A. D. L.; Ade, H. *Chemical Physics Letters* **2006**, *Submitted*.

3.5 Morphology and molecular orientation change as a function of n-alkane chain length and substrate temperature

This section documents the effects of *n*-alkane chain length and substrate temperature on the growth of linear alkane thin films onto cleaved NaCl (001) surface. This work is in preparation and presented here in its manuscript form.

The author of this thesis prepared these samples, acquired the NEXAFS spectra, was a major contributor in establishing the discussion, and prepared the manuscript in close collaboration with Dr. Urquhart.

The author of this thesis obtained Dr. Urquhart's agreement to present the work in this thesis.

Effect of Chain Length and Substrate Temperature on the Growth and Morphology of n-Alkane Thin Films

*Juxia Fu and Stephen G. Urquhart**

Department of Chemistry, University of Saskatchewan, 110 Science Pl, Saskatoon, Saskatchewan, Canada S7N 5C9

NEXAFS spectroscopy and microscopy has been used to study the orientational morphology of thin films of the linear alkanes n-$C_{36}H_{74}$ and n-$C_{60}H_{122}$, prepared by vacuum deposition onto NaCl(001) surfaces at ambient and elevated substrate temperatures. The orientational morphology, specifically the nature of domains with lateral and normal orientation, is explored as a function of the chain length and the substrate temperature. It is found that the longer n-$C_{60}H_{122}$ molecules are laterally oriented on the substrate surface within the investigated substrate temperatures, but the morphology of these oriented domains varies with temperature. The shorter n-$C_{36}H_{74}$ molecules are only partially laterally oriented at low substrate temperature and completely normally oriented at high substrate temperature. The formation of complex, nanoscale orientational morphologies are rationalized by kinetic and thermodynamic considerations, in particular the relative enthalpic and entropic contributions to the free energy associated with the different molecular orientations.

Submitted to Langmuir on October 12, 2006
*Corresponding author: email Stephen.urquhart@usask.ca

1. Introduction

Organic thin films are of great interest because of their potential applications in the field of molecular electronics, optics and sensors.[1,2] The properties of these devices are closely related to the structural order, orientation and morphology of the molecules in the thin films. Understanding the mechanisms of the growth of organic thin films, developing methods to control the resultant morphology and to characterize this orientational nanostructure is essential for developing these technologies.

Alkanes are simple organic molecules. They play important roles in the formation of ordered structures in molecular assemblies such as Langmuir-Blodgett films, self-assembled monolayers, and liquid crystals. Therefore, knowledge of the structure of alkane films should be useful for understanding and controlling the morphology and molecular orientation in functional thin films.

The structure of linear alkane thin films has been investigated by a variety of techniques, such as electron microscopy and electron diffraction,[3-5] X-ray diffraction,[6-9] atomic force microscopy (AFM),[10,11] infrared transmission and reflection-absorption spectroscopies,[12,13] and Near edge X-ray absorption fine structure (NEXAFS) spectroscopy and microscopy.[14,15]

Here, NEXAFS spectroscopy and microscopy is explored and developed as a complementary means to characterize the morphology and orientation in these thin films. NEXAFS spectroscopy uses synchrotron radiation, which is tunable and highly polarized. In NEXAFS spectroscopy, X-rays are absorbed when a core-level electron is excited to an unoccupied molecular orbital that is specific to the molecule's electronic

structure; therefore, NEXAFS spectroscopy can be used to identify the element species and functional groups in the sample.[16-18]

Linear dichroism in NEXAFS spectroscopy and microscopy can be used to investigate molecular orientation. For example, the linear dichroism in NEXAFS microscopy was demonstrated for Kevlar fiber,[19] where the butterfly-like patterns change with rotation of the electric field vector of X-rays. These butterfly-like patterns are consistent with the expected radically symmetric structure of the fiber. Linear dichroism in NEXAFS spectroscopy has been demonstrated in species such as crystalline polymers,[20] self-assembled monolayers,[21] and Langmuir-Blodgett films.[22,23]

In NEXAFS spectroscopy, the intensity of a specific NEXAFS transition depends on the angle (θ) between the electric field vector of linearly polarized X-rays and the transition dipole moment (TDM, μ_{if}) of that transition according to

$$I \propto \left| E \cdot \mu_{if} \right|^2 \propto \cos^2 \theta \qquad (1)$$

where μ_{if} is the TDM for the one electron transition from the initial state ψ_i to the final state ψ_f according to:

$$\mu_{if} = \left\langle \psi_f \left| \mu \right| \psi_i \right\rangle \qquad (2)$$

where μ is the electric dipole operator.

This effect is illustrated in Figure 1 for the linear dichroism of an oriented linear alkane chain.[24,25] When the X-ray's electric field vector is oriented perpendicular to the molecular backbone (e.g. Figure 1b), this vector is parallel to the TDM for the $\sigma^*_{C\text{-}H}$ molecular orbital, and therefore the Carbon 1s $\rightarrow \sigma^*_{C\text{-}H}$ transitions at ~288 eV have their maximum intensity. Figure 1(c) demonstrates the contrasting situation, where the

X-ray electric field vector is oriented parallel to the macromolecular backbone, i.e. this vector is parallel to the TDM of Carbon 1s $\rightarrow \sigma^*_{C\text{-}C}$ transition, therefore, the Carbon 1s $\rightarrow \sigma^*_{C\text{-}C}$ transition (~293 eV) has maximum intensity and the intensity of the Carbon 1s $\rightarrow \sigma^*_{C\text{-}H}$ transition reaches a minimum. The linear dichroism in alkanes has been recently studied by our group,[25] in which we showed that the pseudo-diatomic building block model used by many groups[26,27] provides an inaccurate measurement of the orientation of alkyl molecules.

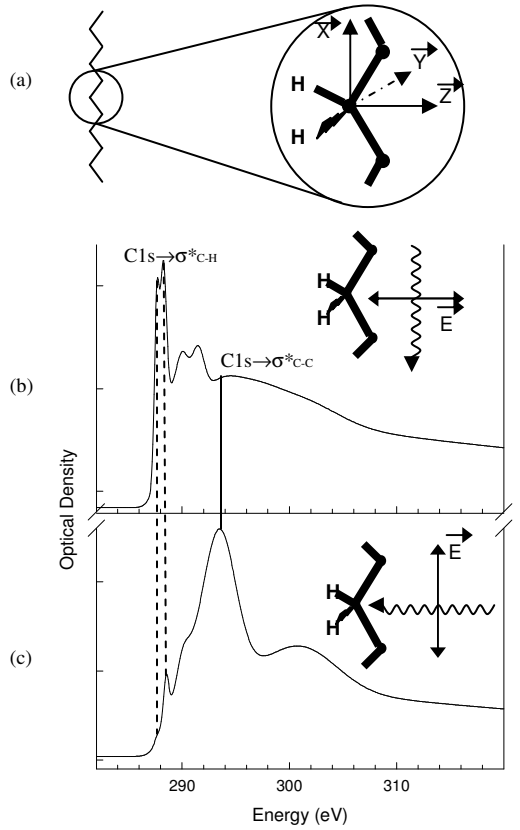

Figure 1 (a) Schematic of a linear alkane chain and an enlarged view of the geometry of a carbon atom in the chain. The x-axis is the macroscopic chain direction and C-H bonds are located in the z-y plane. (b) When $\vec{E} \perp$ x-axis, the maximum intensity occurs at the Carbon 1s$\rightarrow\sigma^*_{C\text{-}H}$ transitions; (c) When $\vec{E}$// x-axis, the maximum intensity occurs at the Carbon 1s$\rightarrow\sigma^*_{C\text{-}C}$ transitions. $\vec{E}$ is the electric field vector of X-rays. This figure is derived from Figure 2 in ref [24].

This linear dichroism allows us to determine the orientation of alkane molecules in these thin films. When the alkane chains are oriented normal to the sample surface, the X-ray absorption spectrum will be characterized by a strong Carbon 1s $\rightarrow \sigma^*_{C\text{-}H}$ transition and a weak Carbon 1s $\rightarrow \sigma^*_{C\text{-}C}$ transition (cf. Figure 1b). When the alkane chains are laterally oriented within the plane of the surface, the orientation in this plane can be determined as shown schematically in Figure 2, where the intensity of the Carbon 1s $\rightarrow \sigma^*_{C\text{-}H}$ transition and the Carbon 1s $\rightarrow \sigma^*_{C\text{-}C}$ transition depends on the orientation of the molecule relative to the photon polarization vector.

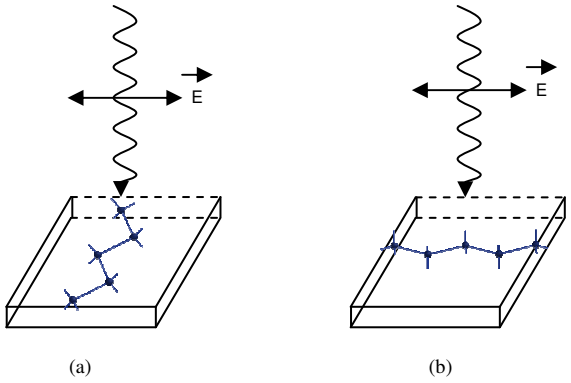

Figure 2 Relative spatial arrangements of linear alkane molecules (laterally oriented along the substrate surface) with respect to electric field vector of X-rays, $\vec{E}$. (a) Electric field vector perpendicular to macromolecular backbone; (b) Electric field vector parallel to macromolecular backbone.

Ordered linear alkane thin films can be prepared by epitaxy,[28,29] which refers to a system where there is a well-defined orientational relationship between the film and substrate. Epitaxy in linear alkane thin films has been known since 1956.[30] Unlike atomic epitaxy, molecular orientation is an important variable, as will be outlined below. In molecular epitaxy, lattice mismatch is generally less important. For example, the epitaxial crystallization of polyethylene was observed on cleaved (001) surfaces of

NaCl, NaBr, NaI, KCl, KI, and LiF with the corresponding lattice mismatching ranging from -28% to 27%.[31] This epitaxy arises from the high symmetry and the ionic field force of the ionic substrate, inducing the molecules to align along the substrate surface.

Figure 3 presents a diagram of the epitaxial growth of a linear alkane on a NaCl (001) surface, where alkane chains are laterally-oriented on substrate surface along the <110> and <$\bar{1}$10> directions. This is consistent with theoretical calculations[32,33] and previous experimental results.[4,5]

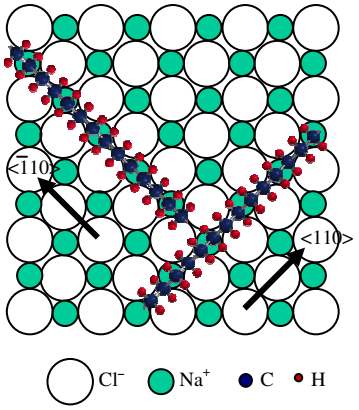

Figure 3 Epitaxial relationships between linear alkane molecules and NaCl (001) face. The alkane chains are oriented laterally on the substrate surface with their c-axis along the <$\bar{1}$10> and <110> directions of the substrate.

The structure of linear alkane thin films is variable. For example, the morphology of an ultrathin film of hexacontane (n-$C_{60}H_{122}$) prepared by spin casting onto graphite was examined by atomic force microscopy, revealing a lamellar morphology of laterally oriented alkane chains.[11] In contrast, raft-like structures have been found for hexatriacontane (n-$C_{36}H_{74}$) thin films grown on cleaved NaCl and KCl surfaces, as examined by scanning electron microscopy.[4] The morphology and molecular orientation of the linear alkane thin films is greatly affected by the deposition conditions such as substrate temperature[5,34,35] and deposition rate[36] as well as the length

of the molecular chain.[36-38] For example, pentacontane (*n*-$C_{50}H_{102}$) molecules are laterally oriented when evaporated onto fused-quartz substrate at lower substrate temperature (T_s = 134 K), while at higher substrate temperature (T_s = 335 K) all *n*-$C_{50}H_{102}$ molecules become normally oriented. At intermediate substrate temperature, both lateral orientation and normal orientation are found.[39] For the shorter tetracontane (*n*-$C_{40}H_{82}$), the normal orientation occurred at a lower substrate temperature (T_s = 325 K) than that for longer pentacontane.[39]

In this paper, we present results of an X-ray spectroscopy and microscopy study of the orientational morphology of thin films of linear alkanes. A wide range of morphologies are observed in these thin films. The orientation of the alkane molecules in thin films is also found to vary with chain length and the substrate temperature during deposition. These observations are rationalized by consideration of the kinetics and thermodynamics of film nucleation and growth.

2. Experimental section

Sample preparation

The linear alkanes used in this study are n-hexacontane (n-$C_{60}H_{122}$, **HC**) (Sigma-Aldrich, 98%) and n-hexatriacontane (n-$C_{36}H_{74}$, **HTC**) (Sigma-Aldrich, 98%), used without purification. NaCl surfaces were prepared by cleaving a NaCl single crystal to expose a fresh (001) crystal plane. The alkane sublimation was carried out under a vacuum of ~10^{-7} torr from a resistively heated tungsten boat. The average thickness of the deposited films was controlled to be around 100~150 nm with a quartz crystal microbalance. During deposition, the NaCl substrates were heated with a quartz halogen light bulb mounted beneath the sample holder and the substrate temperature

was monitored with a thermocouple. After deposition, the NaCl substrate was dissolved in millipore water and the floating alkane thin films were picked up by Si_3N_4 membranes windows [Silson Ltd.] for the X-ray microscopy experiment.

In order to explore the effects of chain length on the molecular orientation and thin film morphology of linear alkanes, **HC** and **HTC** thin films were prepared in vacuum on an unheated cleaved NaCl (001) surface (T_s = RT). The effects of substrate temperature were examined on **HC** and **HTC** thin films prepared on cleaved NaCl (001) surfaces at elevated substrate temperature. For **HC** thin films, the substrate temperatures are: T_s = RT, 36°C, 40°C, 45°C, 48°C, and 60°C. For **HTC** thin films, the substrate temperatures are: T_s = RT and 40°C.

Data Acquisition

NEXAFS images and spectra were recorded at the Advanced Light Source in Berkeley on two different Scanning Transmission X-ray Microscopes (STXM): the Polymer-STXM (beamline 5.3.2)[40] and the Molecular Environmental Sciences STXM (beamline 11.0.2).[41] All spectra were acquired in transmission mode and are reported as optical density versus energy. Using STXM microscopes, X-ray absorption images can be obtained at a spatial resolution below 35 nm, depending on the zone plate. The X-ray absorption spectrum can be obtained from sub-micron scale domains.[42]

At the carbon 1s edge, the energy calibration is performed by introducing CO_2 into the microscope chamber while the sample is in place, allowing the spectrum of the sample and the calibrated CO_2 to be recorded simultaneously. The two absorption peaks in CO_2 corresponding to the C 1s → 3s (ν = 0) (292.74 eV) and C 1s → 3p (ν = 0) (294.96 eV) are used for calibration.[43]

3. Results and Discussion

3.1 Analysis of STXM data

As introduced in section 1, NEXAFS spectroscopy and microscopy can be used to obtain information about thin film morphology and molecular orientation of linear alkanes. This section focuses on how to extract such information, using the sample of **HC** prepared on cleaved NaCl surface at room temperature.

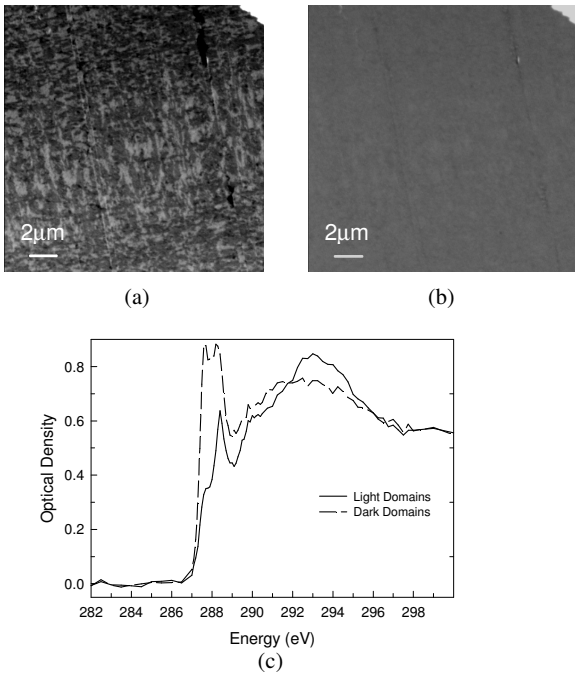

Figure 4 (a) X-ray absorption image at 287.6 eV (at which C 1s $\rightarrow \sigma^*_{C\text{-}H}$ transitions occur) of **HC** films, thermally evaporated on NaCl (001) face at T_s = RT. (b) X-ray absorption image at 330 eV (at which no specific transitions for alkane samples occur). (c) NEXAFS spectra correspond to the image contrast in image (a). The optical density for these two spectra at 330 eV is identical (OD=0.35), indicating this sample is uniform.

Figure 4(a) and (b) presents X-ray microscopy images, recorded at 287.6 eV for (a) and 330.0 eV for (b), of an **HC** thin film (120 nm) deposited onto a cleaved NaCl (001) substrate at T_s = RT. Figure 4(c) presents extracted Carbon 1s NEXAFS spectra from the dark and light domains observed in Figure 4(a). The resonances observed at

287.6 eV and 288.2 eV have been previously assigned as Carbon 1s $\rightarrow \sigma^*_{C\text{-}H}$ transitions, and the broad resonance at 293.5 eV as a Carbon 1s $\rightarrow \sigma^*_{C\text{-}C}$ transition.[44,45]

Strong image contrast is observed in Figure 4(a), recorded at the energy of a Carbon 1s $\rightarrow \sigma^*_{C\text{-}H}$ transition, while there is no contrast in Figure 4(b), recorded at an energy in the post-edge continuum. The origin of the X-ray microscopy image contrast is shown in equation 3:

$$I = I_0 \exp(-\mu \cdot \rho \cdot t) \qquad (3)$$

where I is transmitted intensity, I_0 is the incident photon flux intensity, t is sample thickness, μ is the mass absorption coefficient, and ρ is the density. The X-ray images are a measure of the X-ray transmission (spatial variation in I at a fixed value of I_o). The X-ray absorption spectra are presented on an optical density scale that is defined as

$$OD = -\ln(I / I_0) = \mu \cdot \rho \cdot t \qquad (4)$$

The image contrast in Figure 4(a) can arise from either the presence of different chemical components or molecular orientation (reflected in the mass absorption coefficient, μ) or from differences in sample thickness (t) or density (ρ). Given the purity of **HC** (98%) and the possibility of distillation-purification during evaporation in vacuum, the presence of other chemical species can be excluded.

Whether this image contrast is caused by molecular orientation, sample thickness difference or both can be resolved by examining an X-ray microscopy image recorded at energies where no spectroscopic features are present. In the post-edge region (above 315 eV for n-alkanes), no absorption features are present and the mass absorption coefficient (μ) reflects the atomic photoionization cross-section. Therefore, the optical density (Eq. 4) in the post-edge is proportional to the product of the sample's density

and thickness, and is independent of molecular orientation. Because of the similarity of the post-edge region in Figure 4(c) (above 315 eV), and the lack of image contrast in Figure 4(b) (recorded at 330 eV), we conclude that the **HC** films have uniform thickness and density and the image contrast in Figure 4(a) can be entirely attributed to *different molecular orientations* present in the thin film (i.e. the variation in μ with molecular orientation). The intensity of the Carbon 1s $\rightarrow \sigma^*_{C\text{-}H}$ transitions varies with orientation, indicating that this sample is well ordered and **HC** molecules are laterally oriented on the sample surface, (cf. Figure 1 and Figure 2), orthogonally as shown in Figure 3. Thus, NEXAFS spectroscopy provides a direct method to determine the molecular orientation at the sub-micron scale.

3.2. Morphology and Orientation of Linear Alkane Thin Films as a Function of Chain Length

Thin films of linear alkanes n-Hexacontane (n-$C_{60}H_{122}$, **HC**) and n-Hexatriacontane (n-$C_{36}H_{74}$, **HTC**) were deposited onto an unheated (e.g. room temperature T_s = RT (22 ± 1 °C)) NaCl (001) surface.

As discussed in section 3.1, the **HC** thin films (Figure 4) prepared on cleaved NaCl surfaces at T_s = RT have a uniform thickness. The **HC** molecules are oriented laterally on the NaCl (001) surface along two crystallographic equivalent directions.

Figure 5(a) presents an X-ray microscopy image recorded at 287.6 eV of **HTC** film (120 nm). In this figure, a combination of raft-like structures (vertical and horizontal bars, oriented 90^o to each other) and disk-like structures (round domains) are observed. NEXAFS spectra extracted from these domains are presented in Figure 5(b). The spectrum extracted from a vertically-oriented bar shows maximum absorption at ~293 eV, corresponding to a Carbon 1s $\rightarrow \sigma^*_{C\text{-}C}$ transition. The spectrum from a

horizontally-oriented bar has a maximum at ~288 eV (Carbon 1s → $\sigma^*_{C\text{-}H}$ transition). These results indicate that the macromolecular axis of **HTC** molecules in each raft-element is parallel to the substrate surface, but oriented **normal** to the longitudinal direction of the element. The HTC molecular orientation is attributed to epitaxy along the two crystallographically equivalent directions on the NaCl(001) surface, as shown in Figure 3. Some defects (raft elements that are not orthogonally oriented) can be attributed to the flotation of the sample on H_2O that is used to remove the NaCl substrate. In addition to the raft elements, thinner "disk-like structures" are observed between the raft elements. The NEXAFS spectra show that **HTC** molecules in these domains are oriented normal to the substrate surface (solid line in Figure 5(b)).

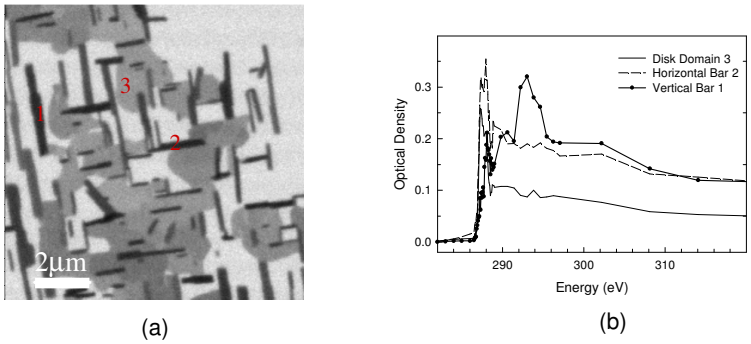

Figure 5 (a) X-ray absorption image at 287.6 eV of **HTC** films, thermally evaporated on NaCl (001) face at T_s = RT. (b) NEXAFS spectra correspond to the image contrast in image (a). The optical density for these spectra at 330 eV is different (solid line+dot, OD=0.12; dashed line, OD=0.12; and solid line, OD=0.05), indicating that the raft-like structure has the same thickness, which is thicker than disk-like structure.

The variation of molecular orientation for the longer **HC** molecules (Figure 4) and the shorter **HTC** molecules (Figure 5) can be understood by considering the degree of supercooling,[39] which is defined as the difference between the melting point T_m of the alkane molecules and the substrate temperature T_s: $\Delta T = T_m - T_s$. Specifically, higher ΔT gives lateral orientation, lower ΔT produces normal orientation, and at intermediate

ΔT, lateral and normal orientation could coexist. The ΔT for **HC** (T_m = 98°C) and **HTC** (T_m = 74°C) at T_s = RT is 76°C and 52°C, respectively. This degree of supercooling is a useful generalization for tracking these structural changes, as the melting point increases with the n-alkane chain length, but the temperature relative to the melting point is the most important variable.

These observations can be better understood by considering the relative contribution of the enthalpy and entropy to the free energy associated with the different molecular orientations and the kinetics of nucleation for the formation of oriented domains.

There is a tendency for the $–CH_3$ group to be at the surface due to the lower interfacial energy of the $–CH_3$ group compared to the $–CH_2$ groups.[46,47] Therefore, when the system is allowed to approach equilibrium, the preferred *n*-alkane orientation would be normal to the substrate surface. However, for the deposition of vapor molecules on a substrate surface, at a "supercooled temperature" (larger ΔT), the system is not in equilibrium. The vapor molecules can be kinetically trapped in a non-equilibrium state, oriented laterally in the surface plane. Therefore, the formation of thin films from vapor phase can be a kinetically limited process.

When the vapor molecules are deposited on a substrate, the enthalpy change (ΔH) and the entropy change (ΔS) are negative. For longer chain molecules, the magnitude of ΔH increases with the chain length, and the magnitude of the ΔS term is depends on the molecular orientation and substrate temperature. The combination of these terms determines the free energy associated with different molecular orientations, and the driving force, even if the morphology is kinetically limited.

Let us first consider the interaction of a single n-alkane chain with the substrate. The interaction energy between the substrate surface and the *n*-alkane chain was calculated by Mauritz *et al.*[32] as 100 kJ mol^{-1} $9CH_2^{-1}$, or 11.2 kJ mol^{-1} CH_2^{-1} between NaCl and methylene group. This is consistent with the recent ~0.1 eV CH_2^{-1} for *n*-alkane interaction with graphite.[48,49] Based on this value, the interaction energy with NaCl would be ~670 kJ mol^{-1} for **HC** and ~402 kJ mol^{-1} for **HTC** provided all CH_2 groups are on the substrate. The term ΔS depends on the molecular orientation and T_s. In the *n*-alkane/NaCl system, when the alkane molecule is laterally oriented on the substrate surface along the <110> and <$\bar{1}$10> directions, the molecule is relatively confined in an ordered structure. In contrast, when the molecule is normally oriented on the substrate surface, more sites are available to accommodate each molecules. Gauche defects[50], the internal degrees of freedom, are likely to form when the molecule is normal to the substrate and at higher substrate temperature. Therefore, for a single n-alkane molecule, the molecule will lie laterally on the substrate surface if the enthalpic interactions are stronger, and will orient normal to the surface is the enthalpic contributions are weaker.

For many n-alkane chains, intermolecular or alkane-alkane interactions need to be considered in addition to the molecule– substrate interactions. In multilayer films, the enthalpic intermolecular contributions are similar for a normal or lateral molecular orientation, e.g. similar "bulk" intermolecular interactions will exist. Therefore, one expects that in the formation of a multilayer sample, the subsequent layers will follow the pattern of the first layer.

Due to the similar "bulk" intermolecular enthalpies, the growth mechanism (layer-by-layer *versus* 3D island) of the first layers determines the ultimate morphology of the thin film. If the bare substrate surface has lower free energy, small clusters are nucleated directed on the substrate to minimize the total free energy. The clusters then grow into 3D islands, which in turn coalesce to form a film. This film may have variation in thickness and defects at the interfaces where adjacent clusters coalesce. However, if the interface free energy between the film and the substrate is low enough, the deposited materials wet the substrate completely to minimize the total free energy, and a uniform monolayer will be formed. Once the first monolayer is formed, the subsequent deposits follow the monolayer pattern, and therefore the deposited materials form a uniform layer-by-layer structure.

At room temperature, the strong enthalpic interaction of **HC** molecules with NaCl (001) surface will tend to hold the **HC** molecules oriented along the substrate surface. This strong interaction also lowers the film-substrate interfacial free energy; therefore, the **HC** molecules tend to wet the substrate surface to form a layer-by-layer growth, i.e. the epitaxial growth of **HC** molecules on NaCl (001) likely assume growth according to the Frank-van der Merwe mode.[51] However, for the shorter **HTC** molecules, the interaction between the **HTC** molecules and the substrate surface is weaker (less negative ΔH). This weak interaction may not hold the **HTC** molecules oriented along the surface and some **HTC** molecules gain thermal energy to reorient. Thus, the free energy is dominated by the entropic term, causing the molecules to adopt normal orientation. However, the observation of the coexistence of normal and lateral orientation leads us to conclude that this reorientation is a kinetic limited process. It

could be due to that this reorientation process from lateral to normal orientation is slow (e.g. kinetically trapped) or that the deposition rate is so fast that the lateral oriented **HTC** molecules do not have enough time to reorient before they are buried by subsequent molecules. In terms of the **HTC** thin film morphology, the film-substrate interfacial free energy is such that the **HTC** molecules tend to form 3-dimensional island growth (VW growth mode) rather than wetting the substrate.

In the **HTC** thin film, we observe that the **HTC** molecules in the raft-like structure are perpendicular to the longitudinal direction of the raft-like element (see figure 5). This is contrary to the electron diffraction results,[4] that concluded that the macromolecular axis (*c*-axis in the unit cell) of **HTC** molecules in the raft-like structure were oriented along the longitudinal direction of the raft-like structure. In the electron diffraction measurements, the beam was defocused over many domains to limit radiation damage; here, x-ray microscopy can examine individual crystallites with minimal radiation damage. The analysis of these raft elements shows an energetic preference for the addition of new **HTC** molecules aligned along side of other **HTC** molecules, over head-to-tail arrangements of molecules with the same orientation. This argument is illustrated in Figure 6. This effect – and the resultant growth of long raft structures where the chains are oriented perpendicular to the long direction shows the preferential growth in the direction that maximizes favorable edge-to-edge van der Waals interactions. This result nicely illustrates the power of x-ray microscopy for analyzing molecular orientation at the nanoscale.

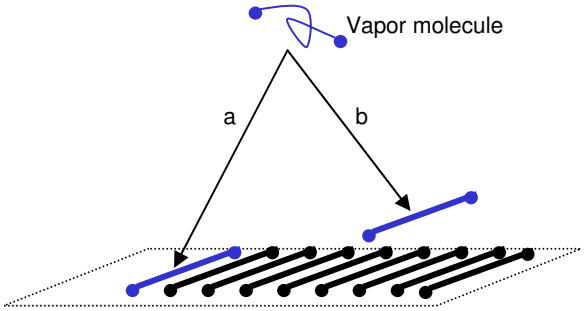

Figure 6 Vapor HTC molecule adsorbs on the substrate or the already-formed film in two ways: (a) along side of other HTC molecule, and (b) head-to-tail arrangement. The side-by-side is the energetic preferential arrangement.

3.3. Morphology and orientation of linear alkanes deposited on substrates at different temperatures

Thin films of linear alkanes n-hexacontane (n-$C_{60}H_{122}$, **HC**) and n-hexatriacontane (n-$C_{36}H_{74}$, **HTC**) were deposited onto a NaCl (001) surface at various substrate temperatures. These conditions are: T_s = RT, 36°C, 40°C, 45°C, 48°C, and 60°C for **HC** thin films, and T_s = RT and 40°C for **HTC** thin films.

Figure 7 presents X-ray microscopy images (left column) and the NEXAFS spectra extracted (right column) from the corresponding light and dark domains in respective images of **HC** thin films deposited at different substrate temperatures (a) RT, (b) 36°C, (c) 40°C, (d) 45°C, (e) 48°C, and (f) 60°C. These images were acquired at the energy of the Carbon 1s → $\sigma^*_{C\text{-}H}$ transitions (287.6 eV) where the image contrast is dominated by molecular orientation.

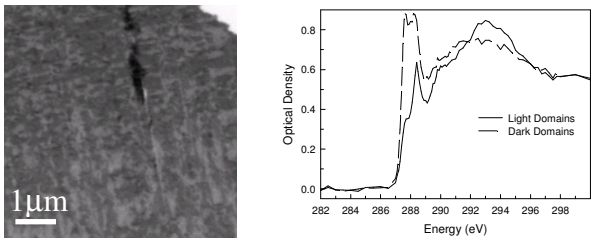

(a) HC, T_s = r.t.

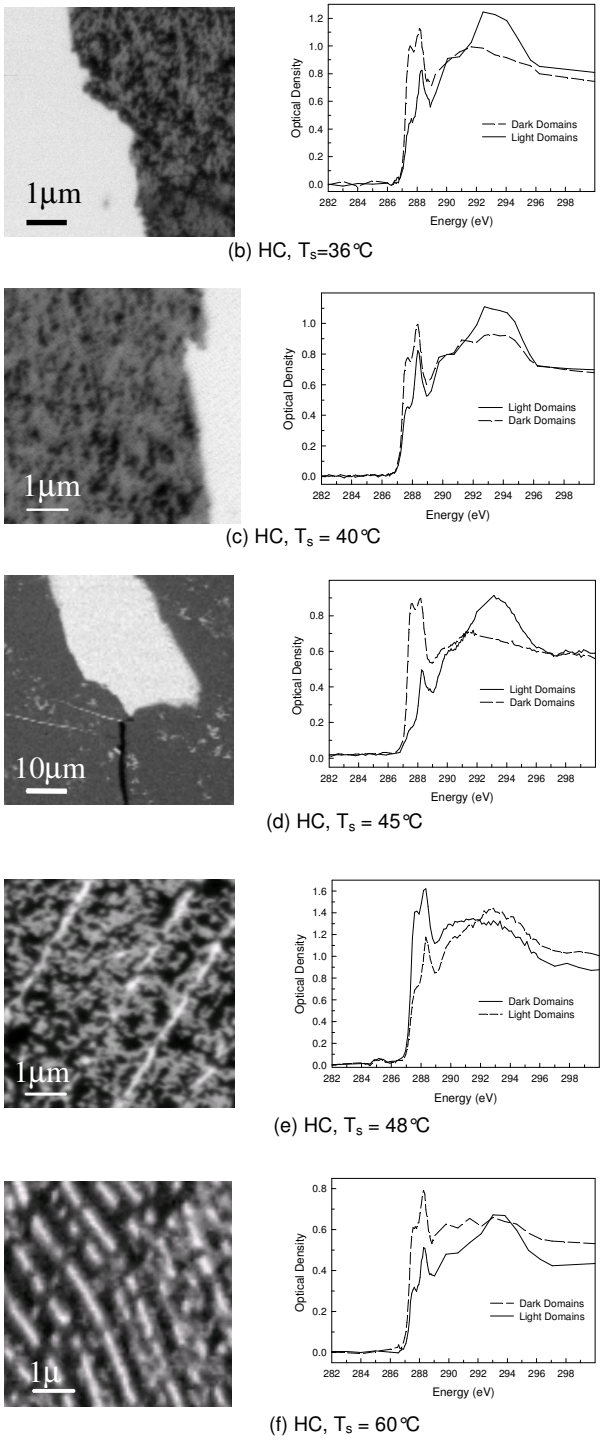

Figure 7 X-ray absorption images at 287.6 eV and corresponding NEXAFS spectra of **HC** films, thermally evaporated on NaCl (001) face at different substrate temperatures. (a) T_s = RT, (b) T_s = 36°C, (c) T_s = 40°C, (d) T_s = 45°C, (e) T_s = 48°C, (f) T_s = 60°C. The HC films are uniform up to T_s = 45°C as revealed by the optical density

at 330 eV for spectra of dark and light domains in each image. The HC films are not uniform at T_s = 48°C and 60°C.

In the **HC** film prepared on a room temperature substrate (T_s = RT; Figure 7(a), image), many small domains are observed, with a visually estimated domain size of ~50 nm. NEXAFS spectra extracted from dark and light domains (Figure 7(a), right) shows that the sample has a uniform thickness (similar optical density at 320 eV) and that the contrast arises from molecular orientation alone. When the **HC** sample was deposited on a slightly warmed NaCl(001) substrate (T_s = 36°C, Figure 7(b), image; T_s = 40°C, Figure 7(c), image), the *lateral size* of the oriented domains increases slightly (~100 nm to ~1 micron). The continuum of the NEXAFS spectra for these samples (Figures 7(a), 7(b) and 7(c), spectra) is similar for the light and dark domains, indicating that the thickness of the domains is the same. In these spectra, the Carbon 1s $\rightarrow \sigma^*_{C\text{-}H}$ band (at 287.6 eV) and the Carbon 1s $\rightarrow \sigma^*_{C\text{-}C}$ band (at 293.5 eV) all show strong linear dichroism from in-plane molecular orientation. However, the contrast varies because the samples are not aligned identically with the electric field vector in the image.

In the Figure 7(c) image, it appears that one orientation – the light domains – is predominant over the dark domains. The size of the dominant oriented domain increases further as the deposition substrate temperature is increased to 45°C (see Figure 7(d) image). Only a small portion of defects with an orthogonal orientation are present, visible as small white patches in the Figure 7(d) image. In fact, this sample consists of a major phase oriented in one direction over the range of 50 – 100 microns, with small orthogonally oriented defects, as well as some larger (10-20 micron) regions

oriented orthogonally. The sample thickness remains uniform. The contrast in this pattern sample inverts when the sample is rotated.

The increase in domain size with increasing T_s has also been observed by other researchers.[34] The T_s can be viewed as supplying kinetic energy required by the deposited molecules to move along the substrate surface. At low substrate temperature, the molecular movement on the substrate is limited and many crystallization nuclei are formed. At high substrate temperature, the movement of molecules along the substrate surface is enhanced and only a limited number of nuclei are formed, therefore, the size of domains becomes larger.

The domain size (A) is related to the T_s by[52,53]

$$A \propto \left(\frac{D_0 \exp(-E_a / kT_s)}{F} \right)^{\chi} \qquad (6)$$

where D_0 is the pre-exponential factor, E_a is the diffusion energy barrier, k is the Planck constant, χ is an exponent and less than 1, T_s is the substrate temperature, and F is the deposition rate. D_0 and E_a are affected by the substrate materials. As seen from Eq. (6), increasing T_s has the possibility to increase the domain size.

When the substrate temperature was increased further to 48°C and 60°C, the corresponding X-ray absorption images and extracted X-ray absorption spectra from corresponding images are shown in Figure 7(e) and Figure 7(f), respectively. The images contain pebble-like voids. The corresponding NEXAFS spectra (Figure 7(e) and 7(f) spectra) reveal that up to T_s = 60°C, the **HC** molecules are still laterally-oriented although thickness differentiation occurs.

Figure 8 presents typical X-ray microscope images (left column) and corresponding X-ray absorption spectra (right column) of an **HTC** film prepared by

epitaxial growth on NaCl (001) face at room temperature (T_s = RT) and at 40°C (T_s = 40°C).

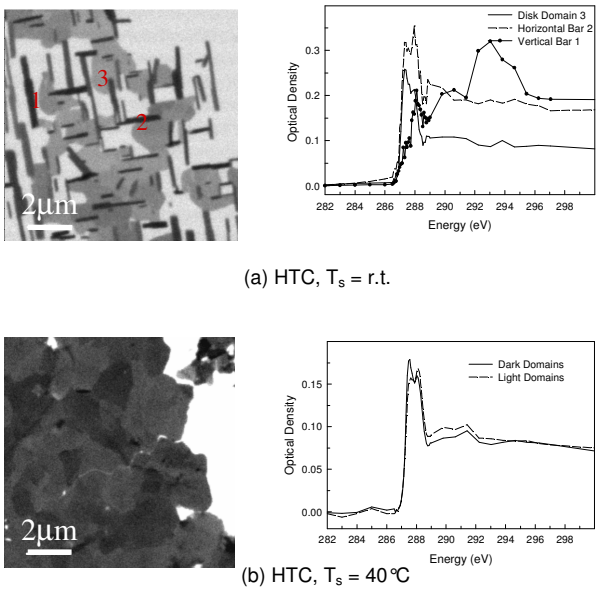

Figure 8 X-ray absorption image at 287.6eV and corresponding NEXAFS spectra of **HTC** films, thermally evaporated on NaCl (001) face at different substrate temperatures. (a) T_s = RT, (b) T_s = 40°C. The HTC film is not uniform at T_s = RT, but uniform at T_s = 40°C.

The **HTC** thin films prepared at room temperature are not uniform, and show domains with lateral- and normal-orientation as described in §3.2. For the **HTC** film deposited at T_s = 40°C, the image contrast is decreased, and the NEXAFS spectra extracted from different domains (Figure 8(b) spectra) are similar. Specifically, the intensity of the Carbon 1s $\rightarrow \sigma^*_{C\text{-}H}$ transitions indicate that the chains are ~normal to the sample surface, and the continuum intensity shows that the thickness is nearly uniform. Slight differences in the Carbon 1s $\rightarrow \sigma^*_{C\text{-}H}$ transitions are observed for different regions. These are due to different contributions of crystalline peaks; following the observation of Ade *et al.*[47] The normal orientation is consistent with the

result of Ueda *et. al.*,[4] where an **HTC** film heat treated at 50°C (24°C below **HTC** melting point), changes from a raft-like structure into small blocks, and the molecular orientation changes from lateral to normal orientation.

In the case of **HC** thin films deposited at T_s up to 60°C, **HC** molecules remain laterally oriented. This leads us to conclude that the strong interaction between the **HC** molecules and NaCl surface is the key to hold the **HC** molecules along the surface. A smaller domain size and the film thickness variation are observed at higher T_s. This might be due to the kinetics of film growth. At high T_s, the adsorbed molecules might obtain the necessary kinetic energy to migrate along the substrate surface, to re-evaporate to the vapor phase, or condense on the top of the existing clusters. Alternatively, this may be an example of an Ostwald-like ripening process, where domains of one orientation gain at the expense of the other orientation. Resolution of this question will require further study, as the thin film structure is influenced by many other factors such as deposition rate, film thickness, and the combination of deposit and substrate materials.

In the case of **HTC**, at T_s = RT, some of the **HTC** molecules adopt a normal orientation due to the relatively weak interaction between **HTC** molecules and substrate. This is expected as HTC is much shorter then **HC**, and the molecule-substrate interaction is expected to scale with the number of CH_2 groups. At T_s = 40°C, all of the **HTC** molecules gain enough energy to overcome the interaction with the substrate and become normal-oriented. The fact that **HTC** molecule's orientation changes from lateral at T_s = RT to normal at T_s = 40°C leads us to conclude that if a

weaker molecule-substrate interaction exists, then the substrate temperature (T_s) plays an important role in defining the molecular orientation of linear alkanes.

Conclusions:

The morphology and molecular orientation of linear alkanes on NaCl (001) surface have been investigated by NEXAFS spectroscopy and microscopy. Both the chain length and substrate temperature affect the morphology and molecular orientation. This phenomenon is rationalized by considering the relative contribution of enthalpy and entropy to the free energy associated with the different molecular orientation. The strong interaction between the longer chain (**HC**) molecules and NaCl (001) surface is responsible for the lateral orientation in the investigated substrate temperature range. For shorter chains (**HTC**), the weaker interaction with the substrate leads to a stronger role of the substrate temperature, T_s, in defining the molecular orientation. Based on the morphology observed, at T_s = RT, the longer chain films (**HC**) grow by Frank-van der Merwe growth mode, while for shorter chain (HTC), grows by Volmer-Weber mode.

Acknowledgements

This research was supported by the Natural Sciences and Engineering Research Council, the Canadian Foundation for Innovation, the Saskatchewan Synchrotron Institute, the University of Saskatchewan and the Chemistry Department of the University of Saskatchewan. The authors are grateful to A.L.D. Kilcoyne and T. Tylizczak for help with the operation of the STXM microscopes at the ALS. The use of the ALS 5.3.2 STXM is supported by NSF DMR-9975694, DOE DE-FG02-98ER45737, Dow Chemical, an NSERC MFA, and the Canadian Foundation for

Innovation. The ALS is supported by the Director, Office of Science, Office of Basic Energy Sciences, of the U.S. Department of Energy under Contract No. DE-AC03-76SF00098. We wish to thank Professors R. E. Verrall, R.K. Bowles, and H. Ade for their helpful comments.

References:

(1) Forrest, S. R. *Chemical Reviews* **1997**, *97*, 1973.

(2) Witte, G.; Wöll, C. *Journal of Materials Research* **2004**, *19*, 1889.

(3) Wellinghoff, S.; Rybnikar, F.; Baer, E. *Journal of Macromol Sci.----Phys.* **1974**, *B10*, 1.

(4) Ueda, Y.; Ashida, M. *Journal of Electron Microscopy* **1980**, *29*, 38.

(5) Zhang, W. P.; Dorset, D. L. *Journal of Polymer Science: Part B: Polymer Physics* **1989**, *27*, 1433.

(6) Shimizu, H.; Tanigaki, N.; Nakayama, K. *Jpn. J. Appl. Phys.* **1995**, *34*, L701.

(7) Ishida, K.; Hayashi, K.; Yoshida, Y.; Horiuchi, T.; Matsushige, K. *Journal of Applied Physics* **1993**, *73*, 7338.

(8) Horiuchi, T.; Matsushige, K. *Spectrochimica Acta* **1993**, *48B*, 137.

(9) Craig, A.; Hastie, G. P.; Roberts, K. J.; Sherwood, J. N. *Journal of Material Science* **1994**, *4*, 977.

(10) Takiguchi, H.; Izawa, M.; Yase, K.; Ueno, N.; Yoshimura, M.; Yao, T.; Sato, K. *Journal of Crystal Growth* **1995**, *146*, 645.

(11) Magonov, S. N.; Yerina, N. A. *Langmuir* **2003**, *19*, 500.

(12) Hosoi, Y.; Sakurai, Y.; Yamamoto, M.; Ishii, H.; Ouchi, Y.; Seki, K. *Surface Science* **2002**, *515*, 157.

(13) Yamamoto, M.; Sakurai, Y.; Hosoi, Y.; Ishii, H.; Kajikawa, K.; Ouchi, Y.; Seki, K. *Journal of Physical Chemistry B* **2000**, *104*, 7363.

(14) Hastie, G. P.; Johnstone, J.; Roberts, K. J.; Fischer, D. *Journal Of The Chemical Society-Faraday Transactions* **1996**, *92*, 783.

(15) Hastie, G. P.; Roberts, K. J. *Langmuir* **1995**, *11*, 4170.

(16) Smith, A. P.; Urquhart, S. G.; Winesett, D. A.; Mitchell, G.; Ade, H. *Applied Spectroscopy* **2001**, *55*, 1676.

(17) Urquhart, S. G.; Ade, H. *J. Phys. Chem. B.* **2002**, *106*, 8531.

(18) Urquhart, S. G.; Hitchcock, A. P.; Smith, A. P.; Ade, H. W.; Lidy, W.; Rightor, E. G.; Mitchell, G. E. *J. Electron Spectrosc. Relat. Phenom.* **1999**, *100*, 119.

(19) Ade, H.; Hsiao, B. *Science* **1993**, *262*, 1427.

(20) Smith, A. P.; Ade, H. *Applied Physics Letters* **1996**, *69*, 3833.

(21) Peters, R. D.; Nealey, P. F.; Crain, J. N.; Himpsel, F. J. *Langmuir* **2002**, *18*, 1250.

(22) Kinzler, M.; Schertel, A.; Hähner, G.; Wöll, C.; Grunze, M. *J. Chem. Phys.* **1994**, *100*, 7722.

(23) Outka, D. A.; Stohr, J.; Rabe, J. P.; Swalen, J. D. *Journal of Chemical Physics* **1988**, *88*, 4076.

(24) Stöhr, J.; Outka, D. A.; Baberschke, K.; Arvanitis, D.; Horsley, J. A. *Physical Review B* **1987**, *36*, 2976.

(25) Fu, J.; Urquhart, S. G. *Journal of physical Chemistry A* **2005**, *109*, 11724.

(26) Stöhr, J. *NEXAFS Spectroscopy*; Springer-Verlag: New York, 1992; Vol. 25.

(27) Stöhr, J.; Outka, D. A. *Physical Review B* **1987**, *36*, 7891.

(28) Pashley, D. W. *Advances of Physics* **1965**, *14*, 327.

(29) Forrest, S. R. *Chemical Reviews* **1997**, *97*, 1793.

(30) Willems, J.; Willems, I. *Nature* **1956**, *178*, 429.

(31) Koutsky, J. A.; Walton, A. G.; Baer, E. *Journal of Polymer Science Part A-2* **1966**, *4*, 611.

(32) Mauritz, K. A.; Baer, E.; Hopfinger, A. J. *Journal of Polymer Science: Polymer Physics Edition* **1973**, *11*, 2185.

(33) Mauritz, K. A.; Baer, E.; Hopfinger, A. J. *Journal of Polymer Science: Macromolecular Reviews* **1978**, *13*, 1.

(34) Chang, J.-W.; Kim, H.; Kim, J.-K.; Ju, B. K. *Journal of the Korean Physical Society* **2003**, *42*, S268.

(35) Yamamoto, Y.; Mitsumoto, R.; Ito, E.; Araki, T.; Ouchi, Y.; Seki, K.; Takanishi, Y. *Journal of Electron Spectroscopy and Related Phenomena* **1996**, *78*, 367.

(36) Tanaka, K.; Okui, N.; Saka, T. *Thin Solid Films* **1991**, *196*, 137.

(37) Inoue, T.; Yase, K.; Okada, M. *Journal of Crystal Growth* **1987**, *83*, 306.

(38) Saito, Y.; Inaoka, K.; Kaito, C.; Okada, M. *Applied Surface Science* **1988**, *33/34*, 1298.

(39) Shimizu, H.; Tanigaki, N.; Nakayama, K. *Japanese Journal of Applied Physics* **1995**, *34*, L701.

(40) Kilcoyne, A. L. D.; Tyliszczak, T.; Steele, W. F.; Fakra, S.; Hitchcock, A. P.; Franck, K.; Anderson, E.; Harteneck, B.; Rightor, E. G.; Mitchell, G.; Yang, L.; Warwick, T.; Ade, H. *Journal of Synchrotron Radiation* **2003**, *102*, 125.

(41) Tyliszczak, T.; Warwick, T.; Kilcoyne, A. L. D.; Fakra, S.; Shuh, D. K.; Yoon, T. H.; Jr., G. E. B.; Andrews, S.; Chembrolu, V.; Strachan, J.; Acremann, Y. *AIP Conference Proceedings 705* **2004**, 1356.

(42) Kilcoyne, A. L. D.; Tyliszczak, T.; Steele, W. F.; Fakra, S.; Hitchcock, A. P.; Franck, K.; Anderson, E.; Harteneck, B.; Rightor, E. G.; Mitchell, G.; Yang, L.; Warwick, T.; Ade, H. *Journal of Synchrotron Radiation* **2003**, *10*, 125.

(43) Ma, Y.; Chen, C. T.; Meigs, G.; Randall, K.; Sette, F. *Physical Review A* **1991**, *44*, 1848.

(44) Stöhr, J.; Outka, D. A.; Baberschke, K.; Arvanitis, D.; Horsley, J. A. *Physical Review B* **1987**, *36*, 2976.

(45) Outka, D. A.; Stohr, J.; Rabe, J. P.; Swalen, J. D.; Rotermund, H. H. *Physical Review Letters* **1987**, *59*, 1321.

(46) Wang, Y.; Rafailovich, M.; Sokolov, J.; Gersappe, D.; Araki, T.; Zou, Y.; Kilcoyne, A. D. L.; Ade, H.; Marom, G.; Lustiger, A. *Physical Review Letters* **2006**, *96*, 028303.

(47) Zou, Y.; Araki, T.; Appel, G.; Kilcoyne, A. D. L.; Ade, H. *Chemical Physics Letters* **2006**, *accepted*.

(48) Lei, R. Z.; Gellman, A. J.; Koel, B. E. *Surface Science* **2004**, *554*, 125.

(49) Yin, S.; Wang, C.; Qiu, X.; Bai, C. *Surface and Interface Analysis* **2001**, *32*, 248.

(50) Kim, Y.; Strauss, H. L.; Synder, R. G. *Journal of Physical Chemistry* **1989**, *93*, 7520.

(51) Pashley, D. W. *Materials Science and Technology* **1999**, *15*, 2.

(52) Amar, J. G.; Family, F. *Physical Review Letters* **1995**, *74*, 2066.

(53) Ruiz, R.; Choudhary, D.; Nickel, B.; Toccoli, T.; Chang, K.-C.; Mayer, A. C.; Clancy, P.; Blakely, J. M.; Headrick, R. L.; Iannotta, S.; Malliaras, G. G. *Chemistry of Materials* **2004**, *16*, 4497.

3.6 Conclusions

LD in the NEXAFS spectroscopy of *n*-alkane thin films has been studied for HC thin films. HC thin films were prepared by epitaxial growth on cleaved NaCl (001) surface. The HC molecules are laterally oriented on the NaCl surface along two equivalent crystallographic <110> and <$\bar{1}$10> directions of the NaCl (001) surface. Large orientational domains were obtained when this thin film was prepared on cleaved NaCl (001) surface at an elevated substrate temperature (T_s = 45°C).

The analysis of the angular dependence NEXAFS spectra reveals that TDM of the C 1s $\rightarrow \sigma^*_{C\text{-}C}$ transition at 293.5 eV in *n*-alkane molecules is oriented along the macromolecular axis, most closely corresponding to the molecular orbital model and explicitly excluding the building block model. In addition, four features are revealed below the C 1s IP. The first two features exhibit a strong LD with the transition intensity nearly zero when the ***E*** vector is along the macromolecular backbone. The third feature exhibits a weak, opposite LD compared to the first two features. The fourth feature is unexpectedly broad, but is necessary to achieve the best fit. Its origin is not clear.

ab initio calculations have been carried out on an isolated nonane molecule, nonane cluster, and propane cluster. The calculations of the isolated nonane molecule with minimal basis set reveal that the transition dipole moment of the C 1s $\rightarrow \sigma^*_{C\text{-}C}$ transition is along the macromolecular axis. Four features below the C 1s IP for n-alkanes were revealed in the condensed phase. Detailed analysis of the orbital size, singlet-triplet energy separation, and oscillator strength of these features reveals that

the first two pre-edge features are dominated by valence character. The transition dipole moment of these two resonances is oriented in the CH_2 plane, perpendicular to the macromolecular axis. The third transition is of Rydberg character, whose transition dipole moment is along the macromolecular axis. These results are consistent with our experimental linear dichroism for these features.

It is found that the molecular orientation of *n*-alkanes in the thin films is strongly dependent on the interaction between the molecule and substrate. The stronger the interaction, the more likely lateral molecular orientation is formed. This interaction depends on the *n*-alkane chain length and the substrate materials. Therefore, at T_s = RT, the HC molecules are all laterally oriented on the cleaved NaCl (001) surface, while HTC molecules are only partially laterally oriented on the cleaved NaCl (001) surface. However, at elevated substrate temperature, if the interaction between the substrate and deposit is not strong enough, the thermal energy of the molecules may overcome this weak interaction, i.e. the normal orientation is formed in preference to lateral orientation. That is the case for the HTC thin films prepared at T_s = 40°C.

3.7 Future work

In-situ STXM measurement

It has been shown in §3.5 that the morphology of *n*-alkane thin films changes with the substrate temperature. An in-situ X-ray microscopy study of these thin films is intended to understand how the *n*-alkane morphology changes with temperature and to study the phase transition of *n*-alkanes. A STXM microscope compatible with the *in situ* heating cell has been designed and will be used to investigate the temperature effect on the morphology of *n*-alkane thin films. Figure 3.16 shows the structure of the in situ heating cell.

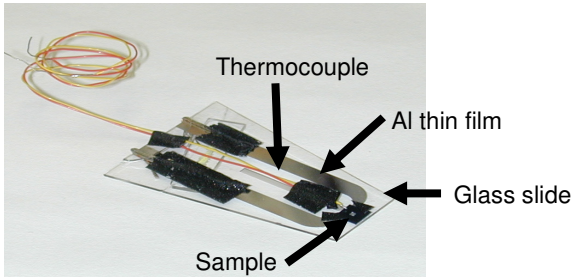

Figure 3.16 Structure of the in situ heating cell, compatible with the STXM microscope.

Theoretical calculations

Experiments (Zou et al. 2006) have shown a great difference in the C 1s $\rightarrow \sigma^*_{C\text{-}H}$/Rydberg region in the NEXAFS spectra of two alkane crystals n-$C_{19}H_{40}$ and n-$C_{40}H_{82}$. The spectrum of n-$C_{40}H_{82}$ has a doublet splitting of ~0.6 eV, whereas the splitting of the doublet increases to ~0.9 eV in the spectrum of n-$C_{19}H_{40}$ with a third component developing into a recognizable feature at intermediate energy. These differences might be ascribed to the crystal structure associated with the different

length. Theoretical studies are needed in order to show that the subtle change in the crystal structure can substantially affect the electronic structure of n-alkanes.

These theoretical studies are intended to be carried out on nonane clusters. These clusters are designed based on different n-alkane crystal structures. To begin with, three sets of calculation are under consideration:

(1) orthorhombic structure: a = 7.40 Å, b = 4.93 Å, a/b = 1.501, θ =48°

(2) hexagonal structure: a = 8.30 Å, b = 4.79 Å, a/b = 1.732, θ =45°

(3) orthorhombic structure: a = 7.4 Å, b = 4.93 Å, a/b = 1.501, θ =45°

References:

Ade, H. (1997). "Compositional and orientational characterization of polymeric systems with x-ray microscopy." Trends in Polymer Science **5**(2): 58-66.

Ade, H. and B. Hsiao (1993). "X-Ray Linear Dichroism Microscopy." Science **262**(5138): 1427-1429.

Ade, H., A. L. D. Kilcoyne, T. Tyliszczak, P. Hitchcock, E. Anderson, B. Harteneck, E. G. Rightor, G. Mitchell, A. P. Hitchcock and T. Warwick (2003). "Scanning transmission X-ray microscopy at a bending magnet beamline at the Adcanced Light Source." Journal De Physique IV **104**: 3-8.

Ade, H. and S. G. Urquhart (2002). NEXAFS spectroscopy and microscopy of natural and synthetic polymers. Chemical Applications of Synchrotron Radiation. T.-K. Sham. Singapore, World Scientific Publishing Co. Pte. Ltd.**:** 285-355.

Ade, H., X. Zhang, S. Cameron, C. Costello, J. Kirz and S. Williams (1992). "Chemical contrast in x-ray microscopy and spatially resolved XANES spectroscopy of organic specimens." Science **258**(5084): 972-975.

Ade, H., Y. Zou, A. D. L. Kilcoyne, Y. Wang, M. Rafailovich and M. Sokolowski (2004). "X-ray linear dichroism microscopy of crystalline short chain alkanes and semi-crystalline polyethylene thin films." Microscopy Microanalysis **10 (Suppl 2)**: 1020-1021.

Ågren, H., V. Carravetta, O. Vahtras and L. G. M. Pettersson (1995). "Orientational Probing of Polymeric Thin-Films by Nexafs - Calculations on Polytetrafluoroethylene." Physical Review B **51**(24): 17848-17855.

Amar, J. G. and F. Family (1995). "Critical cluster size: island morphology and size distribution in submonolayer epitaxial growth." Physical Review Letters **74**(11): 2066-2069.

Ashida, M., Y. Ueda and H. Yanagi (1986). "The effect of the substrate on the epitaxial growth of the hexatriacontane crystal." Bulletin of the Chemical Society of Japan **59**: 1437-1441.

Bagus, P. S., K. Weiss, A. Schertel, C. Wöll, W. Braun, C. Hellwig and C. Jung (1996). "Identification of transitions into Rydberg states in the X-ray absorption spectra of condensed long-chain alkanes." Chemical Physics Letters **248**(3-4): 129-135.

Balta Calleja, F. J. (1965). "X-ray investigations of paraffin single crystals in relation with their morphological features." Rev. Real Acad. Cienc. Exact. Fis. Nat. Madrid **59**: 71-93.

Bouchoms, I. P. M., W. A. Schoonveld, J. Vrijmoeth and T. M. Klapwijk (1999). "Morphology identification of the thin film phases of vacuum evaporated pentacene on SiO_2 substrates." Synthetic Metals **104**: 175-178.

Buckley, C. J., N. Khaleque, S. J. Bellamy, M. Robins and X. Zhang (1997). "Mapping the organic and inorganic components of tissure using NEXAFS." Journal De Physique. IV, Colloque: JP **7**(1): 83-90.

Bunn, C. W. and R. D. P. Daubeny (1954). "The polarizabilities of carbon - carbon bonds." Transaction of the Faraday Society **50**(11): 1173-1177.

Castner, D. G., K. B. Lewis, D. Fischer, B. D. Ratner and J. L. Gland (1993). "Determination of surface structure and orientation of polymerized

tetrafluoroethylene films by near-edge X-ray absorption Fine structure, X-ray photoelectron spectroscopy, and static secondary ion mass spectrometry." Langmuir **9**: 537-542.

Chang, J.-W., H. Kim, J. K. Kim and B. K. Ju (2003). "Structure and morphology of vacuum-evaporated pentacene as a function of substrate temperature." Journal of the Korean Physical Society **42**: S268-S272.

Charney, E. (1988). "Electric linear dichroism and birefringence of biological polyelectrolytes." Quarterly Reviews of Biophysics **25**(1): 1-60.

Chkoda, L., M. Schneider, V. Shklover, L. Kilian, M. Sokolowski, C. Heske and E. Umbach (2003). "Temperature-dependent morphology and structure of ordered 3,4,9,10-perylene-tetracarboxylicacid-dianhydride (PTCDA) thin films on Ag (111)." Chemical Physics Letters **371**: 548-552.

Coffey, T., S. G. Urquhart and H. Ade (2002). "Characterization of the effects of soft X-ray irradiation on polymers." Journal of Electron Spectroscopy and Related Phenomena **122**(1): 65-78.

Cossy-Favre, A., J. Diaz, Y. Liu, H. R. Brown, M. G. Samant, J. Stohr, A. J. Hanna, S. Anders and T. P. Russell (1998). "X-PEEM study on surface orientation of stylized and rubbed polyimides." Macromolecules **31**(15): 4957-4962.

Cotton, F. A. (1990). Chemical Applications of Group Theory. New York.

Crain, J. N., A. Kirakosian, J. L. Lin, Y. D. Gu, R. R. Shah, N. L. Abbott and F. J. Himpsel (2001). "Functionalization of silicon step arrays II: Molecular orientation of alkanes and DNA." Journal of Applied Physics **90**(7): 3291-3295.

Croll, L. M., J. F. Britten, C. Morin, A. P. Hitchcock and H. D. H. Stöver (2003). "Integrating near-edge X-ray absorption fine structure (NEXAFS) microscopy and crystallography: the effect of molecular order." Journal of Synchrotron Radiation **10**: 265-268.

Dhez, O., H. Ade and S. G. Urquhart (2002). "Calibrated NEXAFS spectra of some common polymers." Journal of Electron Spectroscopy and Related Phenomena **128**: 85-96.

Dorset, D. L. (1986). "Electron diffraction structure analysis of epitaxially crystallized n-paraffins." Journal of Polymer Science: Polymer Physics Edition **24**: 79-87.

Dutartre, D., P. Warren, F. Chollet, F. Gisbert, M. Berenguer and I. Berbezier (1994). "Defect-free Stranski-Krastanov growth of strained Si1-xGex layers on Si." Journal of Crystal Growth **142**(1-2): 78-86.

Ernst, K. H., M. Neuber, M. Grunze and U. Ellerbeck (2001). "NEXAFS study on the orientation of chiral P-heptahelicene on Ni(100)." Journal of the American Chemical Society **123**(3): 493-495.

Forrest, S. R. (1997). "Ultrathin organic films grown by organic molecular beam deposition and related techniques." Chemical Reviews **97**: 1793-1896.

Gamble, L. J., B. Ravel, D. A. Fischer and D. G. Castner (2002). "Surface structure and orientation of PTFE films determined by experimental and FEFF8-calculated NEXAFS spectra." Langmuir **18**(6): 2183-2189.

Genzer, J., D. Fischer and K. Efimenko (2003). "Combinatorial near-edge x-ray absorption fine structure: simultaneous determination of molecular orientation

and bond concentration on chemically heterogeneous surfaces." Applied Physics Letters **82**(2): 266-268.

Genzer, J., E. J. Kramer and D. A. Fischer (2002). "Accounting for Auger yield energy loss for improved determination of molecular orientation using soft x-ray absorption spectroscopy." Journal of Applied Physics **92**(12): 7070-7079.

Genzer, J., E. Sivaniah, E. J. Kramer, J. G. Wang, H. Korner, K. Char, C. K. Ober, B. M. DeKoven, R. A. Bubeck, D. A. Fischer and S. Sambasivan (2000). "Temperature dependence of molecular orientation on the surfaces of semifluorinated polymer thin films." Langmuir **16**(4): 1993-1997.

Genzer, J., E. Sivaniah, E. J. Kramer, J. G. Wang, H. Korner, M. L. Xiang, K. Char, C. K. Ober, B. M. DeKoven, R. A. Bubeck, M. K. Chaudhury, S. Sambasivan and D. A. Fischer (2000). "The orientation of semifluorinated alkanes attached to polymers at the surface of polymer films." Macromolecules **33**(5): 1882-1887.

Genzer, J., E. Sivaniah, E. J. Kramer, J. G. Wang, M. L. Xiang, K. Char, C. K. Ober, R. A. Bubeck, D. A. Fischer, M. Graupe, R. Colorado, O. E. Shmakova and T. R. Lee (2000). "Molecular orientation of single and two-armed monodendron semifluorinated chains on "soft" and "hard" surfaces studied using NEXAFS." Macromolecules **33**(16): 6068-6077.

Giebler, R., B. Schulz, J. Reiche, L. Brehmer, M. Wuhn, C. Woll, A. P. Smith, S. G. Urquhart, H. W. Ade and W. E. S. Unger (1999). "Near-edge X-ray absorption fine structure spectroscopy on ordered films of an amphiphilic derivate of 2,5-diphenyl-1,3,4- oxadiazole." Langmuir **15**(4): 1291-1298.

Gilmer, G. H. (1993). Atomic-scale models of crystal growth. Handbook of Crystal Growth. D. T. J. Hurle. Amsterdam, North-Holland. **1a:** 585.

Gordon, M. L., D. Tulumello, G. Cooper, A. P. Hitchcock, P. Glatzel, O. C. Mullins, S. P. Cramer and U. Bergmann (2003). "Inner-shell excitation spectroscopy of fused-ring aromatic molecules by electron energy loss and X-ray Raman techniques." Journal of Physical Chemistry A **107**: 8512-8520.

Hähner, G., M. Kinzler, C. Wöll, M. Grunze, M. K. Scheller and L. S. Cederbaum (1991). "Near edge X-ray-absorption fine-structure determination of alkyl-chain orientation - breakdown of the "Building-Block" scheme." Physical Review Letters **67**(7): 851-854.

Hähner, G., C. Wöll, M. Buck and M. Grunze (1993). "Investigation of intermediate steps in the self-assembly of n-alkanethiols on gold surfaces by soft-X-ray spectroscopy." Langmuir **9**(8): 1955-1958.

Hitchcock, A. P. (2000). Analysis of X-ray microscopy Images and Spectra (aXis2000).

Hitchcock, A. P. (2003). STXM 5.3.2 User Manual.

Hitchcock, A. P., C. E. Brion and M. J. Van der Wiel (1978). "Ionic fragmentation of SF6 ionised in the sulphur 2p shell." Journal of Physics B: Atom. Molec. Phys. **11**(18): 3245-3261.

Hitchcock, A. P. and I. Ishii (1987). "Carbon K-shell excitation spectra of linear and branched alkanes." Journal of Electron Spectroscopy and Related Phenomena **42**(1): 11-26.

Hitchcock, A. P., D. C. Newbury, I. Ishii, J. Stohr, J. A. Horsley, R. D. Redwing, A. L. Johnson and F. Sette (1986). "Carbon K-shell excitation of gaseous and condensed cyclic hydrocarbons: C_3H_8, C_4H_8, C_5H_{10}, C_6H_{10}, C_6H_{12}, and C_8H_8." Journal of Chemical Physics **85**(9): 4849-4862.

Hitchcock, A. P. and J. Stöhr (1987). "K-shell shape resonances and intramolecular bond lengths. Comments on "The relationship between shape resonances and bond lengths"." Journal of Chemical Physics **87**(5): 3253-3255.

Hu, H. and D. L. Dorset (1989). "Three-dimensional electron diffraction structure analysis of polyethylene." Acta Crystallographica **b45**: 283-290.

Hunt, W. J. and W. A. Goddard (1969). "Excited states of H_2O using improved virtual orbitals." Chemical Physics Letters **3**(6): 414-418.

Ianoul, A., F. Fleury, O. Duval, R. Waigh, J. C. Jardillier, A. J. P. Alix and I. Nabiev (1999). "DNA binding by fagaronine and ethoxidine, inhibitors of human DNA topoisomerases I and II, probed by SERS and flow linear dichroism spectrodcopy." Journal of Physical Chemistry B **103**(11): 2008-2013.

Ikeda, S., M. Kiguchi, Y. Yoshida, K. Yase, T. Mitsunaga, K. Inaba and K. Saiki (2004). "Epitaxial growth and domain coalescence of sexithiophene induced by the steps on cleaved KBr (001)." Journal of Crystal Growth **265**: 296-301.

Inaoka, K., K. Yase and M. Okada (1988). "Epitaxial growth of linear-chain molecules prepared by physical-vapor-deposition." Applied Surface Science **33/34**: 1293-1297.

Inoue, T., K. Yase, K. Inaoka and M. Okada (1987). "Molecular-orientation and growth-mechanism of several fatty-acids with different lengths." Journal of Crystal Growth **83**(3): 306-310.

Ishida, K., K. Hayashi, Y. Yoshida, T. Horiuchi and K. Matsushige (1993). "Structural Evaluation of Epitaxially Grown Organic Evaporated- Films by Total-Reflection X-Ray Diffractometer." Journal of Applied Physics **73**(11): 7338-7343.

Jacobsen, C., S. Wirick, G. Flynn and C. Zimba (2000). "Soft X-ray spectroscopy from image sequences with sub-100nm spatial resolution." Journal of Microscopy **197**(2): 173-184.

Kilcoyne, A. L. D., T. Tyliszczak, W. F. Steele, S. Fakra, A. P. Hitchcock, K. Franck, E. Anderson, B. Harteneck, E. G. Rightor, G. Mitchell, L. Yang, T. Warwick and H. Ade (2003). "Interferometer-controlled scanning transmission X-ray microscopes at the Advanced Light Source." Journal of Synchrotron Radiation **10**: 125-136.

Kinzler, M., A. Schertel, G. Hähner, C. Wöll, M. Grunze, H. Albrecht, G. Holzhüter and T. Gerber (1994). "Structure of monolayer and multilayer Langmuir-Blodgett-films from Cd Arachidate and Ca Arachidate." Journal of Chemical Physics **100**(10): 7722-7735.

Kinzler, M., W. Schrepp, C. Wöll and M. Grunze (1995). "Substrate effects on the structure of Langmuir-Blodgett monolayers of Cadmium Arachidate using X-ray-absorption spectroscopy." Langmuir **11**(3): 696-698.

Kirz, J., C. Jacobsen and M. Howells (1995). "Soft X-ray microscopes and their biological applications." Quarterly Reviews of Biophysics **28**(1): 33-130.

Kondoh, H., F. Matsui, Y. Ehara, T. Yokoyama and T. Ohta (2001). "Surface-monolayer-controlled molecular alignment of short n- alkane multilayers." Langmuir **17**(26): 8178-8183.

Koprinarov, I. N., A. P. Hitchcock, C. T. McCrory and R. F. Childs (2002). "Quantitative mapping of structured polymeric systems using singular value decomposition analysis of soft X-ray images." Journal of Physical Chemistry B **106**: 5358-5364.

Kortright, J. B. (2005). Personal communication.

Kosugi, N. (2000). "Advanced course in application of GSCF3 to inner-shell excitation".

Kosugi, N. and H. Kuroda (1980). "Efficient methods for solving the open-shell SCF problem and for obtaining an initial guess. The "one-hamiltonian" and the "partial SCF" methods." Chemical Physics Letters **74**(3): 490-493.

Koutsky, J. A., A. G. Walton and E. Baer (1966). "Epitaxial crystallization of homopolymers on single crystals of alkali halides." Journal of Polymer Science Part A-2 **4**: 611-629.

Kubono, A. and R. Akiyama (2002). "Orientational mechanism for long-chain organic molecules during physical vapor deposition." Molecular Crystals and Liquid Crystals **378**: 167-183.

Lee, P. A., P. H. Citrin, P. Eisenberger and B. M. Kincaid (1981). "Extended x-ray absorption fine structure--its strengths and limitations as a structural tool." Reviews of Modern Physics **53**(4, Part 1): 769-806.

Lovinger, A. J., D. D. Davis, A. Dodabalapur, H. E. Katz and L. Torsi (1996). "Single-crystal and polycrystalline morphology of the thiophene-based semiconductor alpha-hexathienyl (alpha-6T)." Macromolecules **29**: 4952-4957.

Ma, Y., C. T. Chen, G. Meigs, K. Randall and F. Sette (1991). "High-resolution K-shell photoabsorption measurements of simple molecules." Physical Review A **44**(3): 1848-1858.

Magonov, S. N. and N. A. Yerina (2003). "High-temperature atomic force microscopy of normal alkane $C_{60}H_{122}$ films on graphite." Langmuir **19**(3): 500-504.

Margaritondo, G. (1988). Introduction to Synchrotron Radiation. New York, Oxford University Press.

Margaritondo, G. (2002). Elements of synchrotron light for biology, chemistry, & medical research. New York, Oxford University Press Inc.

Marks, S., C. Cortopassi, J. De Vries, E. Hoyer, R. Leinbach, Y. Minamihara, H. Padmore, P. Pipersky, D. Plate, R. Schlueter and A. Young (1998). "The Advanced Light Source Elliptically Polarizing Undulator." Proceedings of the Particle Accelerator Conference, 17th, Vancouver, B. C., May 12-16, 1997 **3**: 3221-3223.

Matsuzaki, F. and K. Inaoka (1984). "Molecular orientation in physical-vapour deposition of long-chain stearic acid." Journal of Crystal Growth **69**: 231-240.

Mauritz, K. A., E. Baer and A. J. Hopeinger (1973). "Molecular energetics of the epitaxial crystallization of polyethylene on alkali halide substrates." Journal of Polymer Science: Polymer Physics Edition **11**: 2185-2197.

Mauritz, K. A., E. Baer and A. J. Hopfinger (1978). "The epitaxial crystallization of macromolecules." Journal of Polymer Science: Macromolecular Reviews **13**: 1-61.

Mo, Y. W., D. E. Savage, B. S. Swartzentruber and M. G. Lagally (1990). "Kinetic pathway in Stranski-Krastanov growth of Ge on Si(001)." Physical Review Letters **65**: 1020-1023.

Moss, B. and D. L. Dorset (1984). "Electron crystallography of epitaxially grown paraffin." Journal of Polymer Science: Polymer Physics Edition **22**: 1919-1929.

Moss, B. and D. L. Dorset (1985-1986). "Quantitative analysis of electron diffraction data from epitaxially grown crystals." Journal of Macromol Science - Physics **B24**(1-4): 99-118.

Mukhopadhyay, S., S. K. Mandal, S. Bhaduri and W. H. Armstrong (2004). "Manganese clusters with relevance to photosystem II." Chemical Reviews **104**: 3981-4026.

Norden, B. (1978). "Applications of linear dichroism specetroscopy." Applied Spectroscopy Reviews **14**(2): 157-248.

Ohta, T., K. Seki, T. Yokoyama, I. Morisada and K. Edamatsu (1990). "Polarized XANES studies of oriented polyethylene and fluorinated polyethylenes." Physica Scripta. **41**: 150-153.

Outka, D. A., J. Stöhr, J. P. Rabe and J. D. Swalen (1988). "The orienation of Langmuir-Blodgett monolayers using NEXAFS." Journal of Chemical Physics **88**(6): 4076-4087.

Outka, D. A., J. Stöhr, J. P. Rabe, J. D. Swalen and H. H. Rotermund (1987). "Orientation of arachidate chains in Langmuir-Blodgett monolayers on Si(111)." Physical Review Letters **59**(12): 1321-1324.

Pashley, D. W. (1965). "The nucleation, growth, structure and epitaxy of thin surface films." Advances of Physics **14**: 327-415.

Pashley, D. W. (1999). "Epitaxy growth mechanisms." Materials Science and Technology **15**: 2-8.

Pelletier, I., H. Bourque, T. Buffeteau, D. Blaudez, B. Desbat and M. Pezolet (2002). "Study by infrared spectroscopy of ultrathin films of behenic acid methyl ester on solid substrates and at the air/water interface." Journal of Physical Chemistry B **106**(8): 1968-1976.

Pelletier, I., I. Laurin, T. Buffeteau, B. Desbat and M. Pezolet (2003). "Infrared study of the molecular orientation in ultrathin films of behenic acid methyl ester: comparison between single langmuir-blodgett monolayers and spin-coated multilayers." Langmuir **19**(4): 1189-1195.

Piancastelli, M. N. (1997). "The neverending story of shape resonances." Journal of Electron Spectroscopy and Related Phenomena **100**: 167-190.

Piancastelli, M. N., D. W. Lindle, T. A. Ferrett and D. A. Shirley (1987). "The relationship between shape resonances and bond lengths." Journal of Chemical Physics **86**(5): 2765-2771.

Rightor, E. G., A. P. Hitchcock, H. Ade, R. D. Leapman, S. G. Urquhart, A. P. Smith, G. Mitchell, D. A. Fischer, H. J. Shin and T. Warwick (1997). "Spectromicroscopy of poly(ethylene terephthalate): comparison of spectra and radiation damage rates in X-ray absorption and electron energy loss." Journal of Physical Chemistry B **101**: 1950-1960.

Rodger, A. (1993). Linear Dichroism. Method in Enzymology. J. F. Riordan and B. L. Vallee. San Diego, Academic Press, Inc. **226:** 232-258.

Rodger, A. and B. Norden (1997). Circular dichroism and linear dichroism. Oxford, Oxford University Press.

Rousseau, M.-E., T. Lefèvre, L. Beaulieu, T. Asakura and M. Pézolet (2004). "Study of protein conformation and orientation in silkworm and spider silk fibers using Raman microspectroscopy." Biomacromolecules **5**: 2247-2257.

Ruiz, R., D. Choudhary, B. Nickel, T. Toccoli, K.-C. Chang, A. C. Mayer, P. Clancy, J. M. Blakely, R. L. Headrick, S. Iannotta and G. G. Malliaras (2004). "Pentacene thin film growth." Chemistry of Materials **16**: 4497-4508.

Samant, M. G., J. Stöhr, H. R. Brown, T. P. Russell, J. M. Sands and S. K. Kumar (1996). "NEXAFS studies on the surface orientation of buffed polyimides." Macromolecules **29**(26): 8334-8342.

Schellman, J. and H. P. Jensen (1997). "Optical spectroscopy of orientaed molecules." Chemical Reviews **87**: 1359-1399.

Schertel, A., G. Hähner, M. Grunze and C. Wöll (1996). "Near edge x-ray absorption fine structure investigation of the orientation and thermally induced order-disorder transition in thin organic films containing long chain hydrocarbons."

Journal of Vacuum Science & Technology a-Vacuum Surfaces and Films **14**(3): 1801-1806.

Sette, F., J. Stöhr and A. P. Hitchcock (1984). "Correlation between intramolecular bond lengths and k-shell sigma-shape resonances in gas-phase molecules." Chemical Physics Letters **110**(5): 517-520.

Shimizu, H., N. Tanigaki and K. Nakayama (1995). "Molecular orientation and periodical structure of vacuum-deposited films of long-chain molecules." Japanese Journal of Applied Physics **34**: L701-L704.

Siegbahn, K., C. Nordling, G. Johansson, J. Hedman, P. F. Heden, K. Hamrin, U. Gelius, T. Bergmark, L. O. Werme, R. Manne and Y. Baer (1969). ESCA applied to free molecules, Amsterdam, North-Holland Pub. Co.

Smith, A. P. and H. Ade (1996). "Quantitative orientational analysis of a polymeric material (Kevlar(R) fibers) with x-ray microspectroscopy." Applied Physics Letters **69**(25): 3833-3835.

Smith, A. P., S. G. Urquhart, D. A. Winesett, G. Mitchell and H. Ade (2001). "Use of near edge X-ray absorption fine structure spectromicroscopy to characterize multicomponent polymeric systems." Applied Spectroscopy **55**(12): 1676-1681.

Somers, J., A. W. Robinson, T. Lindner, D. Ricken and A. W. Bradshaw (1989). "Application of molecular symmetry in near-edge x-ray-absorption spectroscopy of adsorbed species." Physical Review B **40**(4): 2053-2059.

Srinivasan, K., K. Meera and P. Ramasamy (1999). "Enhancement of metastable zone width for solution growth of potassium acid phthalate." Journal of Crystal Growth **205**: 457-459.

Stöhr, J. (1992). NEXAFS Spectroscopy. New York, Springer-Verlag.

Stöhr, J. and D. A. Outka (1987). "Determination of molecular orientations on surfaces from the angular dependence of near-edge x-ray-absorption fine-structure spectra." Physical Review B **36**(15): 7891-7905.

Stöhr, J., D. A. Outka, K. Baberschke, D. Arvanitis and J. A. Horsley (1987). "Identification of C-H resonances in the K-sheell excitation spectra of gas-phase, chemisorbed,and polymeric hydrocarbons." Physical Review B **36**(5): 2976-2979.

Stöhr, J. and M. G. Samant (1999). "Liquid crystal alignment by rubbed polymer surfaces: a microscopic bond orientation model." Journal of Electron Spectroscopy and Related Phenomena **98-99**: 189-207.

Stöhr, J., M. G. Samant, A. Cossy-Favre, J. Díaz, Y. Momoi, S. Odahara and T. Nagata (1998). "Microscopic origin of liquid crystal alignment on rubbed polymer surfaces." Macromolecules **31**(6): 1942-1946.

Stöhr, J., M. G. Samant, J. Luning, A. C. Callegari, P. Chaudhari, J. P. Doyle, J. A. Lacey, S. A. Lien, S. Purushothaman and J. L. Speidell (2001). "Liquid crystal alignment on carbonaceous surfaces with orientational order." Science **292**(5525): 2299-2302.

Stowell, M. J. and T. J. Law (1966). "The migration of double positioning boundaries during the growth of epitaxial (111) gold films." Physica Status Solidi **16**(1): 117-125.

Tanaka, K., N. Okui and T. Sakai (1991). "Molecular-orientation behavior of paraffin thin-films made by vapor-deposition." Thin Solid Films **196**(1): 137-145.

Teare, P. W. (1959). "The crystal structure of orthorhombic hexatriacontane $C_{36}H_{74}$." Acta Crystallographica **12**: 294-300.

Teo, B. K. (1986). EXAFS: Basic principles and data analysis. New York, Spinger - Verlag.

Thompson, A., D. Attwood, E. Gullikson, M. Howells, K.-J. Kim, J. Kirz, J. Kortright, I. Lindau, P. Pianetta, A. Robinson, J. Scofield, J. Underwood, D. Vaughan and G. Williams (2001). X-ray data booklet. Berkeley.

Torsi, L., A. Dodabalapur, A. J. Lovinger, H. E. Katz, R. Ruel, D. D. Davis and K. W. Baldwin (1995). "Rapid thermal processing of alpha-hexathienylene thin-film transistors." Chemistry of Materials **7**: 2247-2251.

Tyliszczak, T. (1995). MGAUSS - multiline fitting program. McMaster University, Hamilton, now at LBNL, Berkeley, CA.

Urquhart, S. G. (1997). Delocalization and functional group fingerprinting in the core excitation spectroscopy of molecules and polymers. Department of Chemistry. Hamilton, McMaster University**:** Ph. D thesis 217.

Urquhart, S. G. and H. Ade (2002). "Trends in the carbonyl core (C 1s, O 1s) $\rightarrow \pi^*_{C=O}$ transition in the near-edge X-ray absorption fine structure spectra of organic molecules." Journal of Physical Chemistry B **106**(34): 8531-8538.

Urquhart, S. G. and R. Gillies (2005). "Rydberg-valence mixing in the carbon 1s near-edge x-ray absorption fine structure spectra of gaseous alkanes." Journal of physical Chemistry A **109**: 2151-2159.

Urquhart, S. G., A. P. Hitchcock, A. P. Smith, H. Ade and E. G. Rightor (1997). "Inner-shell excitation spectroscopy of polymer and monomer isomers of dimethyl phthalate." Journal of Physical Chemistry B **101**(13): 2267-2276.

Urquhart, S. G., A. P. Hitchcock, A. P. Smith, H. W. Ade, W. Lidy, E. G. Rightor and G. E. Mitchell (1999). "NEXAFS spectromicroscopy of polymers: overview and quantitative analysis of polyurethane polymers." Journal of Electron Spectroscopy and Related Phenomena **100**: 119-135.

Väterlein, P., R. Fink, E. Umbach and W. Wurth (1998). "Analysis of the x-ray absorption spectra of linear saturated hydrocarbons using the Xα scattered-wave method." Journal of Chemical Physics **108**(8): 3313-3320.

Venables, J. A., G. D. T. Spiller and M. Hanbücken (1984). "Nucleation and growth of thin films." Reports on Progress in Physics **47**(4): 399-459.

Walton, A. G., S. H. Carr and E. Baer (1968). "Molecular orientation of macromolecules in ionic force fields." Polymer Preprints (American Chemical Society) **9**: 603-616.

Ward, M. D. (2001). "Bulk crystals to surfaces: combining X-ray Diffraction and Atomic force microscopy to probe the structure and formation of crystal interfaces." Chemical Reviews **101**: 1697-1725.

Watts, B. and H. Ade (2006). Measurement of linear polarization of 5.3.2 STXM, Department of Physics, NCSU.

Weiss, K., P. S. Bagus and C. Wöll (1999). "Rydberg transitions in X-ray absorption spectroscopy of alkanes: The importance of matrix effects." Journal of Chemical Physics **111**(15): 6834-6845.

Weiss, K., J. Weckesser and C. Wöll (1999). "An X-ray absorption study of saturated hydrocarbons physisorbed on metal surfaces." Journal of Molecular Structure (Theochem) **458**: 143-150.

Weiss, K., C. Woll, E. Bohm, B. Fiebranz, G. Forstmann, B. Peng, V. Scheumann and D. Johannsmann (1998). "Molecular orientation at rubbed polyimide surfaces determined with X-ray absorption spectroscopy: Relevance for liquid crystal alignment." Macromolecules **31**(6): 1930-1936.

Weiss, K., C. Wöll and D. Johannsmann (2000). "Orientation of thin liquid crystal films on buffed polyimide alignment layers: A near-edge x-ray absorption fine structure investigation." Journal of Chemical Physics **113**(24): 11297-11305.

Wellinghoff, S., F. Rybnikar and E. Baer (1974). "Epitaxial crystallization of polyethylene." Journal of Macromol Science - Physics **B10**(1): 1-39.

Willems, J. (1958). "Oriented growth in the field of organic high polymers." Discussions of the Faraday Society: 111-113.

Willems, J. and I. Willems (1956). "Oriented overgrowth of paraffin wax crystls on spherulites of polyethylene." Nature **178**(4530): 429-430.

Willey, T. M., A. L. Vance, T. van Buuren, C. Bostedt, A. J. Nelson, L. J. Terminello and C. S. Fasley (2004). "Chemically transformable configurations of mercaptohexadecanoic acid self-assembled monolayers adsorbed on Au (111)." Langmuir **20**: 2746-2752.

Wittmann, J. C., A. M. Hodge and B. Lotz (1983). "Epitaxial crystallization of polymers onto benzoic acid: Polyethylene and paraffins, aliphatic polyesters,

and polyamides." Journal of Polymer Science: Polymer Physics Edition **21**: 2495-2509.

Wittmann, J. C. and B. Lotz (1981). "Epitaxial crystallization of polyethylene on organic substrates: a reappraisal of the mode of action of selected nucleating agents." Journal of Polymer Science: Polymer Physics Edition **19**: 1837-1851.

Wittmann, J. C. and B. Lotz (1990). "Epitaxial crystallization of polymers on organic and polymeric substrates." Progress in Polymer Science **15**: 909-948.

Xiang, M. L., X. Li, C. K. Ober, K. Char, J. Genzer, E. Sivaniah, E. J. Kramer and D. Fischer (2000). "Surface stability in liquid-crystalline block copolymers with semifluorinated monodendron side groups." Macromolecules **33**: 6106-6119.

Young, A. T., E. Arenholz, S. Marks, R. Schlueter, C. Steier, H. A. Padmore, A. P. Hitchcock and D. G. Castner (2002). "Variable linear polarization from an X-ray undulator." Journal of Synchrotron Radiation **9**: 270-274.

Zhang, W. P. and D. L. Dorset (1989). "Epitaxial growth of long-chain molecules on potassium hydrogen phthalate and potassium chloride substrates from the vapor phase." Journal of Polymer Science: Part B: Polymer Physics **27**: 1433-1447.

Zhang, X., R. Balhorn and J. Mazrimas (1996). "Mapping and measuring DNA to protein ratios in mammalian sperm head by XANES imaging." Journal of Structural Biology **116**: 335-344.

Zhang, X., C. Jacobsen, S. Lindaas and S. Williams (1995). "Exposure strategies for polymethyl methacrylate from in situ x-ray absorption near edge structure spectroscopy." Journal of Vacuum Science and Technology B **13**(4): 1477-1483.

Zhang, X., A. E. Statonbevan, D. W. Pashley, S. D. Parker, R. Droopad, R. L. Williams and R. C. Newman (1990). "A Transmission electron-microscopy and reflection high-energy electron-diffraction study of the initial-stages of the heteroepitaxial growth of InSb on GaAs(001) by molecular-beam epitaxy." Journal of Applied Physics **67**(2): 800-806.

Zharnikov, M., W. Geyer, A. Gölzhäuser, S. Frey and M. Grunze (1999). "Modification of alkanethiolate monolayers on Au-substrate by low energy electron irradiation: alkyl chains and the S/Au interface." Physical Chemistry Chemical Physics **1**: 3163-3171.

Zharnikov, M. and M. Grunze (2001). "Spectroscopic characterization of thiol-derived self-assembling monolayers." Journal of Physics: Condensed Matter **13**: 11333-11365.

Ziegler, C., T. Schedel-Niedrig, G. Beamson, D. T. Clark, W. R. Salaneck, H. Sotobayashi and A. M. Bradshaw (1994). "X-ray absorption study of highly oriented poly(tetrafluoroethylene) thin films." Langmuir **10**(12): 4399-4402.

Zou, Y., T. Araki, G. Appel, A. D. L. Kilcoyne and H. Ade (2006). "Solid state effects in the NEXAFS spectra of alkane-based van der Waals crystals; Breakdown of molecular model." Chemical Physics Letters **accepted**.

Appendies

The appendies present those results that are pertinent to this project, but did not meet the intended objectives. These results include the unsuccessful experiments that failed to produce lateral orientation (§A1) or failed to produce large domains (§A2 and §A3). SVD mapping (§A4), atomic force microscopy (§A5), and polarized light microscopy (§A6) of HC thin films prepared on cleaved NaCl surface.

A1. Other substrates used for epitaxial growth of HC thin films

A1.1 HC films prepared by comelting with benzoic acid (BA)

Though laterally oriented HC molecules were obtained on solution-cast KHP crystals and on a cleaved NaCl (001) surface, the size of domains was too small for a series of NEXAFS spectra from the same sample area. The ideal substrate would be such that the HC molecules grown on it would only have one orientation or where the domain sizes are much larger. It is reported (Moss et al. 1984) that polyethylene (PE) grew on benzoic acid (001) face with only one direction (Wittmann et al. 1983; Wittmann et al. 1990) Therefore, benzoic acid was the third substrate we have tried for the growth of HC molecules.

The C 1s NEXAFS spectra of HC thin film prepared by comelting with BA substrate are shown in Figure A.1. BA has a high vapor pressure and cannot be

prepared in vacuum. Because the HC thin film was prepared by comelting and then transferred to Si_3N_4 membrane windows, it is necessary to verify that the thin film was HC and not BA. The NEXAFS spectrum is similar to the typical spectrum of HC as shown in §3.2.2, indicating that the sample on the Si_3N_4 membrane windows is HC. If BA were present on the membranes, a sharp peak at 285 eV, corresponding to the C 1s $\rightarrow \pi^*_{C=C}$ transition, would be observed.

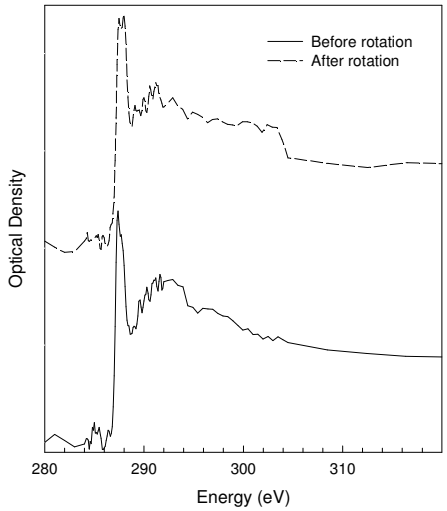

Figure A.1 C 1s NEXAFS spectra of HC thin films, prepared by comelting with BA, before (solid line) and after (dashed line) the sample was rotated by 90°

The C 1s $\rightarrow \sigma^*_{C\text{-}H}$ transitions exhibit maximum intensity regardless of the rotation, indicating that the HC molecules prepared by comelting with BA were normal to the substrate surface. This experiment had failed, as laterally oriented chains were desired. Since laterally oriented samples have been achieved on other substrates (§3.2.3.1 and §3.2.3.2), this BA substrate was not pursued further.

A1.2 HC films prepared on solution-cast p-bromo benzoic acid (p-BBA)

p-bromo benzoic acid (*p*-BBA) has been used as the substrate for epitaxial growth of long chain molecules, such as PE (Wittmann et al. 1990). The PE thin films only exhibit one molecular orientation when grown on the *p*-BBA substrate. We have used the solution-cast *p*-BBA thin film as the substrate to prepare laterally oriented HC thin films. We wish to get larger, laterally oriented domains. Figure A.2 presents the C 1s NEXAFS spectra of HC films prepared on solution-cast *p*-BBA before (solid line) sample rotation, sample rotation 45° (dashed line), and sample rotation 90° (dotted line). These three spectra exhibit similar contour and peak positions. The dominance of C 1s $\rightarrow \sigma^*_{C\text{-}H}$ transitions did not change with respect to the rotation, indicating that the HC molecules prepared on solution-cast *p*-BBA substrate were normally oriented to the substrate surface (cf. Figure 3.2(a)), which is similar to the HC film prepared on BA. This substrate failed to induce lateral orientation of HC thin films.

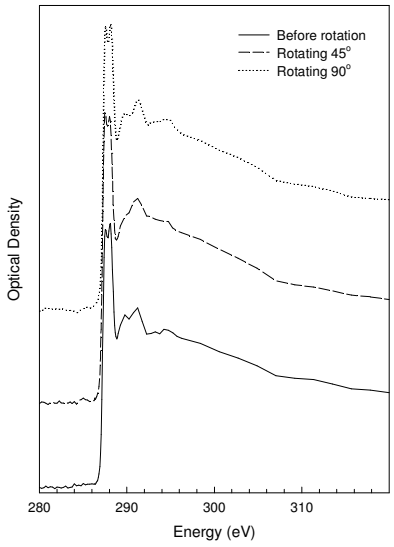

Figure A.2 C 1s NEXAFS spectra of HC films prepared on solution-cast *p*-BBA, at different rotation angles

A1.3 HC films prepared on evaporated *p*-phenyl benzoic acid (*p*-PBA)

The selection of *p*-phenyl benzoic acid (*p*-PBA) is based on its structure being similar to benzoic acid and it has been reported (Wittmann et al. 1990) that PE epitaxially grows from solution on the surface of *p*-PBA with only one molecular orientation. We have tried to grow HC thin film on evaporated *p*-PBA substrate in vacuum. Figure A.3 shows two X-ray absorption images at 287.6 eV and 330 eV of HC sample prepared on evaporated p-PBA substrates. Image contrast is appreciable in both images. The presence of image contrast in the 330 eV image indicates that the sample is not uniform. No more measurements were carried out on this sample.

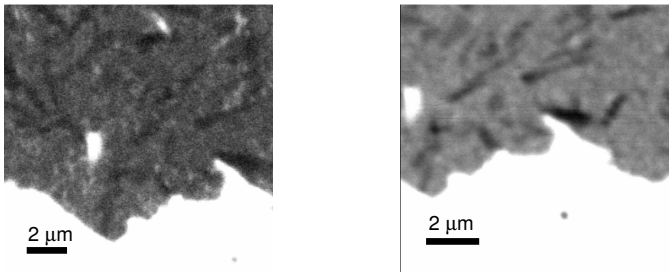

Figure A.3 X-ray absorption images of HC films prepared onto evaporated *p*-PBA substrates. (left: image was taken at 287.6 eV, right: image was taken at 330 eV)

A1.4 HC films prepared on evaporated KCl thin film

In analogy to HC films on cleaved NaCl (001) face, HC films were also formed on evaporated KCl thin films. We expected that the HC films formed on evaporated KCl thin films would have the lateral orientation just like on cleaved NaCl (001) surface. Figure A.4 shows NEXAFS spectra of HC crystals grown on evaporated KCl before (solid line) and after (dashed line) the sample holder was rotated by 90°. The dominance of C 1s $\rightarrow \sigma^*_{C\text{-}H}$ transitions in these two spectra indicates that the HC molecules are normally oriented on the evaporated KCl thin films.

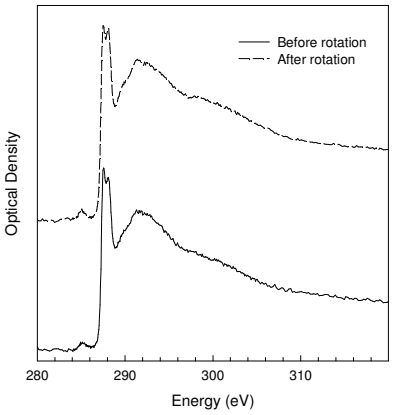

Figure A.4 NEXAFS spectra of HC thin film, prepared on evaporated KCl film

A1.5 HC films prepared on bare Si_3N_4 membrane

The HC thin films were also prepared on bare Si_3N_4 membrane windows. Figure A.5 (a) shows a typical X-ray absorption image of an HC sample on a bare Si_3N_4 membrane at 287.6 eV. There is no sample in the white region, which is the open area. A NEXAFS spectrum of this sample is shown in Figure A.5 (b) in which the C 1s $\rightarrow$ $\sigma^*_{C\text{-}H}$ transitions dominate and this domination is independent of rotation angle, indicating that the HC molecules in this sample were normally oriented on the substrate surface.

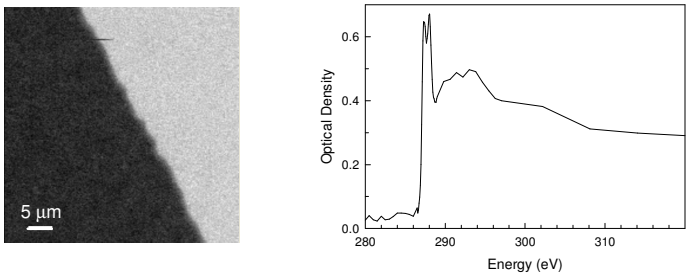

Figure A.5 X-ray absorption image of HC on Si_3N_4 membrane windows and X-ray absorption spectrum

A2. HC thin film prepared on EDTA chelating KHP substrate

In order to increase the domain size of the HC thin film prepared on KHP substrate, the KHP substrate was chelated with EDTA. It was expected that larger KHP crystals would form and could be cleaved just like the NaCl single crystal. Figure A.6 shows an X-ray absorption image of an HC thin film prepared on EDTA-chelating KHP substrate. This image was taken at 287.6 eV. Dark and light domains were visible. These domain sizes were in the range up to 1 μm. The domain size on this substrate did not improve.

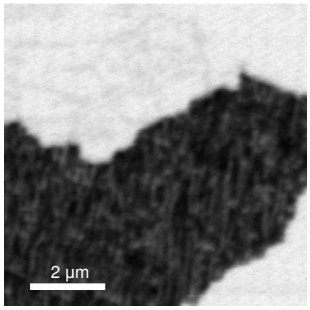

Figure A.6 X-ray absorption image of HC on EDTA-chelated KHP substrate.

A3. HC thin film prepared on TA substrate with elevated T_s

In order to increase the domain size, HC thin films were prepared on a TA substrate at elevated substrate temperatures. Figure A.7 showed the X-ray absorption images of HC thin films prepared on TA substrate at T_s = 36°C (left) and T_s = 54°C. These images were acquired at 287.6 eV. In both images, dark and light domains were visible. The domain size was estimated to be around several tens of nanometers.

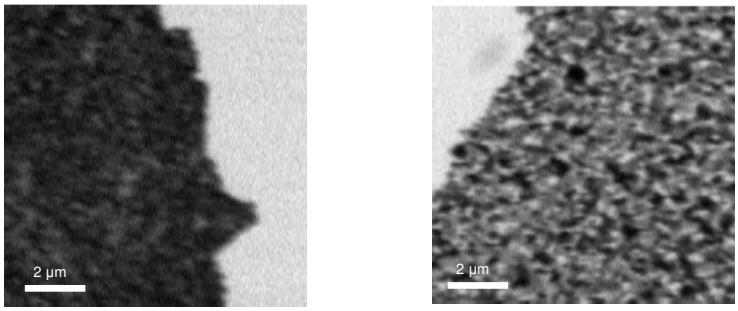

Figure A.7 X-ray absorption images of HC prepared on TA substrates at elevated substrate temperature. (left) T_s = 36°C, (right) T_s = 54°C

A4. Mapping of HC prepared on NaCl substrate

The Beer-Lambert optical absorption law described in Eq. (1.5) and Eq. (1.6) is the basis of the quantitative mapping in the X-ray absorption microscopy since the optical density of a multicomponent sample (chemical components and orientational components) is a superposition of the optical density of each component, weighted by its mass absorption coefficient at the photon energy used. The OD of a sample containing *j* noninteracting components is given by (Koprinarov et al. 2002)

$$OD(E) = \sum_{n=1}^{j} \mu(E)_n \rho_n t_n \tag{A.1}$$

where t_n is the thickness of each component with mass absorption coefficient μ_n at energy E and density ρ_n. For a sample with only one chemical species and uniform thickness, the linear relationship between optical density (OD) and mass absorption coefficient μ(E) will allow a quantitative analysis of orientational components present in the sample.

To carry out quantitative analysis, the NEXAFS spectra are recorded for each pure component. X-rays images of a multi-orientation-component sample of unknown spatial distributions are then recorded at a number of energies and chemical maps are derived by appropriate comparison to linear combinations of the mass absorption coefficients of the components.

Different mathematical methods can be used to obtain components maps from sets of X-ray spectromicroscopy images. Singular value decomposition (SVD) has been successfully used to quantitatively map the polypropylene and poly (acrylic acid) system (Koprinarov et al. 2002). Zhang et al (Zhang et al. 1996) applied SVD to examine the content and distribution of DNA and protein in mature mammalian sperm cells from images recorded at a few photon energies. Buckley and coworkers (Buckley et al. 1997) applied SVD to map the organic (protein) and inorganic (calcium ions) components of tissue.

The result of applying SVD to a sequence of X-ray images is a set of component maps, each of which is a plot of the density-thickness product. After correction for density, these maps provide component distribution in the selected sample area (Koprinarov et al. 2002).

The methodology of SVD is encoded in *Analysis of X-ray Images and Spectra (aXis)* program (Hitchcock 2000). In order to investigate the crystal domain size and distribution of the orthogonally oriented HC crystal domain prepared on cleaved NaCl (001) face, SVD has been used to map the HC sample prepared on NaCl with T_s = RT and T_s = 45°C. The spectroscopic basis to distinguish the orientational components is presented in Figure A.8, which plots the C1s NEXAFS spectra of HC sample with two

orientations in optical density unit: macromolecular backbone parallel to the electric field vector *E* (solid line) and macromolecular backbone perpendicular to ***E*** (dashed line). The spectrum of HC sample with macromolecular chain parallel to ***E*** is dominated by a broad resonance at 293.4 eV, which is attributed to the C 1s $\rightarrow \sigma^*_{C\text{-}C}$ transition. When the HC macromolecular backbone is perpendicular to E, the NEXAFS spectrum is dominated by two sharp resonances at 288 eV, which is assigned to the C 1s$\rightarrow\sigma^*_{C\text{-}H}$ transition.

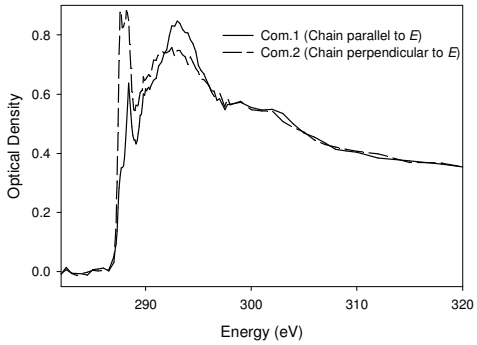

Figure A.8 NEXAFS spectra of HC sample with two orientations with respect to electric field vector ***E***. Component 1 (solid line) with macromolecular chain parallel to ***E*** and component 2 with macromolecular chain perpendicular to ***E***.

Figure A.9 compares these two orientational component maps of HC sample prepared on cleaved NaCl (001) face with T_s = RT

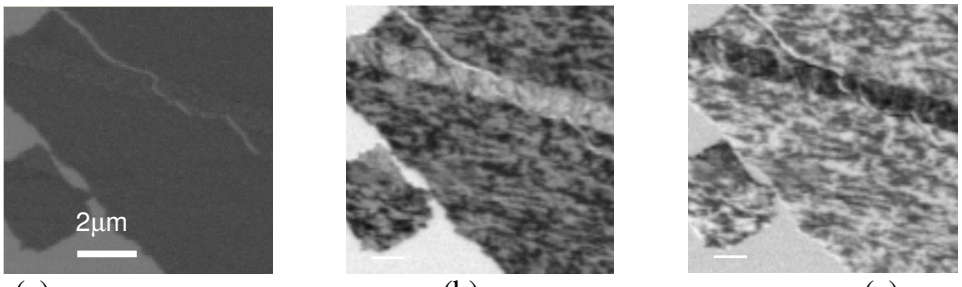

(a) (b) (c)

Figure A.9 (a) Transmission STXM image at 300 eV of HC sample prepared at T_s = RT (b) Component 1 (HC macromolecular backbone parallel to ***E***) and (c) Component 2 (HC macromolecular backbone perpendicular to ***E***) maps derived by applying SVD to image (a)

Figure A.9 (a) is a transmission image at 300 eV, at which the two orientational components absorb photons nonpreferentially so that in the dark gray sample area no contrast is observed. The light gray area is open area, no sample present. The two components derived from SVD are presented in Figure A.9 (b) and (c), respectively. Image contrast is observed in both maps. The dark domains absorb more photons, indicating that the HC molecules in such domains are parallel to ***E***. In the light domains HC molecules are perpendicular to ***E***. In both maps, the dark and light domains are close to each other and of the submicron size.

Figure A.10 compares these two orientational component maps of HC sample prepared on cleaved NaCl (001) face with $T_s = 45°C$.

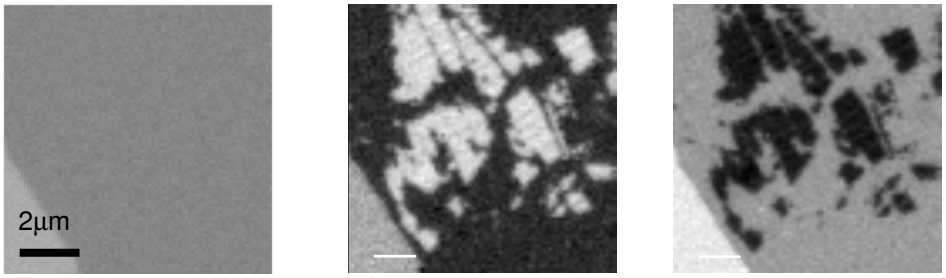

Figure A.10 (a) Transmission STXM image at 300 eV of HC sample prepared at $T_s = 45°C$ (b) Component 1 (HC macromolecular backbone parallel to ***E***) and (c) Component 2 (HC macromolecular backbone perpendicular to ***E***) maps derived by applying SVD to image (a)

From the orientation maps presented in Figure A.10 (b) and (c), it is clear to see that the single orientation domains start to coalesce and become larger compared with those presented in Figure A.9 (b) and (c).

A5 Atomic Force Microscope images of HC on NaCl

A5.1 AFM images of cleaved NaCl

The substrate surface topography has a direct influence on the orientation of a deposit. Substrates with a large smooth surface are suitable for nucleation of epitaxy. Atomic force microscopy (AFM) can be used to characterize the surface topography of substrates. AFM (Ward 2001) is a method to characterize the surface structure of non-conductive materials. A two-dimensional image is acquired by scan-rasting the tip over a specified area of the sample. Figure A.11 presents non-contact mode AFM image of a cleaved NaCl surface. It is possible to obtain large scale flat surface.

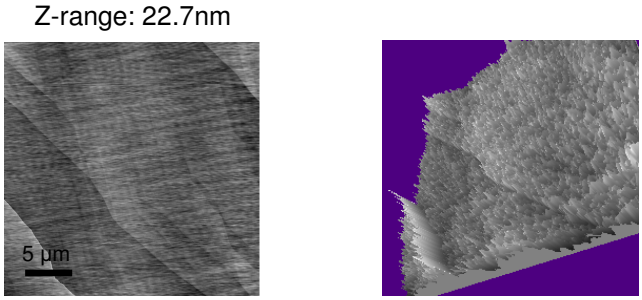

Figure A.11 Non-contact mode AFM image of cleaved NaCl (001) surface.

A5.2 AFM images of HC films prepared on cleaved NaCl with different T_s

Morphology of hexacontane epitaxially grown on graphite surface by spin-casting of diluted HC solutions has been studied by tapping mode AFM (Magonov et al. 2003). Epitaxial alkane layers formed directly on the substrate surface were characterized by lamellar morphology. Imaging of the alkane films at elevated temperatures revealed that nanocrystals melted around 95°C, while the epitaxial layers were observed at temperature up to 140 °C. We have used the AFM microscope to characterize the HC

sample prepared onto cleaved NaCl (001) at different substrate temperature. The non-contact mode AFM images are presented in Figure A.12. The size of these two images is 4 μm × 4 μm. The left showed the AFM image of HC thin films prepared on NaCl at T_s = 45°C. The contrast in this image is more uniform. The rod structure exhibits a long range order. The rod structures are all in the same direction. The right showed the AFM image of HC thin films prepared on NaCl at T_s = RT. This image exhibits a somewhat rough surface. The rod structure only showed short range order. Orthogonal rod structures are visible. These AFM images of HC thin films prepared at different substrate temperature support the NEXAFS spectroscopy and microscopy results that the domain size increases with the increasing substrate temperature.

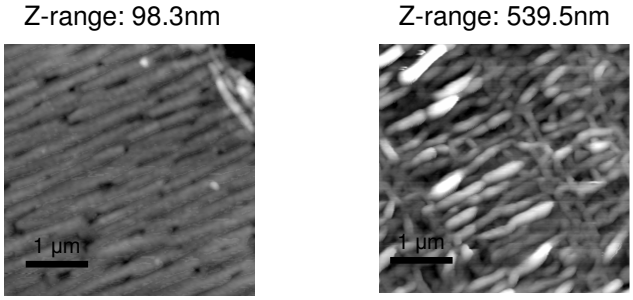

Figure A.12 Non-contact AFM images of HC sample prepared on cleaved NaCl (001) at different substrate temperature. (left) T_s = 45°C, (right) T_s = RT.

A6 Polarized light microscopy of HC samples

The polarized light microscopy (PLM) is an optical technique of measuring orientation in an optically anisotropic sample, in which the refractive index (*n*) varies with the molecular orientation. Crystalline material is usually anisotropic due to the large degree of ordering in their structure. For example, the refractive index along the

orthorhombic unit cell axis is n_a = 1.514, n_b = 1.519, and n_c = 1.575 for the orthorhombic n-$C_{36}H_{74}$ crystal (Bunn et al. 1954).

In PLM, two polarizing lenses are inserted into the optical path, one in the incoming light – polarizer, and one between the sample and eyepiece – analyzer. When the analyzer is perpendicular to the polarizer, this is called 'crossed polarized'. That is, the polarizer only transmits light that is polarized in one direction and the analyzer only transmits light that is polarized in the perpendicular direction. If the sample is isotropic, when using crossed polarizer, no light will pass through the sample and a dark field of view will be seen in the eyepieces. However, for an anisotropic sample, the retardation of light by the different refractive index is different, thus the new light emerging from the sample is deviated from the incident light, allowing the light to pass through the analyzer. The contrast observed in the PLM images for a crystalline material is due to the different optical path of the sample with the media, causing by their different refractive index.

Figure A.13 presents the polarized light microscopic images of HC sample prepared onto cleaved NaCl (001) surface at T_s = 45°C. These measurements were performed using a Nikon Metallurgical ECLIPSE ME600P Microscope, in which the polarization of the light passing through the polarizer can be left-right and up-down in the horizontal plane, while the polarization of the light passing through the analyzer only has one direction: up-down. When the light is polarized left-right in the sample plane (cross polarized), many small patches are visible (Figure A.13, left), whereas in the right image, where the light is polarized up-down in the sample plane (parallel

polarized), such patches disappear. The on-off of the small patches with the orientation of the light indicated that the sample was dominated by one orientation.

This image is the same sample area as shown in Figure 3.12. The shapes, the domains, the defects in both images are the same, demonstrating that polarized light microscopy can be used to estimate the orientation domains.

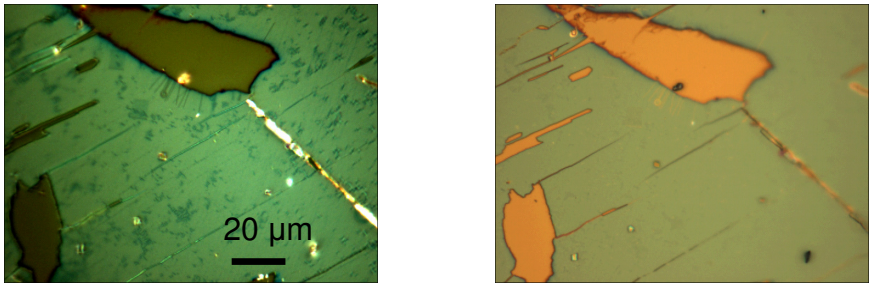

Figure A.13 Epi-polarized light microscopic images of the HC thin film prepared on cleaved NaCl at T_s = 45°C